Faculdade de Engenharia da Universidade do Porto

Instituto de Ciências Biomédicas Abel Salazar

Uncovering the Liquid-Liquid Phase Separation Behavior of Ataxin-3

Sára Joana Varga

DISSERTATION

Master in Bioengineering
Major in Molecular Bioengineering

Supervisor: Zsuzsa Sárkány, PhD
Co-supervisor: Rita Vilaça, PhD

June 2022

This study was supported by FEDER funds through the COMPETE 2020 - Operacional Programme for Competitiveness and Internationalisation (POCI), Portugal 2020; Portuguese funds through FCT in the framework of the projects POCI-01-0145-FEDER-031173 and POCI-01-0145-FEDER-031323, and by European Union's Horizon 2020 Research and Innovation programme under grant agreement ID 952334 "PhasAGE".

© Sára Varga, 2022

Resumo

Os organelos sem membrana resultam de um fenómeno termodinâmico designado por separação de fases líquido-líquido, em que uma solução homogénea se separa em duas fases líquidas distintas e com composições diferentes. Recentemente, tem sido proposto que alterações no processo normal de separação de fases líquido-líquido poderão contribuir para a formação de agregados proteicos estando, desta forma, envolvidos na patogénese de diversas doenças neurodegenerativas.

A doença de Machado-Joseph é uma doença neurodegenerativa rara, hereditária e progressiva associada a uma mutação por expansão de repetições do tripleto CAG no gene *ATXN3*. Esta mutação resulta na transcrição e tradução da respetiva proteína ataxina-3 com uma expansão anormal da cauda de poliglutaminas. Apesar deste segmento de poliglutaminas mais longo ser essencial para a formação de estruturas mais complexas do tipo amiloide, a ataxina-3 também contém outras regiões na sua estrutura que promovem a sua agregação. De facto, a própria ataxina-3 não expandida é capaz de formar agregados proteicos, embora de menor complexidade, como as protofibrilas, *in vivo* e *in vitro*.

Este trabalho teve como objetivo caracterizar as condições experimentais para o estudo do processo de separação de fases líquido-líquido da ataxina-3 não expandida *in vitro*. Os resultados obtidos sugerem que esta proteína está envolvida na formação de condensados moleculares por separação de fases líquido-líquido na presença de um *crowding* biomolecular. Adicionalmente, foi demonstrado que o comportamento de separação de fases da ataxina-3 é influenciado pelas condições ambientais, nomeadamente a força iónica e o tipo de solução tampão. A caracterização das propriedades físicas dos condensados biomoleculares de ataxina-3 demonstrou ainda que estes são de natureza gelatinosa. Estes resultados sugerem que o processo de agregação da proteína poderá ter início no interior destas gotículas. Os resultados obtidos neste trabalho contribuem para uma melhor caracterização dos mecanismos moleculares envolvidos no processo de agregação da ataxina-3, o que levará a uma melhor compreensão da patogénese da doença de Machado-Joseph.

Abstract

Membraneless organelles are transient structures formed by a thermodynamic phenomenon of liquid-liquid phase separation by which a homogeneous liquid solution de-mixes into two liquid phases with distinct compositions. Recently, abnormal liquid-liquid phase separation has been implicated in the formation of protein aggregates and, consequently, in the pathogenesis of multiple neurogenerative diseases.

Machado-Joseph Disease is a hereditary and progressive rare neurodegenerative disease characterized by an abnormal expansion of repeated CAG triplets stretch in the *ATXN3* gene. This mutation results in an expanded polyglutamine tail on the ataxin-3 protein. Although this longer polyglutamine tract is essential for the formation of high-complexity amyloid-like structures, ataxin-3 also presents other structural features that favour its aggregation. Accordingly, non-expanded ataxin-3 can form less complex protein aggregates, designated as protofibrils, *in vitro* and *in vivo*.

This work aimed to characterize the experimental conditions to study the process of liquid-liquid phase separation of non-expanded ataxin-3 *in vitro*. The results suggest that non-expanded ataxin-3 can undergo liquid-liquid phase separation in a crowded environment. Moreover, ataxin-3 phase separation behavior is strongly dependent on the environmental conditions, such as ionic strength and buffer type. The characterization of the material properties of ataxin-3 droplets also revealed that they are of a gel-like nature, suggesting that the first steps of ataxin-3 protein aggregation might occur inside them. The overall results enlighten the molecular mechanisms that underlie the first steps of ataxin-3 aggregation, which will ultimately translate into a better understanding of the pathogenesis of Machado-Joseph disease.

Acknowledgements

I would like to take this opportunity to firstly thank Dr. Sandra Ribeiro for welcoming me into her research group with such open arms and for sharing her vast knowledge with me. She pushed me to go a bit further every time, and that is something that I will always remember.

Secondly, my full appreciation goes to my supervisor and to my co-supervisor, Dr. Zsuzsa Sárkány and Dr. Rita Vilaça. This work would not have been possible without the both of you. You were always there to motivate me, ground me, and help me whenever I needed it the most. I am truly so grateful for all that I learned from you.

A special thank you goes to Francisco for dedicating his time to remind me that protein purification is a beautiful thing.

To the other members of the Biomolecular Structure and Function group, thank you for creating such a friendly and welcoming work environment.

Finally, I would like to thank my parents and my family for supporting me throughout every stage of my life.

Contents

Resumo iii

Abstract v

Acknowledgements vii

Contents ix

List of Figures x

List of Tables xii

Abbreviations xiv

Chapter 1 1

Introduction 1
1.1 Context and Motivation 1
1.2 Objectives 2
1.3 Dissertation Outline 3

Chapter 2 5

Literature Review 5
2.1 Liquid-Liquid Phase Separation in Biology 5
2.2 Aberrant Liquid-Liquid Phase Separation in Neurodegeneration 12
2.3 Machado-Joseph Disease and Ataxin-3 17
2.4 Liquid-Liquid Phase Separation of Ataxin-3 21
2.5 Experimental Approaches to Study Liquid-Liquid Phase Separation *In Vitro* 23

Chapter 3 28

Materials and Methods 28
3.1 Materials 28
3.2 Methods 33

Chapter 4 49

Results and Discussion 49
4.1 Expression and Purification of the Ataxin-3 Constructs 49
4.2 Characterization of Ataxin-3 Liquid-Liquid Phase Separation Behavior in Different Conditions 54
4.3 Identification of the Ataxin-3 Region Responsible for Liquid-Liquid Phase Separation 68
4.4 Determination of the Material Properties of Ataxin-3 13Q Droplets 70

Chapter 5 73

Conclusions and Future Perspectives 73

References 75

List of Figures

Figure 1 Intracellular distribution of the biomolecular condensates identified in eukaryotic cells thus far 6

Figure 2 Proposed mechanisms for enzymatic rate regulation by biomolecular condensates... 9

Figure 3 Summary of the effects of disease-associated alterations on biomolecular condensates, leading to aberrant LLPS in cells 12

Figure 4 The proposed role for biomolecular condensates in the protein aggregation pathway, culminating in neurodegeneration 14

Figure 5 Schematic representation of the aggregation pathway of the non-expanded and expanded forms of ataxin-3 21

Figure 6 Schematic representation of fundamental properties of liquid-like droplets..... 23

Figure 7 Schematic representation of the protocol used for sedimentations assays. 24

Figure 8 Schematic representation of a FRAP experiment with condensates of different material properties. 27

Figure 9 Schematic representation of the sample preparation protocol for the turbidimetry assays. 37

Figure 10 Schematic representation of the protocol used for the sample preparation for the microscopy imaging. 42

Figure 11 Ataxin-3 D1 expression and purification. 51

Figure 12 Ataxin-3 13Q expression and purification. 52

Figure 13 GFP-ataxin-3 13Q expression and purification. 53

Figure 14 GFP-ataxin-3 13Q purification by a two-step elution in the IMAC chromatography column. 54

Figure 15 Bioinformatic analysis of the primary structure of ataxin-3 13Q to predict its propensity to undergo phase separation. 56

Figure 16 Effect of PEG concentration on LLPS of ataxin-3 13Q. 58

Figure 17 Effect of GFP-ataxin-3 13Q concentration on the LLPS of ataxin-3 13Q. 60

Figure 18 Effect of protein concentration on the LLPS of ataxin-3 13Q. 62

Figure 19 Effect of NaCl concentration on the LLPS of ataxin-3 13Q. 64

Figure 20 Effect of NaCl concentration on the saturation concentration for the LLPS of ataxin-3 13Q. 65

Figure 21 Effect of NaCl concentration on the crowding agent-dependent LLPS of ataxin-3 13Q. 66

Figure 22 Effect of buffer type on the LLPS behavior of ataxin-3. 67

Figure 23 Characterization of the LLPS behavior of ataxin-3 D1. 69

Figure 24 Characterization of the material properties of ataxin-3 13Q droplets at different salt concentrations. 71

List of Tables

Table 1 List of biomolecular condensates described to this date with their intracellular localization and function..... 6

Table 2 Characterization of each subtype of Machado-Joseph disease 19

Table 3 List of the bacterial strains used for the experiments described in the following sections..... 28

Table 4 List of the cell culture media used for the experiments described in the following sections..... 29

Table 5 List of the buffer solutions used for the experiments described in the following sections..... 30

Table 6 Relevant physicochemical parameters for the purification of ataxin-3 constructs computed by ProtParam. 32

Table 7 List of the plasmids used for the experiments described in the following sections. .. 32

Table 8 Composition of the resolving and stacking gels for the SDS-PAGE analysis. 36

Table 9 Sample preparation for the turbidimetry assay (PEG concentration test). 38

Table 10 Sample preparation for the turbidimetry assay (GFP-ataxin-3 13Q concentration test)..... 38

Table 11 Sample preparation for the turbidimetry assay (ataxin-3 concentration test)..... 39

Table 12 Sample preparation for the turbidimetry assay (NaCl concentration test). 39

Table 13 Sample preparation for the turbidimetry assay (buffer type test). 40

Table 14 Sample preparation for the turbidimetry assay (ataxin-3 D1 construct test). 41

Table 15 Sample preparation for the microscopy imaging (ataxin-3 13Q and NaCl concentration test). 43

Table 16 Sample preparation for the microscopy imaging (PEG and NaCl concentration test). 45

Table 17 Channel settings used in the microscopy analysis with the IN Cell Analyzer imaging system. 47

Table 18 Sample preparation for the FRAP assay (NaCl concentration test). 48

Table 19 Elution volumes of each ataxin-3 construct in size exclusion chromatography when using the HiPrep™ 26/60 Sephacryl® S300 HR column..... 50

Table 20 Final yields obtained in the purification of each ataxin-3 construct. 50

Table 21 Variation in the mobile fraction and diffusion coefficient in response to changes in the ionic strength. 70

Abbreviations

α-syn	α-Synuclein
AD	Alzheimer's Disease
AFM	Atomic Force Microscopy
ALS	Amyotrophic Lateral Sclerosis
APS	Ammonium Persulfate
ARF	Auxin Response Transcription Factor
ATP	Adenosine Triphosphate
DDX4	DEAD-Box Helicase 4
DIC	Differential Interference Contrast
DLS	Dynamic Light Scattering
DMSO	Dimethyl Sulfoxide
DNA	Deoxyribonucleic Acid
DNAse	Deoxyribonuclease
DTT	Dithiothreitol
EDTA	Ethylenediamine Tetraacetic Acid
FITC	Fluorescein Isothiocyanate
FRAP	Fluorescence Recovery After Photobleaching
FTD	Frontotemporal Dementia
FUS	Fused in Sarcoma
G3BP1	Ras-GTPase-Activating Protein-Binding Protein 1
GFP	Green Fluorescent Protein
GKAP	Guanylate Kinase-Associated Protein
HD	Huntington's Disease
IDP	Intrinsically Disordered Protein
IDR	Intrinsically Disordered Region
IMAC	Immobilized Metal Affinity Chromatography
JD	Josephin Domain
LAT	Linker for Activation of T-Cell
LB	Luria-Bertani
LLPS	Liquid-Liquid Phase Separation
MJD	Machado-Joseph Disease
mRNA	Messenger Ribonucleic Acid
MWCO	Molecular Weight Cut-Off
NA	Numerical Aperture
NMDA	N-Methyl-D-Aspartate

OPT	Oct1/PTF/Transcription
PcG	Polycomb Group
PD	Parkinson's Disease
PEG	Polyethylene Glycol
PML	Promyelocytic Leukemia
PMSF	Phenylmethylsulphonyl fluoride
polyQ	Polyglutamine
PQC	Protein Quality Control
PRM	Proline-Rich Motif
PSD	Post-Synaptic Density
PSD-95	Post-Synaptic Density-95
PVDF	Polyvinylidene Fluoride
rDNA	Ribosomal Deoxyribonucleic Acid
rpm	Rotations Per Minute
RNA	Ribonucleic Acid
RNAse	Ribonuclease
rRNA	Ribosomal Ribonucleic Acid
RuBP	Ribulose Biphosphate
SCA3	Spinocerebellar Ataxia type 3
SDS	Sodium Dodecyl Sulfate
SDS-PAGE	Sodium Dodecyl Sulfate-Polyacrylamide Gel Electrophoresis
SEC	Size Exclusion Chromatography
SG	Stress Granule
SH3	SRC Homology 3
SI	Salt-Induced
SOB	Super Optimal Broth
TCR	T-Cell Receptor
TDP-43	TAR DNA-Binding Protein 43
TEMED	N,N,N',N'-Tetramethylethylenediamine
ThT	Thioflavin T

Chapter 1

Introduction

1.1 Context and Motivation

Liquid-liquid phase separation (LLPS) is defined as a reversible phenomenon by which a liquid solution de-mixes into two phases with distinct solute concentrations[1-4]. In the late nineteenth century, Wilson reported the observation of LLPS *in vivo* when studying the protoplasm of echinoderm-eggs[5]. He described this cellular compartment as:

"… a liquid, or rather a mixture of liquids, in a form of a fine emulsion consisting of a continuous substance in which are suspended drops …"[5]

Ever since then, numerous liquid biomolecular condensates have been identified in eukaryotic cells[6,7]. They have been designated as membraneless organelles, as, by concentrating certain biomolecules in specific regions of the cell, they can organize the intracellular compartment and restrict biological functions to defined areas without the need for a lipidic membrane. Membraneless organelles were observed in different intracellular locations such as the nucleoplasm (e.g., nucleolus), and the cytoplasm (e.g., stress granules), while a set of them is found in association with different cellular membranes (e.g., post-synaptic density)[7]. Their functions range from the protection of the cells against external stressors, to the enhancement of enzymatic reactions (for a more extensive description of the already characterized biomolecular condensate functions see Section 2.1)[6,7].

More recently, in addition to its importance for normal cell function, aberrant LLPS has been shown to lead to protein aggregation, which is a hallmark of multiple well-known neurodegenerative diseases[3,4,8]. In fact, although the healthy forms of the causative proteins of certain neurodegenerative disorders have been shown to undergo LLPS *in vitro* and *in vivo*, disease-causing mutations often lead to irreversible hardening of the droplets[9-12]. The biological consequences of this aberrant liquid-to-solid phase transition are being extensively explored,

in an effort to undercover their potential role in disease pathogenesis. Notably, all of the disease-associated proteins listed above contain intrinsically disordered regions. These highly flexible segments are a common feature to a great number of proteins with LLPS behavior, as they participate in weak and transient intermolecular interactions required for the formation of liquids[1,3,4,6,13-15].

Machado-Joseph Disease (MJD) is a hereditary and progressive rare neurodegenerative disease that currently affects 1-5 per 100000 people worldwide[16]. Even so, it is the most common type of spinocerebellar ataxia[17,18] and the second most prevalent polyglutamine (polyQ) disorder, surpassed only by Huntington's disease[19]. As all other polyQ diseases, MJD is characterized by an abnormally expanded stretch of repeated CAG triplets that ultimately leads to a longer sequence of glutamine residues in the protein codified by the affected gene. In this particular disease, the mutated gene is called *ATXN3*. It encodes the ataxin-3 protein, a ubiquitously expressed deubiquitinating enzyme that participates in the proteasomal protein degradation pathway and has been shown to regulate gene transcription.[20] A maximum of 44 glutamine residues have been found in the ataxin-3 protein of healthy individuals. However, this number rises to a range of 52-86 repeats in MJD patients[1,19,21]. In its architecture, ataxin-3 contains a large N-terminal folded domain, the Josephin domain (JD), responsible for the protein's isopeptidase activity. There are also three ubiquitin interacting motifs (UIMs) that allow for the enzyme to bind to its targets. The polyQ stretch localizes to the C terminal region of the protein.

Ataxin-3 is a mix-folded protein: in addition to its globular N-terminal domain, this protein has intrinsically unfolded regions throughout its C-terminal portion[21]. This feature of ataxin-3 makes it a promising candidate to undergo LLPS. This is endorsed by *in silico* bioinformatic analysis, that shows that the protein's sequence has portions with a high aggregation and high residue-based droplet-promoting probabilities. In fact, this was the reasoning that motivated the development of the work described in this dissertation. We aimed to study the environmental conditions that promote ataxin-3 liquid-liquid phase separation *in vitro* and determine if these are compatible with what is observed within the intracellular compartment. Ultimately, the description and detailed characterization of the liquid-liquid phase separation behavior of ataxin-3 can, on the one hand, enhance our understanding of the pathological mechanisms that underlie the development of the MJD, and, on the other hand, potentially uncover new therapeutic targets for this currently incurable disease.

1.2 Objectives

Multiple causative proteins of neurodegenerative disorders have been shown to undergo phase separation *in vitro* and *in vivo*, even in physiological conditions. However, only recently has ataxin-3 been described to exhibit LLPS behaviour in a crowded environment[1]. As the study

of ataxin-3 LLPS is in its preliminary stages, additional fundamental level experiments are essential to further elucidate why and how this phenomenon may occur in biological systems.

The first steps to explore the phase separation behavior of a specific protein often comprise an extensive molecular characterization *in vitro* under different biologically relevant conditions. For this reason, the first goal of this work was to determine how a crowded environment (i.e., PEG concentration), protein concentration, ionic strength, and buffer type influence the formation of a condensed phase of ataxin-3 in solution. Ultimately, these experiments help to clarify how the intracellular environment would favour the occurrence of ataxin-3 LLPS *in vivo*. In addition, varying salt concentrations and buffer type provide us with knowledge about the type of intermolecular interactions (e.g., electrostatic, or hydrophobic) that participate in the assembly of the protein-concentrated droplets.

Furthermore, it is well-established that different regions of ataxin-3 participate in its aggregation cascade, which ultimately leads to the formation of multimolecular protein assemblies (see in more detail in Section 2.3)[1,19-21]. Consequently, the second objective of this work was to identify what portion of the protein might be responsible for the molecular interactions that lead to droplet formation.

Finally, in this work, we aimed to determine the material properties of the ataxin-3 droplets. While some spherical droplets that result from LLPS remain in the liquid state for longer periods of time, others suffer a faster process of aging that hardens them to a gel-like material (also known as gelation)[4,15]. In the first case, the molecules in the condensed phase can move freely inside the droplets and exchange with the surrounding dilute phase. On the other hand, in gel-like droplets, their components remain static.

Overall, this dissertation shows a detailed characterization of the LLPS behavior of ataxin-3 through the implementation of a variety of experimental techniques. This will ultimately contribute to a better understanding of the molecular mechanisms that underlie the aggregation pathway of this protein.

1.3 Dissertation Outline

The present dissertation is organized in five chapters. In Chapter 1, a short description of the motivation for this experimental work as well as its primary objectives are presented. Next, Chapter 2 is an elucidation of the main theoretical concepts that are fundamental for the comprehension of the following sections of the document, including: i) a description of how LLPS has been implicated in the normal, and also aberrant, function of biological systems; ii) a presentation of the protein system that was studied (e.g., ataxin-3) and how this molecule is

proposed to be the causative protein of MJD, a neurodegenerative disorder; iii) the state of the art of the LLPS behavior of ataxin-3; and, finally, iv) a list of experimental methodologies that can be implemented to study and characterize liquid-liquid phase separation of biomolecules *in vitro*. The following Chapter 3 is an in-depth description of the methodologies that were implemented during this experimental work. In Chapter 4, the obtained results are presented, followed by a discussion, where the results are critically analyzed and interpreted. Lastly, in Chapter 5, the conclusions drawn from the work previously described are listed. This final section also includes plans for future experiments that would complete or complement the results obtained so far.

Chapter 2

Literature Review

2.1 Liquid-Liquid Phase Separation in Biology

Liquid-liquid phase separation (LLPS) is the name given to the process by which a liquid mixture gives place to two different liquid phases: i) a condensed phase, in which solute concentration is superior; and ii) a dilute phase, in which solute concentration is lower. This phenomenon is only thermodynamically favourable when it minimizes system's free energy[6,7,22,23]. As other phase transitions, liquid-liquid phase separation is highly dependent on the environmental conditions, such as temperature, pH, ionic strength, solute concentration, and biomolecular crowding[6].

2.1.1 Biomolecular Condensates

LLPS has been proposed to occur in biological systems, as a mechanism that allows for the spatiotemporal organization of the biochemical reactions in the intracellular compartment[6,15]. By simply observing the interior of any cell, one can identify a great number of membrane-bound organelles, including the nucleus, the mitochondria, and the lysosome, for instance. The presence of a lipidic layer that separates the interior of these structures from the rest of the cytoplasm allows for a specific function of the cell (e.g., DNA transcription and replication, production of ATP, and digestion of macromolecules) to take place in a controlled environment. However, a different type of organelles has also been identified (shown in Figure 1 and listed in Table 1). They are designated as membraneless organelles or biomolecular condensates and, even though they are not delimited by a membrane, they still function as individual compartments of the cell with the material properties of a liquid[7]. Examples include

the nucleolus[24-26], the stress granules[27-31], and the post-synaptic density[32-35]. Each of them has a well-defined function (see Figure 1 and Table 1) that is accomplished by concentrating, to restricted regions of the cell, only a subset of molecules from the ones available in the cytoplasm or the nucleoplasm.

Approximately 30 % of all human proteins show structural features that would promote their propensity to participate in *in vivo* LLPS[4,13]. In fact, continued advances in high-resolution microscopy and in cell biology techniques could uncover a great variety of previously unknown intracellular biomolecular condensates, each one with their own biological function[6,13]. Consequently, the identification and characterization of new intracellular membraneless compartments represents a step toward a more complete understanding of the cell's physiology.

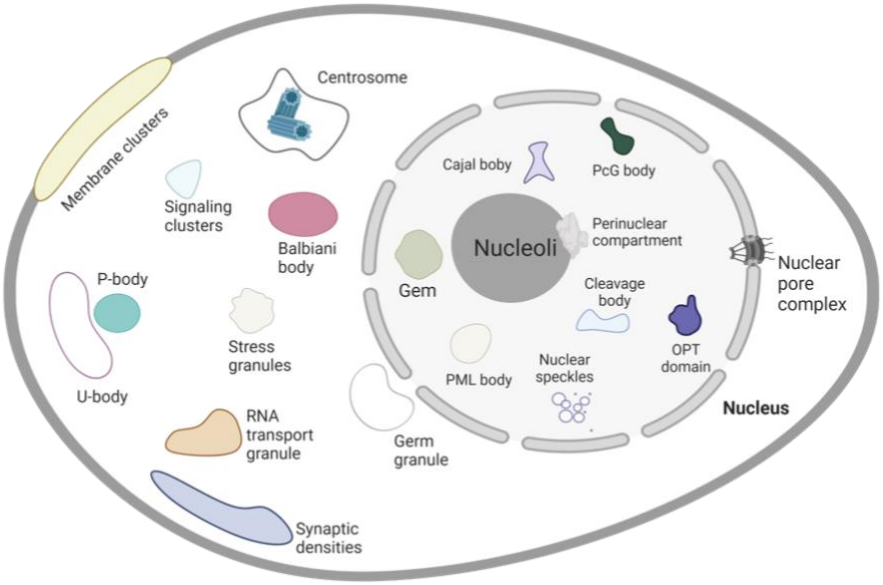


Figure 1 Intracellular distribution of the biomolecular condensates identified in eukaryotic cells thus far (adapted from [7]). *Created with BioRender.com.*

Table 1 List of biomolecular condensates described to this date with their intracellular localization and function (adapted from [7]).

Biomolecular Condensate	Subcellular Localization	Function	References
Actin patches	Plasma membrane	Endocytosis	36
Balbiani body	Cytoplasm	Storage	37,38
Cajal body	Nucleus	Assembly and/or modification of splicing machinery	39,40

Cleavage body	Nucleus	mRNA processing	41
Focal adhesions	Plasma membrane	Cell adhesion and migration	42
Gem	Nucleus	Storage; Aid histone mRNA processing	43,44
Germ granules	Cytoplasm	Storage	45-47
Histone locus body	Nucleus	Histone mRNA biogenesis	40,48
Nephrin clusters	Plasma membrane	Glomerular filtration barriers	49-51
Nuclear pore complex	Nuclear membrane	Nuclear import and export	52
Nuclear speckles	Nucleus	mRNA splicing	53
Nucleolus	Nucleus	Ribosome biogenesis	24-26
OPT domain	Nucleus	Transcriptional regulation	54,55
Paraspeckles	Nucleus	RNA processing	56,57
P-body	Cytoplasm	mRNA decay; mRNA splicing	29
PcG body	Nucleus	Transcriptional repression	58
PML bodies	Nucleus	Transcriptional regulation; apoptosis signaling; antiviral defense	59
Podosomes	Plasma membrane	Cell adhesion and migration	60
Postsynaptic densities	Cytoplasm	Neurotransmission	32-35
RNA transport granules	Cytoplasm	mRNA storage and transport	61
Stress granule	Cytoplasm	Translational regulation; mRNA storage	27-31
TCR clusters	Plasma membrane	Immune synapse	62,63
U-body	Cytoplasm	Storage and assembly of snRNPs	64

2.1.2 Biological Functions of Biomolecular Condensates

Recently, Lyon et al. published a review in which they describe in detail how liquid biomolecular condensates contribute to multiple biological process that take place in a cell. These mechanisms are divided into seven main categories: i) enhancement or suppression of biochemical reactions; ii) regulation of macromolecular folding state; iii) vectoral organization of biochemistry; iv) establishing mesoscale architecture; v) facilitating specific cellular localization; vi) buffering stochastic cellular noise; and vii) sensing and switching[6].

By definition, the process of LLPS implies a difference in solute concentration between the two phases that are formed. In fact, biomolecular condensates are generally enriched in certain molecules, when compared to the surrounding phase. However, it has been shown that these structures exclude specific biomolecules when the mesh created by interacting molecules restricts their entry to the condensed phase (due to the pore size or surface charge, for instance)[6,65]. Multiple reports have shown that this compositional difference between the condensed and dilute phase constitutes a highly regulated cellular mechanism that sustains the local rates of specific biochemical reactions (Figure 2)[33,63,66-70]. A well-characterized example of reaction rate enhancement through LLPS was identified in photosynthetic organisms. During the carbon fixation process (i.e., conversion of carbon into carbohydrates[71]), the carboxylation of ribulose biphosphate (RuBP) by the enzyme ribulose biphosphate carboxylase/oxygenase (Rubisco) constitutes the rate-limiting step[72]. By assembling biomolecular condensates that are enriched in both the enzyme and its substrates (RuBP and carbon dioxide), the limiting step of carbon fixation is accelerated[73]. Furthermore, Rubisco's competing substrate, oxygen, was found to be depleted from the condensates. This is another contributing factor that ameliorates the enzyme's efficiency for carbon fixation. With the same purpose, biomolecular condensates can also enhance enzymatic reactions by excluding their negative regulators[6]. Although only demonstrated *in vitro*, the T-cell receptor signaling clusters that form upon antigen recognition appear to be regulated by a process of LLPS. Following T-cell receptor activation, the linker for activation of T-cells (LAT) protein becomes phosphorylated[74], which is essential for the T-cell receptor signal transduction. *In vitro* studies demonstrated that this phosphorylated form of the protein has a propensity to undergo phase-separation[63]. In addition, it has been shown that LAT droplets exclude the phosphatase CD25 (probably through charge repulsion), with the objective of preventing the disassembly of the condensates due to LAT dephosphorylation[65]. In opposition to the examples described above, biomolecular condensates can also block reactions by keeping molecules away from their substrates[6]. For instance, in plants, under normal conditions, the restriction of auxin response transcription factors ARF7 and ARF19 to cytoplasmic condensates inhibits their activity in the nucleus[75]. However, an increase in auxin levels promotes ARF condensate disassembly and migration of the molecules to the nucleus, where they can perform their activity as transcription factors.

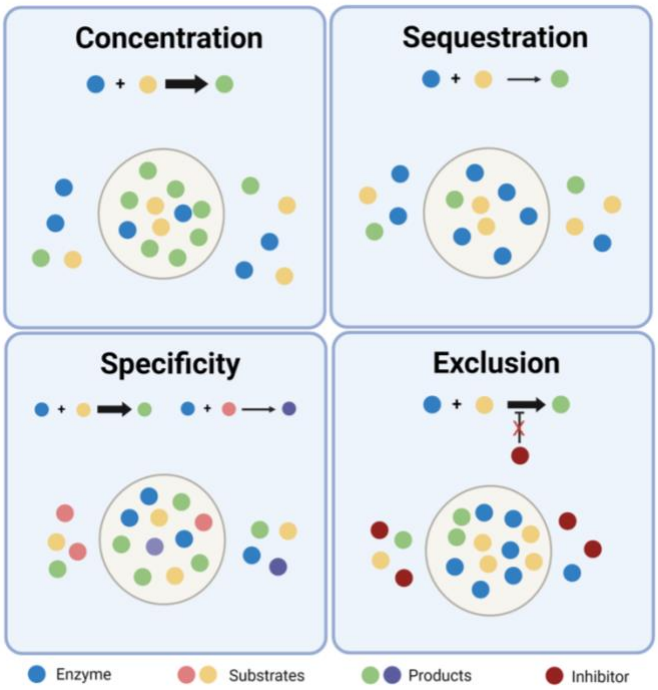


Figure 2 Proposed mechanisms for enzymatic rate regulation by biomolecular condensates (adapted from [6]). *Created with BioRender.com.*

Biomolecular condensates have also been implied in the regulation of macromolecule folding state, especially in the presence of external stressors (e.g., heat shock). In the cytoplasmic stress granules, for example, the RNA-binding protein G3BPI recruits long RNA molecules to the condensates, preventing the formation of misfolded RNA species[76,77]. This assumes particular importance for mRNA molecules, as translation may easily restart once the stress is absent if the polyribonucleotide molecule retains its conformation.

Intracellular compartments formed by LLPS might also regulate and orchestrate sequential biochemical reactions. For this, two features of liquid-liquid phase-separated solutions assume great relevance: i) a multiple component mixture can undergo phase-separation, resulting in multiple distinct dense phases, each one with the ability to concentrate a specific type of molecules (e.g., a different enzyme in a biochemical cascade); ii) once a biomolecule is altered by the activity of an enzyme, for instance, the resulting change in its physicochemical properties may lead to its concentration or removal from biomolecular condensates. The best-described example of this type of vectoral organization of biochemical reactions is the assembly of ribosomes in the nucleus. During this process, three concentric spherical liquid phases with distinct biomolecular compositions assemble in the nucleus[26,78-80]. In the most central compartment (i.e., the fibrillar centre), ribosomal DNA is transcribed. The resulting rRNA molecule moves to the following compartment (i.e., the dense fibrillar

component), where it undergoes translation. Finally, ribosomal assembly takes place at the external compartment (i.e., the granular compartment).

In addition to participating in the regulation of biochemical reactions, biomolecular condensates have been associated with processes that affect cellular function at a larger scale. The assembly of the postsynaptic density, a membraneless organelle localized to the postsynaptic membrane of neurons, is accomplished by LLPS[32-35]. Its major protein components (e.g., PSD-95, GKAP, Shank3, Homer1c or Homer3) undergo phase separation through a complex network of intermolecular interactions, acting as a bridge between the excitatory NMDA glutamate receptors and the cytoplasmic molecules that make up their signalling cascade.

The packaging of molecules into liquid condensates, which then associate with motor proteins to be transported throughout the whole cytoplasm is a viable mechanism by which the cell can efficiently regulate the distribution of its molecular components in its volume. In neurons, mRNA molecules (together with proteins) form liquid RNA transport granules that can be trafficked along the axon and ultimately reach the axonal terminus, which in some motor neurons, can be meters away[81-83]. Recently, it was shown that the connection between the RNA transport granules and the motor proteins might be mediated by lysosomes. The presence of annexin A11 in the condensates allows for their binding to the lysosome's membrane, which, in turn, is directly coupled to motor proteins[84].

A recent theoretical model postulates that biomolecular condensates serve as a buffering system for biomolecular concentration fluctuations, meaning that a variation in total concentration of a specific molecule with the ability to undergo LLPS (due to increased gene transcription or protein expression) would only alter the volume of the dense phase, while its concentration in both liquid phases would not change[6]. This would prevent any detrimental effect that might occur if the protein's concentration surpasses its solubility value, for instance.

Finally, solution conditions, such as temperature, pH, and salt concentration, strongly influence the highly sensitive process of phase transition. For this reason, it has been proposed that LLPS acts as a sensing mechanism that allows cells to respond accordingly to changes in their environment (e.g., heat shock or other stressors)[85,86].

2.1.3 Molecular Features that Promote Liquid-Liquid Phase Separation

It is well-established that some molecules have a higher propensity to liquid-liquid phase separate than others. In fact, the molecule's ability to participate in transient interactions with others (i.e., its multivalency) assumes a great importance for biomolecular condensate formation[4,7,8,13]. Proteins with multiple folded domains, proteins with intrinsically disordered regions (IDRs) or intrinsically disordered proteins (IDPs), and nucleic acids (specially RNA) are good candidates to undergo LLPS in biological environments.

For multidomain proteins, their LLPS behavior strongly depends on their number of interaction domains[4,13]. This was simply demonstrated by mixing protein constructs made up of SH3 domain repeats, with their known interaction partners, the proline-rich motifs (PRMs), at equimolar concentrations[50]. By enhancing the molecules' valency (i.e., by increasing the number of domains or motifs in each construct), there was a decrease in the saturation concentration for liquid-liquid phase separation[50].

Contrarily to proteins with multiple folded domains, IDPs and IDRs don't assume a well-defined folding[7]. Instead, they can adopt an array of tridimensional conformations that only differ slightly in their thermodynamic stability[4,13,87,88]. Normally, these polypeptides are enriched in specific polar and aromatic residues that favor an extended conformation in solution, including glycine, serine, glutamine, proline, glutamic acid, lysine, and arginine[89,90]. Although hydrophobic residues are known to promote high-order folding, they can also be found throughout the sequence of many IDPs/IDRs. The aromatic rings of tyrosine and phenylalanine residues, for instance, participate in charge-charge, charge-π, and π-π interactions, which have been shown to drive LLPS[91]. The primary structure of IDPs and IDRs determines their flexibility but also the intermolecular interactions that they can make, which ultimately dictates the physicochemical properties of the liquid phases they form. A variety of proteins that contain IDRs can undergo liquid-liquid phase separation both *in vitro* and *in vivo*, including the causative proteins of some neurodegenerative disorders [e.g., TDP-43[27] and FUS[9,92,93], for Amyotrophic Lateral Sclerosis (ALS) and Frontotemporal Dementia (FTD); tau[11,94], for Alzheimer's Disease (AD) and other Tauopathies; α-synuclein[12], for Parkinson's Disease (PD); and the exon1 fragment of huntingtin[10], for Huntington's Disease(HD)]. In specific cases, in addition to promoting the formation of a new liquid phase consisting of the causative proteins, IDRs might also be responsible for the liquid-to-solid transition that is observed during droplet aging[7,9,13,23,95-97]. This phenomenon is discussed in more detail in Section 2.2.

Posttranslational modifications are another tightly regulated mechanism for controlling the formation, composition, and stability of biomolecular condensates[13]. For instance, *in vitro*, methylation of arginines, which disrupts the residue's ability to participate in cation-π interactions, increases the saturation concentration of DDX4 protein[98]. Furthermore, the phosphorylation of different proteins can have an array of consequences for the biomolecular condensates: i) lead to an increase in the internal dynamics of the condensates[99]; ii) force the removal of the modified protein from the droplet[100,101]; iii) promote a complete dissolution of the condensate[102-104]; or iv) stimulate liquid-liquid phase separation when specific protein-protein interactions are involved[50].

Finally, RNA molecules can also act as scaffolds for the assembly of biomolecular condensates, particularly because of their length, flexibility, and valency to interact with other polynucleotides or proteins[4,105]. In fact, in addition to RNA being able to undergo phase

separation by itself, when added to a protein solution, the presence of RNA is sufficient to lower the saturation concentration for LLPS, in many cases[47,96,106].

2.2 Aberrant Liquid-Liquid Phase Separation in Neurodegeneration

In addition to the physiological relevance of phase transitions for cell function, there are accumulating evidences that abnormal LLPS occurs in a variety of pathologies[4,13,15,107,108]. Researchers have made great efforts to uncover the molecular processes that underlie normal to aberrant changes in the biomolecular condensates (summarized in Figure 3). Overall, three mechanisms were proposed: i) modification of the biomolecular condensate assembly process; ii) altered regulation of the phase separation; or iii) modification of the physicochemical properties of the intracellular environment[4]. Any of these alterations will subsequently lead to a phase separation behavior that is different from the one observed under normal physiological conditions, which can manifest through: an increase or decrease in the number or size of condensates; an ectopic formation of the droplets; a modification of the material properties of the biomolecular condensates; or a change in the components of the droplets[3,4].

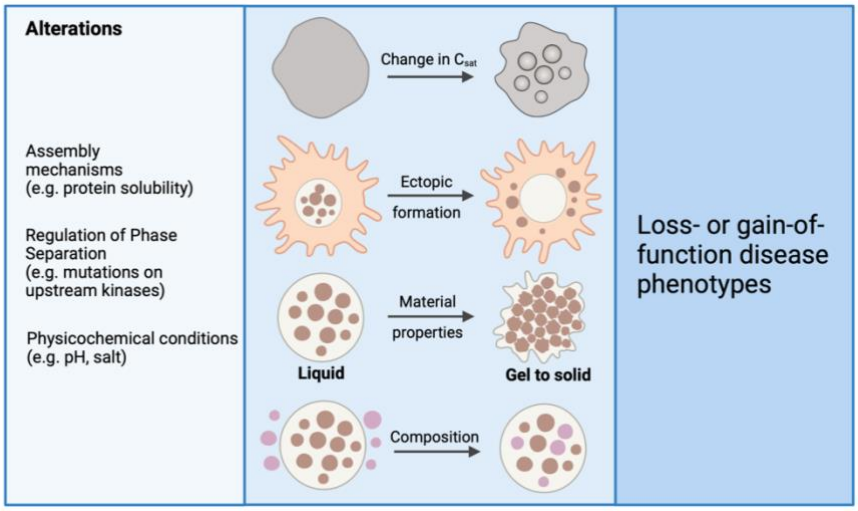


Figure 3 Summary of the effects of disease-associated alterations on biomolecular condensates, leading to aberrant LLPS in cells (adapted from [4]). *Created with BioRender.com*.

Neurodegenerative disorders are included in a class of diseases designated as proteinopathies. As so, they are all characterized by the accumulation of misfolded protein aggregates in the nervous system of patients. These are toxic species that ultimately disrupt the normal function of cells, tissues, and organs[3,4]. In the proposed protein aggregation

pathway, the disease causative protein loses its native conformation and becomes misfolded[109]. This can be due to disease-associated single gene mutations but, as most neurodegenerative disease cases are sporadic, often there is no genetic cause that can be identified[4]. The misfolded molecule is generally more aggregation-prone and, if it not detected and eliminated by the cellular protein quality control systems, it can sequentially form multiprotein assemblies that are progressively more complex and toxic (Figure 4). Firstly, a small number of monomers interact to form oligomers. These can further associate and lead to the development of fibrillar structures. When fibrils interact with each other they form large and insoluble aggregates that, in addition to the causative protein, can sequester other molecules from the surrounding environment, depriving the cell of many components that might be essential for their function[3]. Amyloid fibrils are a specific type of protein aggregate that are often present in neurodegenerative disease-affected cells[109,110] and specifically interact with the fluorescent dye thioflavin T (ThT), which allows for their quantification and visualization both *in vitro* and *in vivo*[111].

It was recently discovered that proteins with a high tendency to aggregate also phase separate *in vitro* and *in vivo*[3,4,8,13,15,23]. An important observation was that the droplets formed by these molecules are metastable and rapidly undergo a maturation process that converts them into less dynamic and more solid-like structures[15]. Indeed, the condensed phase droplets tend to lose their spherical shape and their capacity for a dynamic molecular exchange with the surrounding dilute phase [confirmed by fluorescence after photobleaching (FRAP) experiments] and can't completely fuse or relax upon contact with other droplets. These properties all indicate that the condensates are no longer of a liquid nature. A potential cause for this droplet aging is the formation of ß-sheet rich structures, resulting from the transition of weak and transient interactions to strong and stable ones[3,15]. Note that, this specific type of folding is also a hallmark of amyloid fibril formation[19]. For this reason, LLPS has been proposed to act as a preceding step to protein aggregation, and consequently as a mechanism involved in the first steps of neurodegenerative disease pathogenesis (Figure 4)[14].

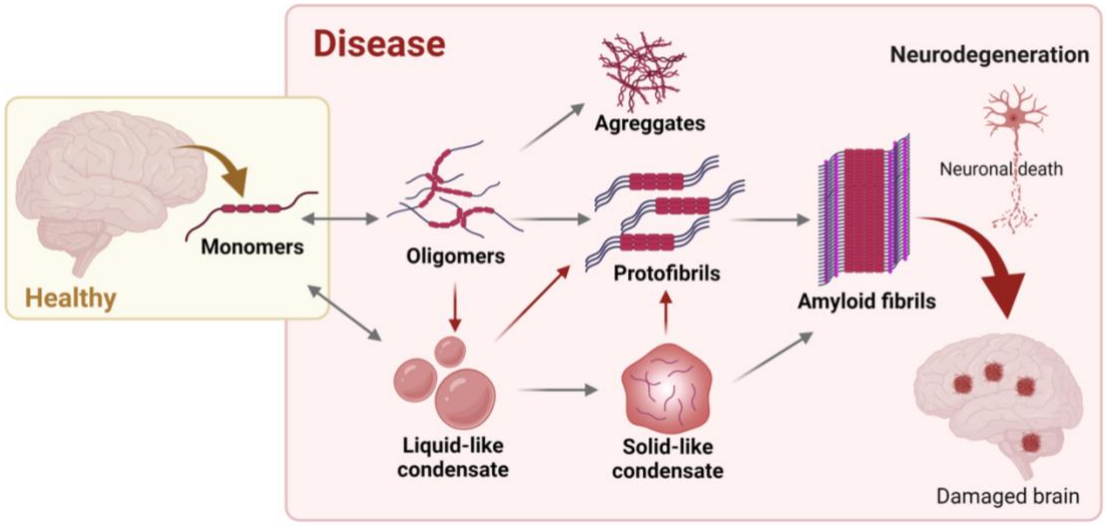


Figure 4 The proposed role for biomolecular condensates in the protein aggregation pathway, culminating in neurodegeneration (adapted from [8]). *Created with BioRender.com.*

Neurons appear to be especially susceptible to pathological effects resulting from aberrant phase transitions[4]. Firstly, these cells are postmitotic, meaning that they can't rely on cell division to asymmetrically distribute pathogenic condensates. Alterations in protein quality control mechanisms, which usually accompanies normal cellular aging, can also lead to the formation and accumulation of abnormal condensates. In addition, these cells have a high metabolic activity and require great amounts of ATP to maintain their function. For this reason, a drop in ATP levels might also impair the quality control processes which might contribute to the with formation of aberrant molecular assemblies. The molecular, morphological, and functional changes that occur during a neuron's lifetime are tightly coordinated by a complex posttranscriptional and translational control, which has been proposed to occur through LLPS. Consequently, when normal phase transition is affected, the cell's functioning becomes compromised. For the reasons described above, it isn't surprising that abnormal liquid-liquid phase separation has been shown to be involved in multiple neurodegenerative diseases, including ALS, FTD, tauopathies, and nucleotide repeat expansion disorders[112].

The following sections contain a detailed description of the current state of the art regarding the role of liquid-liquid phase separation in a specific subset of neurodegenerative diseases.

2.2.1 Amyotrophic Lateral Sclerosis and Frontotemporal Dementia

The involvement of aberrant liquid-liquid phase separation in the pathogenesis of neurodegenerative diseases is best-characterized for ALS and FTD. The RNA-binding proteins TDP-43, FUS, hnRNPA1, hnRNPA2, and TIA1 are often mutated in familiar forms of these pathologies and appear to be main players in pathogenesis of both diseases. Even for individuals

without the any disease, the presence of an external stressor might induce these molecules to assemble into stress granules, which are cytoplasmic liquid-like membraneless organelles[113-116]. Interestingly, it was shown that other stress granule components, such as PABPC1 and EIF4G1, colocalize to TDP-43 and FUS aggregates in the brains of patients[117]. The fact the membraneless organelles and the protein aggregates share similar biomolecular composition is compelling evidence that neurotoxic assembles arise from the irreversible conversion of liquid condensates into solid structures.

Some disease-causing mutations identified in patients with ALS change key properties of stress granules, including size, dynamics, and transport, which suggests that abnormal biomolecular condensate formation is associated with the disease's pathogenesis[83,116,118,119]. Furthermore, disease-associated mutations in the low-complexity regions of FUS, hnRNPA1, and TIA1 lead to a faster droplet maturation into solid-like structures *in vitro*[9,95,116,120]. Consequently, these mutant forms of the proteins may promote the formation of non-physiological condensates in cells that lead to toxicity, which is not observed in the healthy individuals.

The study of an additional set of mutations, particular to the nuclear localization signal of FUS, uncovered a new mechanism by which aberrant biomolecular condensates might form in a cell[121,122]. These mutations specifically affect the protein's interaction with Transportin[121]. When unable to attach to the nuclear import receptor, FUS remains restricted to the cytoplasm. There, FUS concentration becomes abnormally elevated and may surpass the saturation concentration, leading to phase separation even in the absence of an external stressor. If the protein concentration remains constant with no condensate disassembly, droplet maturation may occur leading to the possible development of toxic aggregates.

Besides the disease-causing mutants described above, abnormal posttranslational modifications may also cause pathological phase transitions of FUS and TDP-43[123]. Unmethylation of specific arginine residues in RGG/RG-rich portions of the FUS intrinsically disordered regions appears to enhance the interactions between the arginines and aromatic amino acids, leading to a significant increase in liquid-liquid phase separation propensity[92,122,124,125]. If the cellular quality control systems fail to promote the disassembly of these condensates that would not have formed under normal conditions, their aging into solid structures could cause toxicity. As TDP-43 is hyperphosphorylated both in ALS and in FTD[126,127], it would be relevant to determine the effects of this posttranslational modification in the protein's phase separation behavior.

2.2.2 Alzheimer's Disease and Tauopathies

AD is currently the most common neurodegenerative disease, and its pathological hallmarks include the extracellular deposition of amyloid plaques composed of the Aß peptide, and the intracellular accumulation of misfolded tau protein neurofibrillary tangles[128]. In addition to AD, other pathologies of the nervous system also share the common feature of tau protein aggregation. Together they are designated as Tauopathies. Non-pathogenic tau protein exhibits liquid-liquid phase separation behavior *in vitro*[129,130]. Tau is a microtubule-binding protein, and its condensate formation may be relevant for the assembly of new microtubules by concentrating tubulin dimers at specific nucleation sites[129]. As it was described in the previous section for ALS and FTD, specific disease-linked mutations or posttranslational modifications (e.g., hyperphosphorylation) can promote tau liquid-liquid phase separation in conditions that are not favorable for the phase transition of the normal protein[11,131]. If these aberrant droplets are not dissolved by the cell, hardening of the droplets could lead to toxic protein aggregation[11].

2.2.3 Parkinson's Disease

The accumulation of Lewis bodies due to α-synuclein aggregation is the primary hallmark of PD and other synuceinopathies. However, the biological events comprised between protein self-assembly and Lewis body formation are still unknown. Compelling evidence supporting that α-synuclein undergoes liquid-liquid phase separation has recently been reported by two different groups[12,132]. They show that weak hydrophobic interactions established between low complexity regions are responsible for droplet formation[12]. Although no physiological role for these condensates has been proposed to this day, the rapid maturation process of α-synuclein droplets *in vitro* and *in vivo* led the researchers to suggest that liquid-liquid phase separation acts as the biomolecular bridge that connects initial protein aggregation to the buildup of large inclusions in cells[12].

2.2.4 Huntington's Disease and other Repeat Expansion Disorders

The repeat expansion disorders are a group of diseases caused by an abnormal expansion of trinucleotide repeats in a specific gene beyond a critical length[133]. Two major types of liquid-liquid phase separating molecules can arise from the transcription and subsequent translation of the mutated gene: i) repeat RNAs[134,135]; and ii) repeat proteins[10,136]. The repetitive nature of these molecules makes them particularly prone to participate in multivalent interactions that has been shown to be necessary for liquid droplet assembly[4,7,8,13].

RNA molecules containing a repeat number superior to their critical threshold undergo liquid-liquid phase separation with an extremely rapid gelation process *in vitro*[137]. In living cells, these molecules assemble into nuclear foci, containing several proteins that are necessary for normal cell function (e.g., splicing factors), in addition to the phase separating polyribonucleotides[137].

HD is caused by an expansion of the polyQ tract of the huntingtin protein with more than 42 consecutive glutamine residues in its sequence[133,138]. In the recent years, Peskett et al. demonstrated that normal huntingtin can undergo liquid-liquid phase separation through intermolecular interactions between their polyQ regions[10]. This process can be reverted by addition of 10 % (w/v) 1,6-hexanediol revealing the hydrophobic nature of the interactions involved in droplet formation[10]. When the polyQ tract is expanded beyond the critical limit, the phase separation behavior becomes abnormal, and the aging of the condensates is accelerated[10]. Once the droplets mature, addition of 1,6-hexanediol is no longer sufficient to disassemble them[10]. Furthermore, the resulting solid-like structures strongly resemble the huntingtin aggregates that are present in the nervous tissue of HD patients[10]. As the polyQ expansion plays a key role in the aberrant phase transition of huntingtin, one can hypothesize that other pathogenic polyQ proteins (e.g., ataxin-3) may have a similar behavior *in vivo*.

RNA molecules also play a prominent role in polyQ droplet regulation. It was shown that different polyribonucleotides have distinct effects on condensate viscosity, dynamics, and propensity to fuse[136].

2.3 Machado-Joseph Disease and Ataxin-3

2.3.1 Overlook of Machado-Joseph Disease

MJD, also known as Spinocerebellar Ataxia type 3, is an autosomal dominant neurodegenerative disease that currently affects 1-5 per 100,000 people worldwide[16]. Although this prevalence classifies it as a rare disorder[139], MJD is the most common type of spinocerebellar ataxia[17-19] and the second most frequent polyQ expansion disorder, surpassed only by HD[19]. Its geographical distribution is rather heterogenous, with Portugal, and more specifically, the Azores Islands, constituting one of its primary incidence hotspots[17,140].

Similarly to the other polyglutamine diseases, MJD is characterized by an abnormally expanded stretch of repeated CAG triplets in the *ATXN3* gene (found in the long arm of

chromosome 14)[133,141]. This consequently results in a longer sequence of glutamine residues in the ataxin-3 protein[142]. In healthy individuals, the CAG repeat number varies between 12 and 44. However, *ATXN3* genes with more than 55 CAG repeats will inevitably lead to the development of the neurodegenerative disorder[1,19,20,143,144]. Furthermore, there is a clear negative correlation between repeat number and the age of disease onset[143].

The pathology's phenotypes are significantly heterogeneous, even when only individuals with the same number of repeats are being compared. Even so, specific patient-related factors, such as gender, genetic background, duration of the disease, and others at a more molecular level (e.g., protein interactors, cellular environment, modifying genes, gene polymorphisms) appear to play a role in dictating disease severity and symptomatology[145,146]. Clinically, patient segmentation is accomplished by a system developed by Coutinho & Andrade, which combines the age of disease onset and the progression rate with the most prominent symptoms to identify each type of the disease (see Table 2)[143,147]. Although gait ataxia and diplopia (i.e., double vision) are usually the first symptoms to be reported, other common clinical manifestations include ataxia (i.e., muscle control loss), chronic progressive external ophthalmoplegia (i.e., gradual paralysis of the muscles that control the movements of the eyes), dysarthria (i.e., speech impairments), dysphagia (i.e., swallowing difficulties), peripheral neuropathy, amyotrophy (i.e., loss of muscle mass), dystonia (i.e., involuntary contraction of the muscles) with rigidity, and distal muscle atrophies[148,149]. *Post mortem* analysis of the nervous system of MJD patients revealed that the major affected brain regions are, in fact, the ones responsible for the functions that are compromised (i.e., *substantia nigra*, cerebellum, pons, *medulla oblongata*, and the cranial nerves III to XII)[148-150]. The neuronal death is also accompanied by the intracellular accumulation of mutated ataxin-3 aggregates in the same regions[19,144]. For this reason, ataxin-3 has been proposed as the causative protein of MJD.

Table 2 Characterization of each subtype of Machado-Joseph disease (adapted from [143]).

Disease Subtype	Mean Age of Onset	Progression Rate	Prevalence	Primary Symptoms
Type I (Joseph Type)	23.4 years	Fast	Rare	Cerebellar ataxia, ophthalmoplegia, pyramidal (i.e., dystonia) and extrapyramidal signs
Type II (Thomas Type)	40.5 years	Intermediate	Most common	Cerebellar ataxia, ophthalmoplegia, with or without pyramidal signs
Type III (Machado Type)	46.8 years	Slow		Cerebellar ataxia, ophthalmoplegia, peripheral muscle weakness and amyotrophy, with or without pyramidal signs

2.3.2 Physiological and Pathological Roles of Ataxin-3

By definition, ataxin-3 is a mixed-folded protein: its N-terminal globular JD is connected to a structurally disordered C terminus composed of 2-3 UIMs (depending on the splicing variant) and the polyQ tract[21]. The length of the polyQ sequence and ultimately, the molecular weight of the protein, depends on the number of CAG repeats in the *ATXN3* gene[19]. For instance, the most common isoform of ataxin-3 (UniProt P54252 entry) is a 361 amino acid-long 42 kDa protein, with 3 UIMs and 13 consecutive glutamine residues[151-153].

As a deubiquitinating enzyme, ataxin-3 participates in the ubiquitin-proteasomal protein degradation pathway[154], which begins with the ATP-dependent activation of the E1 enzyme. Once activated, the E1 enzyme transfers its ubiquitin molecule to the ubiquitin conjugating enzyme E2. Next, the ubiquitin ligase enzyme E3 removes the ubiquitin molecule and attaches it to the target protein that must be eliminated from the cell. This process is repeated until the substrate has a chain of ubiquitin molecules connected by isopeptide linkages. At this point, ataxin-3 can use its isopeptidase activity to disassemble the poly-ubiquitin chain, rescuing the protein from degradation, and recovering the ubiquitin molecules so that they can be reused during the tagging of a different protein[155,156]. Both the JD and the UIMs are necessary for this

biological function of ataxin-3. In fact, the enzyme's peptidase activity derives from three specific amino acids contained in the JD (cysteine 14, histidine 199, and asparagine 134)[157,158]. Mutating any of these residues completely abolishes the protein's enzymatic activity. Furthermore, the first two UIMs of ataxin-3 are particularly involved in the detection and binding of specific types of poly-ubiquitin chains (i.e., lysine 48 or lysine 63-tagged), bringing them closer to the proteolytic JD[156]. This was confirmed when mutations in the leucine 229 and leucine 249 impaired the binding of the enzyme to its substrate. Similar mutation experiments revealed two more ubiquitin binding sites of the protein located in the JD[159].

In addition to its role in the regulation of protein degradation, ataxin-3 has been proposed to regulate the transcription process in cells. In fact, in its vast interactome, ataxin-3 has been shown to interact with a great number of transcription regulator factors, such as CBP[160], FOXO4[161], HDAC3 and 6[162,163], p300[164], PCAF[164], RAD23[165], and TAF4[166]. In addition, the presence of a leucine zipper motif in the sequence of ataxin-3 (residues 223 to 270) indicates that the protein might directly bind to DNA[163,167]. Finally, it was also shown that, through an interaction mediated by its polyQ tract, ataxin-3 can regulate histone acetylation and, consequently, repress transcription[164].

Apart from its physiological importance under normal conditions, great attention has been dedicated to understanding what the role of ataxin-3 in the pathogenesis of MJD. The polyQ expansion in the protein's sequence, resulting from an increase in CAG repeat number in the *ATXN3* gene, is a common feature to all MJD patients, which strongly indicates that this is, in fact, the main cause of this neurodegenerative pathology[17,146,150]. It has been proposed that the expanded polyQ segment changes the conformation of the protein, leading to distinct binding affinities, atypic subcellular distribution, loss of function, and protein aggregation[168]. Like for other neurodegenerative disorders, the aggregation mechanism of ataxin-3 is not fully characterized. However, particularly relevant insight came from the fact that both expanded and non-expanded forms of this protein undergo self-assembly *in vitro*[144]. While disease-associated ataxin-3 can generate amyloid-like fibrils, the protein with a normal polyQ length can only assemble into protofibrils, a mechanism that is reversible upon addition of SDS[20]. From these findings, a two-step aggregation pathway was proposed for ataxin-3 (shown in Figure 5). Shortly, the first aggregation step is mediated by an aggregation-prone region in the N-terminal JD (residues 73 to 96), which is common to both the expanded and non-expanded forms of the protein[169-172]. Self-assembly through this region of the protein is sufficient to convert ataxin-3 monomers into oligomers, and, finally, into protofibrils. In fact, shorter ataxin-3 constructs that only contain the JD also undergo this aggregation pathway. However, the second step of the aggregation pathway, which ultimately leads to the formation of amyloid-like fibrils, depends on the abnormally long polyQ tract, which is why it only occurs in the case of the mutated protein[20,170,173].

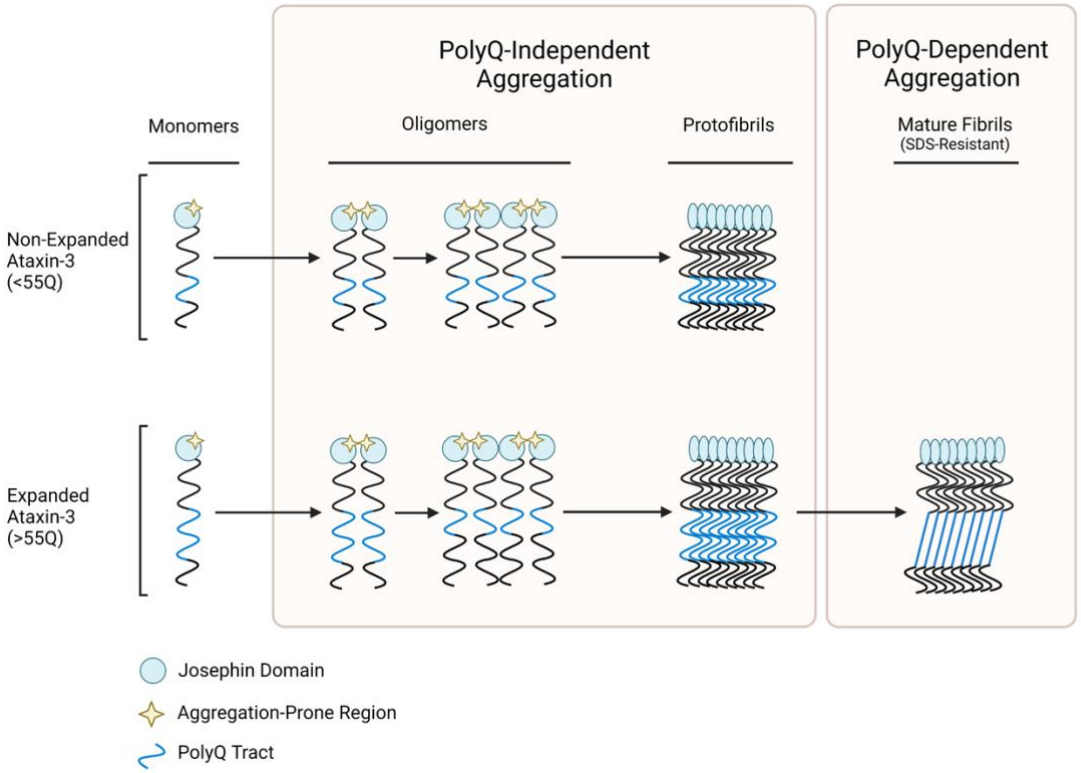


Figure 5 Schematic representation of the aggregation pathway of the non-expanded and expanded forms of ataxin-3 (adapted from [20]). *Created with BioRender.com*.

2.4 Liquid-Liquid Phase Separation of Ataxin-3

The liquid-liquid phase separation of ataxin-3 was first described by Murakami et al., who aimed to demonstrate that Raman microscopy can be used to determine protein concentration in both condensed and dilute phases, and to identify the molecular components contained inside of the protein droplets[1]. The protein construct that was used had a polyQ stretch of 28 glutamine residues (ataxin-3 28Q), which is still in the normal range. To induce ataxin-3 28Q phase separation, the presence of a crowding agent (e.g., PEG or dextran) was necessary at a minimum concentration of 10 % (w/v). In addition, a high concentration of protein was used (i.e., 100 μM) to perform these studies. The authors concluded that the liquid-liquid phase separation behavior of ataxin-3 28Q is not as strong as the one reported for other neurodegenerative disease-associated proteins[1]. For instance, FUS forms liquid droplets at lower concentrations (e.g., 5 μM, which is close to the protein's physiological concentration),

even in the absence of a crowding agent[125]. However, for LLPS experiments with huntingtin exon1, which is also a polyQ protein and might undergo phase separation through a similar process to ataxin-3 28Q, 10 % (w/v) dextran and 100 μM protein (with 25 glutamine residues in the polyQ tract) were also required for the *in vitro* experiments[10].

Monitorization of ataxin-3 28Q droplets formation was accomplished through turbidity measurements, microscopy analysis (namely fluorescence, brightfield, and Raman microscopy), and FRAP assays. The first set of results presented in this paper reveal that the JD does not undergo condensation on its own[1]. This suggests that the phase transition processes of liquid-liquid phase separation and protein aggregation occur through different molecular assembly mechanisms, as the aggregation prone region in the folded N terminus of ataxin-3 is involved in the first steps of the protein's aggregation pathway[169-172]. The authors also propose that droplet formation relies on hydrophobic interactions[1] (similarly to huntingtin exon1[10]), as an raising the sodium chloride concentration from 0 mM to 150 mM led to an increase in the solution's turbidity. In addition, in the presence of 10 % (w/v) 1,6-hexanediol there is a reduction in the turbidity levels to around 50 % of the original value[1]. As these results are not supplemented with microscopy images, we cannot draw conclusions about the nature of the particles that resist to the presence of 1,6-hexanediol (i.e., if they have liquid- or solid-like properties). The FRAP assays showed that, in the presence of 20 % (w/v) PEG, the droplets have a gel-like nature, as they only recover to around half of the original intensity[1]. However, no information is given about the time interval that takes place between sample preparation and the measurements, not excluding the possible effects of droplet aging on the results. Finally, from the spectra obtained by Raman microscopy, the authors drew two main conclusions: i) protein concentration in the condensed phase depends on crowding agent concentration; ii) the crowding agent molecules localize only to the dilute phase, without being recruited to the ataxin-3 28Q droplets[1].

The fact that only one paper has been published about ataxin-3 liquid-liquid phase separation, highlights that this is a field in its preliminary stages and that additional fundamental level experiments are essential to further determine why and how this phenomenon may occur in biological systems. Furthermore, the possibility of a relationship between liquid-liquid phase separation and ataxin-3 aggregation should be studied, as this is observed for other proteins implicated in other neurodegenerative disorders. The characterization of changes on phase separation becomes altered in the presence of the expanded ataxin-3 would also help to elucidate the abnormal biological events that occur in the neurons of MJD patients.

2.5 Experimental Approaches to Study Liquid-Liquid Phase Separation *In Vitro*

There are some important properties that phase-separated droplets must possess to confirm that they are, in fact, of liquid nature (see Figure 6). Firstly, due to the interface tension that established between liquids with different compositions and material properties (i.e., viscosity, density), droplets should have a perfectly spherical shape[3,6,174,175]. Any geometrical alterations may occur as a consequence of gelation or droplet maturation, when they progressively become more solid-like[9,10]. Second, when two droplets become in contact, they should fuse and relax, giving rise to a bigger spherical droplet whose volume is equal to the sum of the volume of each individual droplet[6,175]. Under some conditions, droplet fission might also take place. Similar to fusion, the resulting droplets must be spherical and a conservation of mass should be observed. Furthermore, as it is a thermodynamic phenomenon, liquid-liquid phase separation is a reversible process[2,3,175]. For this reason, a specific change in the environmental conditions (for example the decrease in protein concentration for any protein; an increase in temperature[176]; or a disruption of hydrophobic interactions by the addition of 1,6-hexanediol[10]) should result in a complete dissolution of the condensed phase. For instance, when droplet aging has already occurred, solid aggregates will remain in their place and will not disassemble[9,10]. Finally, it must be shown that molecules move freely inside of a droplet and that they are able to exchange with the surrounding dilute phase, as this is a fundamental property of liquids[4,175]. FRAP assays, which are explored in detail in Section 2.5.5, are generally used for the evaluation of the molecular dynamics inside of droplets.

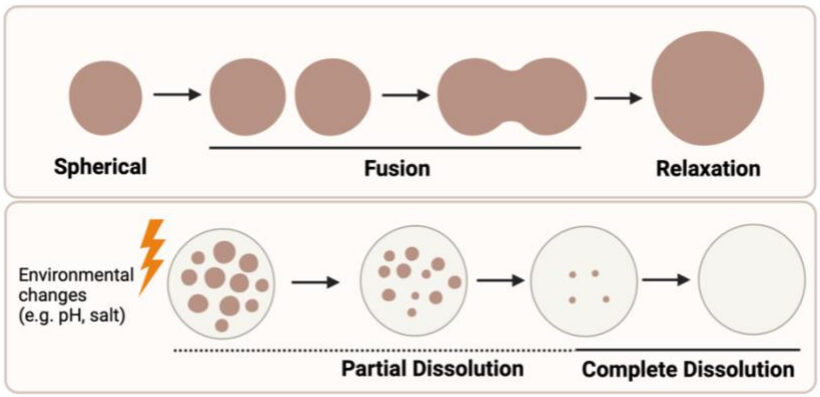


Figure 6 Schematic representation of fundamental properties of liquid-like droplets. *Created with BioRender.com.*

A combination of the methods described below can be used to fully characterize the phase separation behavior of any protein system (e.g., determination of droplet number, size, morphology, composition, and material properties) *in* vitro. Moreover, these methods can also be used to evaluate the effect of specific environmental conditions (e.g., crowding, protein concentration, temperature, pH, ionic strength, RNA concentration, presence of a binding partner, etc.) on condensate dynamics.

2.5.1 Sedimentation Assay

The sedimentation assay is a simple method, commonly used for a quantitative analysis of the compositional differences between the dilute and condensed phase that form upon liquid-liquid phase separation[177]. The protocol (shown in Figure 7) begins with the induction of the liquid-liquid phase separation, which can be achieved with different stimuli, depending on the protein that is being studied (e.g., ionic strength or temperature changes, addition of a crowding agent, etc.). This is followed by a short centrifugation, that separates the supernatant, containing the dilute phase, from the pellet that contains the condensed phase. Generally, the pellet is resuspended in the used buffer to the same final volume as of the supernatant and both samples are resolved by sodium dodecyl sulfate-polyacrylamide gel electrophoresis (SDS-PAGE). Finally, by comparing the intensity of the bands in both samples it is possible to determine the protein partitioning ratio.

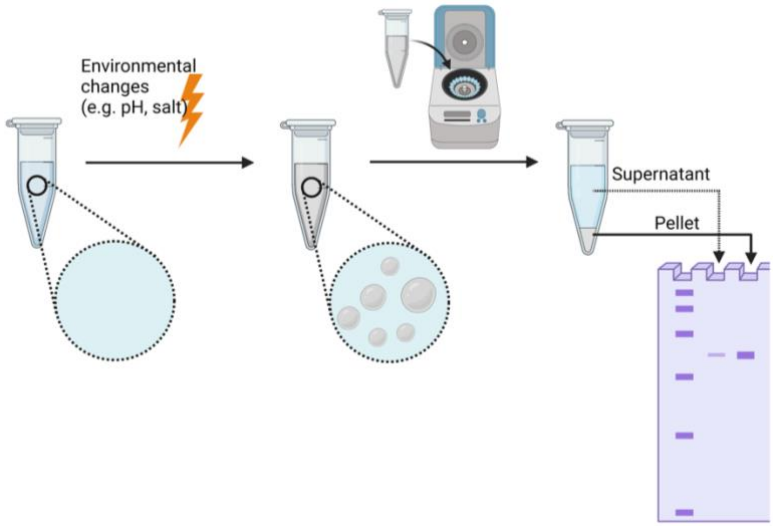


Figure 7 Schematic representation of the protocol used for sedimentations assays. *Created with BioRender.com.*

In addition to being rather fast and straightforward, this method can be used to describe the liquid-liquid phase separation of multi-protein systems, as molecules with different molecular weights will migrate differently in the SDS-PAGE gel. However, this method alone

does not distinguish between phase-separated droplets with liquid nature from solid protein aggregates, as both of these particles will deposit in the bottom of a tube during centrifugation. For this reason, a visual method, such as imaging by microscopy, should be used to complement the results obtained in a sedimentation assay.

2.5.2 Turbidimetry

The droplets that form upon liquid-liquid phase separation usually have diameters comprised between tens to hundreds of diameters. For this reason, if a solution has undergone phase separation, it will disperse visible light. The degree of this scattering can be quantified through optical density measurements, usually at wavelengths of 340 nm, 405 nm, or 600 nm[175,177,178]. The obtained turbidity value will depend on the number and size of the particles contained in the sample. This technique is commonly used to determine a protein's saturation concentration for liquid-liquid phase separation. It can also be used to evaluate the environmental conditions (e.g., temperature, salt concentration, pH, etc.) that promote the occurrence of a phase transition. A major disadvantage of turbidimetry assays for the characterization of protein liquid-liquid phase separation is the inability to differentiate the shape, size, or assembly mechanism (i.e., LLPS vs. protein aggregation) of the particles present in the analyzed solution[175]. For this reason, and similarly to the sedimentation assay, turbidity measurements should also be coupled to with a visual method, such as microscopy.

2.5.3 Dynamic Light Scattering

In opposition to the turbidimetry method described in the previous section, dynamic light scattering (DLS) is used to measure the size distribution of the particles in a liquid sample through time[179-182]. Because of this, it is possible to draw conclusions about the nucleation process that occurs in this thermodynamic phenomenon. For instance, if in a specific protein system nucleation is fast and takes place only in a short time frame, droplet size distribution will be low. On the other hand, if nucleation continues throughout time, there will be a high variability in particle size. Furthermore, using DLS, one can determine if the protein droplets are growing with time (i.e., due to fusion events or by recruiting more molecules into them), or if their size becomes constant once they are formed. It should, however, be noted that this

method does not distinguish between different types of particles, and that is why it is usually performed together with microscopy experiments.

2.5.4 Microscopy

Visual observation of droplets through microscopy experiments remains the golden standard for liquid-liquid phase separation characterization[175]. In fact, it is commonly used to complement the quantitative data that is obtained from the methods described previously, as it is the only technique that allows for the direct visualization and morphological description of the particles that form upon phase transitions. Different acquisition modes can be used for droplet imaging, including brightfield, differential interference contrast (DIC), and fluorescence microscopy[175,177,182]. This last example, in addition to provide information regarding the shape and number of the particles, can be used to estimate the protein concentration in the condensed phase, as well as to study the colocalization of different molecules into the same droplet if each one is labelled with its own fluorophore. In some cases, spontaneous fusion events are also observed, confirming the liquid nature of the particles. Nevertheless, for most cases, only a specific field at a chosen focus plane is analyzed, which means that information from the rest of the sample is lost. In fact, the increase in droplet number that is often observed in microscopy images in not due to new nucleation events, but because the particles tend to deposit to the bottom of the well or to the surface of the microscope slide with time.

2.5.5 Fluorescence Recovery After Photobleaching

Fluorescence recovery after photobleaching (FRAP) is the primary technique used to uncover the material properties of phase-separated droplets[175,177,182]. Using a confocal microscope equipped with the appropriate laser, which depends on the specific fluorophore that is being used, a specific region of interest of the fluorescently labelled protein-containing droplet is bleached and the recovery in fluorescence intensity is analyzed (Figure 8). When recovery is fast, the molecules inside of the droplet are highly dynamic, characteristic of a liquid-like material. Incomplete and slow recovery indicate the presence of gel-like droplets. Finally, solid protein aggregates will not show any fluorescence recovery after photobleaching. For this reason, the effect of aging in the material properties of the condensates can be studied with FRAP assays. Two distinct types of bleaching methods can be implemented. First, when the entire droplet is photobleached, a fast signal recovery indicates that the fluorescent molecules of the dilute phase are capable of exchanging with the bleached molecules of the

condensed phase. On the other hand, when a particular area of the droplet is bleached, the molecular dynamics inside of the droplet also contribute to the recovery of the fluorescence. When performing FRAP experiments, one should take into consideration that the recovery rate depends on the volume of the droplet and, also, on the size of the bleached area[175]. For these reasons, it is recommended that these parameters are kept constant between experiments.

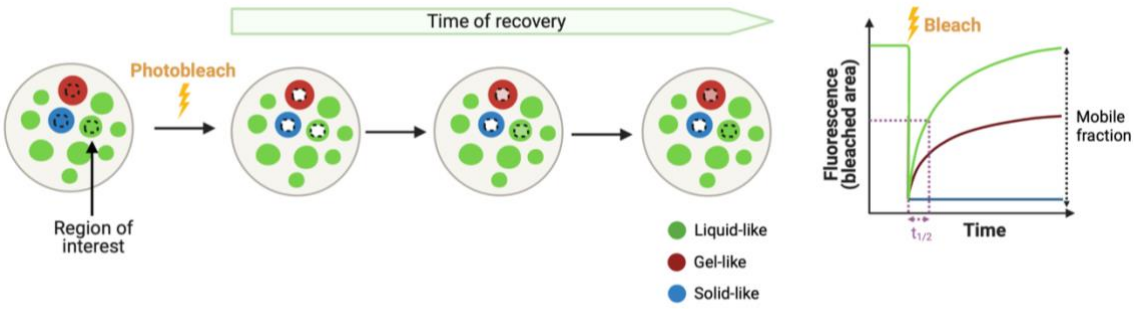


Figure 8 Schematic representation of a FRAP experiment with condensates of different material properties. The mobile fraction corresponds to the plateau at which the fluorescence intensity stabilizes following photobleaching. $t_{1/2}$ represents the halftime of recovery which is defined as the time interval between bleaching and the moment at which the fluorescence intensity is equal to half of its final value. *Created with BioRender.com*.

Chapter 3

Materials and Methods

3.1 Materials

3.1.1 Bacterial Strains

Table 3 List of the bacterial strains used for the experiments described in the following sections.

Bacterial Strain	Application	Genotype	Methods Section
E. coli DH5α	Plasmid Replication	F- endA1 glnV44 thi-1 recA1 relA1 gyrA96 Φ80dlacZΔM15 deoR Δ(lacZYA-argF) U169 nupG, hsdR17(rK- mK+), λ-	3.2.1 3.2.2
E. coli BL21 (DE3)-SI	Protein Expression	F- ompTIon hsdSB (rB-, mB-) gal dcm endA1 proUp::T7 RNAP::malQ-lacZ (TetS)	3.2.1 3.2.3

3.1.2 Cell Culture Media

Table 4 List of the cell culture media used for the experiments described in the following sections.

Medium	Composition	Methods Section
Luria-Bertani medium (LB)	1 % (w/v) Tryptone 0.5 % (w/v) Yeast Extract 1 % (w/v) NaCl	3.2.1 3.2.2
Luria-Bertani medium plates (LB)	1 % (w/v) Tryptone 0.5 % (w/v) Yeast Extract 1 % (w/v) NaCl 1.5 % (w/v) Agar	3.2.1 3.2.2
Super Optimal Broth medium (SOB)	2 % (w/v) Tryptone 0.5 % (w/v) Yeast Extract 10 mM NaCl 2.5 mM KCl 10 mM $MgSO_4 \cdot 7H_2O$ 10 mM $MgCl_2 \cdot 6H_2O$	3.2.1.
Luria-Bertani medium without NaCl (LB_{ON})	1 % (w/v) Tryptone 0.5 % (w/v) Yeast Extract	3.2.3
Luria-Bertani medium plates without NaCl (LB_{ON})	1 % (w/v) Tryptone 0.5 % (w/v) Yeast Extract 1.5 % (w/v) Agar	3.2.3.
Induction medium	2 % (w/v) Tryptone 1 % (w/v) Yeast Extract 5 M NaCl	3.2.3.

3.1.3 Buffer Solutions

Table 5 List of the buffer solutions used for the experiments described in the following sections.

Buffer	Composition	Methods Section
Transformation Buffer	10 mM HEPES pH 6.7 15 mM $CaCl_2 \cdot 2H_2O$ 250 mM KCl 55 mM $MnCl_2 \cdot 4H_2O$	3.2.1
Buffer A	20 mM PO_4^{2-} pH 7.5 500 mM NaCl 20 mM Imidazole 2.5 % (v/v) Glycerol	3.2.3 3.2.4
Buffer B	20 mM PO_4^{2-} pH 7.5 500 mM NaCl 500 mM Imidazole 2.5 % (v/v) Glycerol	3.2.4
Storage Buffer	20 mM PO_4^{2-} pH 7.5 150 mM NaCl 5 % (v/v) Glycerol 2 mM EDTA 1 mM DTT	3.2.4
Loading Buffer	200 mM PO_4^{2-} pH 6.8 20 % (v/v) Glycerol 10 % SDS 50 µg/mL	3.2.5
Running Buffer	25 mM Tris-HCl pH 8.3 192 mM Glycine 0.1 % SDS	3.2.5
LLPS Buffer (in PO_4^{2-})	50 mM PO_4^{2-} pH 7.5 < 1 % (v/v) Glycerol	3.2.6 3.2.7 3.2.8
LLPS Buffer (in HEPES)	50 mM HEPES pH 7.5 < 1 % (v/v) Glycerol	3.2.6 3.2.7 3.2.8

3.1.4 Ataxin-3 Constructs and Plasmids

For this study, different constructs expressing truncated and full-sequence versions of ataxin-3 were used. The protein sequence of each variant, highlighting each specific domain is detailed bellow.

Ataxin-3 D1



MSYYHHHHHHLENLYFQGMESIFHEKQEGSLCAQHCLNNLLQGEYFSPVELSSIAHQLDEEERMRMAEGGVTS
EDYRTFLQQPSGNMDDSGFFSIQVISNALKVWGLELILFNSPEYQRLRIDPINERSFICNYKEHWFTVRKLGKQW
FNLNSLLTGPELISDTYLALFLAQLQQEGYSIFVVKGDLPDCEADQLLQMIRVQQMHRPKLIGEELAQLKEQRV
HKTDLERVLEANDGSGMLDEDEEDLQRALALSRQEIDMEDEEADLRRAIQLSMQGSSR

Ataxin-3 13Q



MSYYHHHHHHLENLYFQGMESIFHEKQEGSLCAQHCLNNLLQGEYFSPVELSSIAHQLDEEERMRMAEGGVTS
EDYRTFLQQPSGNMDDSGFFSIQVISNALKVWGLELILFNSPEYQRLRIDPINERSFICNYKEHWFTVRKLGKQW
FNLNSLLTGPELISDTYLALFLAQLQQEGYSIFVVKGDLPDCEADQLLQMIRVQQMHRPKLIGEELAQLKEQRV
HKTDLERVLEANDGSGMLDEDEEDLQRALALSRQEIDMEDEEADLRRAIQLSMQGSSRNISQDMTQTSGTNLTS
EELRKRREAYFEKQQQKQQQQQQQQQQGDLSGQSSHPCERPATSSGALGSDLGDAMSEEDMLQAAVTMSLE
TVRNDLKTEGKK

GFP-Ataxin-3 13Q



MSHHHHHHGSKGEELFTGVVPILVELDGDVNGHKFSVSGEGEGDATYGKLTLKFICTTGKLPVPWPTLVTTFS
YGVQCFSRYPDHMKRHDFFKSAMPEGYVQERTISFKDDGNYKTRAEVKFEGDTLVNRIELKGIDFKEDGNILGH
KLEYNYNSHNVYITADKQKNGIKANFKIRHNIEDGSVQLADHYQQNTPIGDGPVLLPDNHYLSTQSALSKDPNE
KRDHMVLLEFVTAAGITHGMDELYKQASNSAVDGTAGPGSINMESIFHEKQEGSLCAQHCLNNLLQGEYFSPV
ELSSIAHQLDEEERMRMAEGGVTSEDYRTFLQQPSGNMDDSGFFSIQVISNALKVWGLELILFNSPEYQRLRIDPI
NERSFICNYKEHWFTVRKLGKQWFNLNSLLTGPELISDTYLALFLAQLQQEGYSIFVVKGDLPDCEADQLLQMI
RVQQMHRPKLIGEELAQLKEQRVHKTDLERVLEANDGSGMLDEDEEDLQRALALSRQEIDMEDEEADLRRAIQL
SMQGSSRNISQDMTQTSGTNLTSEELRKRREAYFEKQQQKQQQQQQQQQGDLSGQSSHPCERPATSSGAL
GSDLGDAMSEEDMLQAAVTMSLETVRNDLKTEGKK

Table 6 Relevant physicochemical parameters for the purification of ataxin-3 constructs computed by ProtParam.

Ataxin-3 Construct	Molecular Weight (kDa)	Isoelectric Point	Extinction Coefficient* (M^{-1} cm^{-1})
Ataxin-3 D1	32.58	4.85	30160
Ataxin-3 13Q	43.58	4.86	31650
GFP-Ataxin-3 13Q	70.52	5.12	49195

*Assuming all pairs of Cys residues form cystines.

Table 7 List of the plasmids used for the experiments described in the following sections.

Ataxin-3 Construct	Plasmid	Induction	Resistance
Ataxin-3 D1	pDEST17_His6_Atx-3 D1	NaCl (300 mM)	Ampicillin
Ataxin-3 13Q	pDEST17_TevG_Atx-3 13Q	NaCl (300 mM)	Ampicillin
GFP-Ataxin-3 13Q	pDEST17_HisGFP_Atx-3 13Q	NaCl (300 mM)	Ampicillin

3.2 Methods

3.2.1 Preparation of Competent Cells

For this work, two strains of *Escherichia coli* cells were used: DH5α and BL21 (DE3)-SI. Cells were plated on Luria-Bertani (LB) medium and incubated overnight at 37 ℃. On the following day, a single cell colony was inoculated into 30 mL of LB medium in a 250 mL baffled flask. The flask was incubated for 6-8 hours at 37 ℃ and 250 rpm vigorous shaking (starter culture) in an IKA® KS 4000 I-Control incubator shaker (Shaker, IKA). At the end of this incubation period, 150 µL, 500 µL or 750 µL of the starter culture were transferred to one of three 2 L baffled flasks containing 250 mL of Super Optimal Broth (SOB) medium. The cultures were then kept overnight at 18 ℃ and 200 rpm shaking. On the next morning, the optical density of the three cultures was measured at 600 nm (OD_{600nm}) and the one that had not yet reached 0.6 was chosen for the following steps. Once the OD_{600nm} of this culture reached the desired value, (optimally 0.6, but a value between 0.1-1 is still acceptable), the cell culture was kept on ice for 10 minutes. From this step onward, the protocol was performed at 4 ℃ or on ice. After the cell culture was cooled down, the 250 mL were divided into 50 mL falcons and centrifuged for 10 minutes at 4 ℃ and 2500 ×g (Sorvall ST 40, Thermo Fischer Scientific). The supernatant was discarded, and the pellet was carefully resuspended in a total of 80 mL of transformation buffer (10 mM HEPES, pH 6.7, 15 mM $CaCl_2 \cdot 2H_2O$, 250 mM KCl, 55 mM $MnCl_2 \cdot 4H_2O$). The resuspension was kept on ice for 10 minutes and then centrifuged for 10 minutes at 4 ℃ and 2500 ×g (Sorvall ST 40, Thermo Fischer Scientific). Once again, the supernatant was removed, and the pellet was carefully resuspended in a total of 20 mL of transformation buffer. DMSO was slowly added to the resuspension to a final concentration of 7 % (v/v). Finally, the resuspension was kept on ice for 10 minutes and divided into 100 µL aliquots, which were flash-frozen using liquid nitrogen and stored at -80 ℃.

3.2.2 Plasmid DNA Replication

Escherichia coli DH5α cells were transformed with each encoding the ataxin-3 variants (ataxin3 D1, ataxin-3 13Q, or GFP-ataxin-3 13Q), by heat shock at 42 ℃ for 45 s. The transformed cells recovered in LB medium at 37 ℃, 180 rpm for 1 h and were subsequently plated on LB plates supplemented with 100 µg/mL Ampicillin. These were kept at 37 ℃ overnight. On the next day, an isolated colony was inoculated in 10 mL of LB medium supplemented with 100 µg/mL Ampicillin in a 50 mL falcon. The cell culture was grown

overnight at 37 ℃ and 180 rpm shaking (IKA, Shaker). The following day, the cells were harvested by centrifugation for 10 minutes at 4 ℃ and 3500 rpm (Sorvall ST 40, Thermo Fischer Scientific) and plasmid DNA was with the NZYMiniprep Kit (NZYTech Gene and Enzyme), according to the manufacturer's protocol. The final plasmid concentration was determined by measuring the absorbance at 260 nm using a NanoDrop 1000 spectrophotometer (Thermo Scientific). The purity of the sample was also confirmed by measuring the A_{260nm}/A_{280nm} ratio. The plasmid solution was stored at -20 ℃ until required.

3.2.3 Expression of the Ataxin-3 Constructs

Escherichia coli BL21 (DE3)-SI cells were transformed with the plasmid corresponding to the desired ataxin-3 construct (ataxin3 JD, ataxin-3 13Q, or GFP-ataxin-3 13Q) by heat shock at 42 ℃ for 45 s. The transformed cells recovered in Luria-Bertani medium without NaCl (LB_{ON}) at 37 ℃ for 1 h. Subsequently, they were plated on LB_{ON} plates supplemented with 100μg/mL Ampicillin and incubated at 37 ℃ overnight. On the next day, five isolated colonies were inoculated in 150 mL of LB_{ON} medium supplemented with 100μg/mL Ampicillin in a 500 mL baffled flask. Cells were grown overnight at 37 ℃ and 180 rpm shaking (IKA, Shaker). On the following day, 20 mL of the pre-culture were transferred to a 2 L baffled flask containing 450 mL of LB_{ON} medium, supplemented with 100 μg/mL Ampicillin and 0.4 % (w/v) Glucose. The culture was kept at 37 ℃ and 180 rpm shaking (IKA, Shaker) until the OD_{600nm} reached 0.8, and then cooled to 30 ℃. Protein expression was induced by an increase in NaCl concentration to 300 mM. For this, 50 mL of Induction Medium (2x LB_{ON} medium, 3M NaCl) were added to the culture, which was once again supplemented with 100 μg/mL of Ampicillin. After 3 hours of expression at 30 ℃ and 180 rpm shaking (IKA, Shaker), the cells were harvested by centrifugation at 4 ℃ and 4000 rpm for 25 minutes (Beckman Avanti J26 XP, JLA8.1000 rotor). The pellet was resuspended in 30 mL of ice-cold buffer A [20 mM PO_4^{2-}, pH 7.5, 500 mM NaCl, 20 mM Imidazole, 2.5% (v/v) Glycerol] per litre of cell culture supplemented with 50 μg/L lysozyme and stored at -20 ℃ until protein purification. The protein expression was confirmed by SDS-PAGE analysis.

3.2.4 Purification of the Ataxin-3 Constructs

The cell suspension was thawed, and lysis was induced by addition of 50 μg/mL lysozyme, 0.2 mg/mL DNAse, 0.02 mg/mL RNAse, 1 mM $MgCl_2$, 1 mM PMSF with mild agitation on ice for 1 hour. The cell lysate was centrifuged for 45 minutes at 4 ℃ and 17000 rpm (Beckman Avanti J-26 XP, JA25.50 rotor). The supernatant was filtered with a 0.45 μm PVDF filter (Whatman) and loaded to a pre-equilibrated Ni^{2+}-charged HiTrap™ IMAC HP 5 mL Column (GE Healthcare) The column was washed with ice-cold buffer A [20 mM PO_4^{2-}, pH 7.5, 500 mM NaCl, 2.5% (v/v) Glycerol, 20 mM Imidazole] and connected to the AKTA Prime Plus (GE Healthcare) chromatography system. Elution of the ataxin-3 variants was induced by a step gradient of 10 %, 50 % and 100 % elution buffer B [20 mM PO_4^{2-}, pH 7.5, 500 mM NaCl, 2.5% (v/v) Glycerol, 500 mM Imidazole], with exception of GFP-ataxin-3 13Q. For the purification of this variant, the 10 % (i.e., final concentration of 68 mM Imidazole) step was excluded, as a great amount of the protein of interest detached from the column even at this low concentration of Imidazole. The fractions containing the protein of interest were pooled together and filtered with a 0.22 μm low protein binding PVDF filter (Millipore Corporation). Next, the protein sample was loaded to a size exclusion chromatography (SEC) column (HiPrep™ 26/60 Sephacryl® S300 HR Column, GE Healthcare) adapted to the AKTA Prime Plus chromatography system. The isocratic elution of protein was done in storage buffer [20 mM PO_4^{2-}, pH 7.5, 150 mM NaCl, 5% (v/v) Glycerol, 2 mM EDTA, 1 mM DTT], and monitored by optical density at 280 nm. The fractions containing ataxin-3 with the highest degree of purity were pooled together and concentrated using an Amicon Ultra-15 concentrator (Millipore Corporation) with a 10 or 30 kDa cut-off. The MWCO was chosen considering the molecular weight of the purified protein (see Table 6). The protein concentration of the final sample was determined by measuring the absorbance at 280 nm using a NanoDrop 1000 spectrophotometer (Thermo Scientific) using the theoretical molar extinction coefficient predicted for each ataxin-3 construct (see Table 6). Finally, the purified protein sample was aliquoted, flash-frozen with liquid nitrogen and stored at -80 ℃.

It is worth noting that, for ataxin-3, it is of the most importance to perform all the purification steps at 4 ℃ or on ice.

3.2.5 SDS-PAGE Analysis

Samples were collected throughout the protein expression and purification protocols in order to evaluate the levels of expression and, ultimately, determine the purity of the purified protein. For that, protein samples were resolved by SDS-PAGE, which a denaturing technique

that allows for the separation of proteins based on their molecular weight. As the molecular weight of all purified proteins was comprised between 20 – 80 kDa, 12.5 % acrylamide resolving gels were prepared (see Table 8).

Table 8 Composition of the resolving and stacking gels for the SDS-PAGE analysis.

Resolving Gel (12.5 % Acrylamide)		**Stacking Gel (4 % Acrylamide)**	
Tris-HCl, pH 8.8	500 mM	**Tris-HCl, pH 6.5**	150 mM
Acrylamide	12.5 % (w/v)	**Acrylamide**	4 % (w/v)
SDS	0.2 % (w/v)	**SDS**	0.2 % (w/v)
APS	0.1 % (w/v)	**APS**	0.1 % (w/v)
TEMED	0.001 % (v/v)	**TEMED**	0.001 % (v/v)

In the case of the gels used to study protein expression, a 2 mL sample was collected before (T_{0h}) and 3 hours after the expression was induced (T_{3h}). The cell pellet was harvested by centrifugation for 10 minutes at 4 ℃ and 11000 rpm and resuspended in 500 μL of storage buffer. In a new 1.5 mL microcentrifuge tube, 35 μL of the resuspension, 10 μL of 5× loading buffer [200 mM Tris-HCl, pH 6.8, 20% (v/v) Glycerol, 10% (v/v) SDS, 50 μg/mL Bromophenol Blue], and 5 μL of 1 M DTT were mixed, and the protein sample was denatured at 100 ℃ for 10 minutes to achieve protein denaturation. Afterwards, 10 μL of each sample were loaded to each well of the gel.

For the gels used to study protein purification, 10 μL samples were collected in the different steps of the protocol and mixed with 3 μL of 5× loading buffer, and 2 μL of 1 mM DTT. The samples were denatured at 100 ℃ for 10 minutes to achieve protein denaturation and 10 μL of each sample were loaded to each well of the gel.

The gels were assembled into a Mini-PROTEAN® Tetra Cell system (Bio-Rad) and running buffer [25 mM Tris-HCl, pH 8.3, 192 mM Glycine, 0.1 % (w/v) SDS] was added to both of its chambers. The current was set to constant 30 mA per gel placed in the system. The run was stopped once the loading die reached the end of the resolving gel. The gels were stained with Bio-Safe™ Coomassie (Bio-Rad).

3.2.6 Turbidimetry Assays

For turbidity measurements, the samples were prepared following the procedure shown in Figure 9, adapted from [1]. Shortly, a protein solution was prepared with double the protein

concentration of the final mixture. A PEG 10000 solution was also prepared with double the crowding agent concentration of the final mixture, from a 50 % (w/v) PEG 10000 stock solution (prepared in 50 mM PO_4^{2-} buffer). The solutions were mixed at a 1:1 volume ratio. As an example, to obtain a solution with 100 µM ataxin-3 13Q and 15 % (w/v) PEG, equal amounts of a 200 µM ataxin-3 13Q solution and a 30 % (w/v) PEG solution were mixed. To evaluate the effect of NaCl concentration on ataxin-3 liquid-liquid phase separation (LLPS), the solution was prepared with 100 mM NaCl, and the PEG solution contained the amount of NaCl necessary to obtain the desired final concentration. For example, for a final solution of 100 µM ataxin-3 13Q, 15 % (w/v) PEG and 150 mM NaCl, equal amounts of a 200 µM ataxin-3 13Q, 100 mM NaCl and a 30 % (w/v) PEG, 200 mM NaCl solution were mixed. All the sample conditions evaluated by turbidimetry are fully described in Tables 9-14.

For the assays in which the effects of two distinct buffers were compared (i.e., PO_4^{2-} buffer versus HEPES buffer), the turbidity measurements were preceded by a buffer exchange. For this, the protein was diluted to a final concentration of 200 µM and, using an Amicon Ultra-15 (Millipore Corporation) concentrator, the sample was washed four times with 3 mL of the desired buffer. Finally, the protein solution was concentrated to a final concentration of 200 µM.

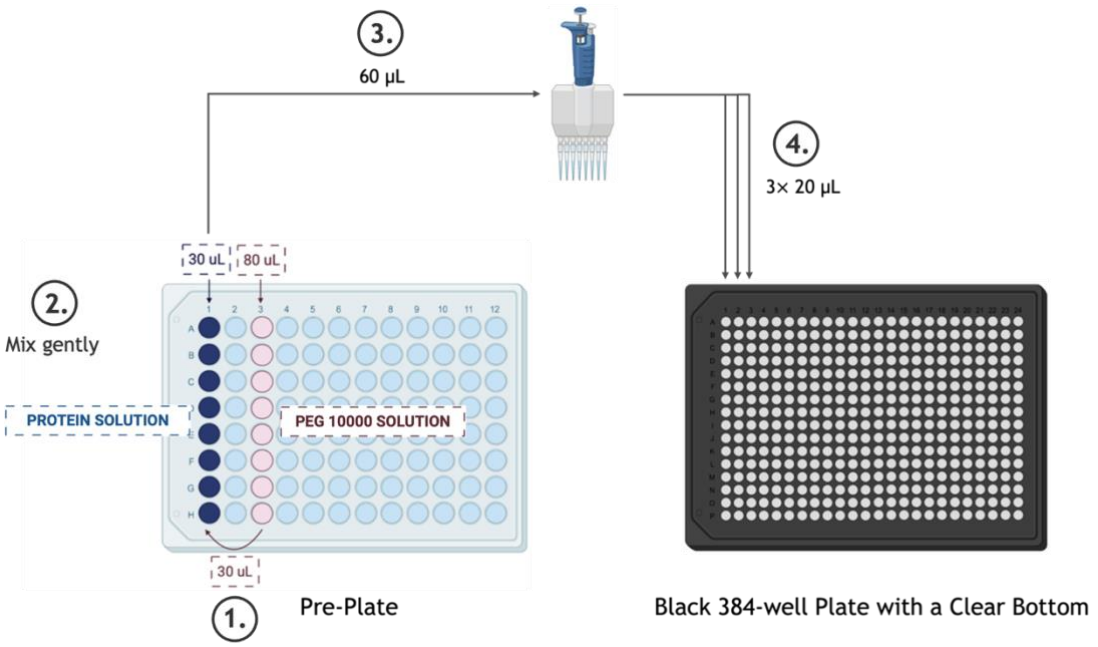


Figure 9 Schematic representation of the sample preparation protocol for the turbidimetry assays. *Created with BioRender.com.*

Table 9 Sample preparation for the turbidimetry assay (PEG concentration test).

	Protein Solution				PEG Solution		
Test Condition % (w/v) PEG	**Ataxin-3 13Q**	**GFP-Ataxin-3 13Q**	**PO_4^{2-} Buffer**	**NaCl**	**PEG 10000**	**PO_4^{2-} Buffer**	**NaCl**
0 %	200 µM	4 µM	50 mM	100 mM	**0 %**	50 mM	200 mM
5 %	200 µM	4 µM	50 mM	100 mM	**10 %**	50 mM	200 mM
10 %	200 µM	4 µM	50 mM	100 mM	**20 %**	50 mM	200 mM
15 %	200 µM	4 µM	50 mM	100 mM	**30 %**	50 mM	200 mM
20 %	200 µM	4 µM	50 mM	100 mM	**40 %**	50 mM	200 mM

Table 10 Sample preparation for the turbidimetry assay (GFP-ataxin-3 13Q concentration test).

	Protein Solution				PEG Solution		
Test Condition GFP-Ataxin-3 13Q :Ataxin-3 13Q	**Ataxin-3 13Q**	**GFP-Ataxin-3 13Q**	**PO_4^{2-} Buffer**	**NaCl**	**PEG 10000**	**PO_4^{2-} Buffer**	**NaCl**
0	200 µM	**0 µM**	50 mM	100 mM	30 %	50 mM	200 mM
1:1000	200 µM	**0.2 µM**	50 mM	100 mM	30 %	50 mM	200 mM
1:100	200 µM	**2 µM**	50 mM	100 mM	30 %	50 mM	200 mM
1:50	200 µM	**4 µM**	50 mM	100 mM	30 %	50 mM	200 mM
1:20	200 µM	**10 µM**	50 mM	100 mM	30 %	50 mM	200 mM

Table 11 Sample preparation for the turbidimetry assay (ataxin-3 concentration test).

	Protein Solution				PEG Solution		
Test Condition µM Ataxin-3	**Ataxin-3 13Q**	**GFP-Ataxin-3 13Q**	**PO_4^{2-} Buffer**	**NaCl**	**PEG 10000**	**PO_4^{2-} Buffer**	**NaCl**
0	**0 µM**	10 µM	50 mM	100 mM	30 %	50 mM	200 mM
12.5	**25 µM**	10 µM	50 mM	100 mM	30 %	50 mM	200 mM
25	**50 µM**	10 µM	50 mM	100 mM	30 %	50 mM	200 mM
50	**100 µM**	10 µM	50 mM	100 mM	30 %	50 mM	200 mM
100	**200 µM**	10 µM	50 mM	100 mM	30 %	50 mM	200 mM

Table 12 Sample preparation for the turbidimetry assay (NaCl concentration test).

	Protein Solution				PEG Solution		
Test Condition mM NaCl	**Ataxin-3 13Q**	**GFP-Ataxin-3 13Q**	**PO_4^{2-} Buffer**	**NaCl**	**PEG 10000**	**PO_4^{2-} Buffer**	**NaCl**
50	200 µM	4 µM	50 mM	**100 mM**	30 %	50 mM	**0 mM**
100	200 µM	4 µM	50 mM	**100 mM**	30 %	50 mM	**100 mM**
150	200 µM	4 µM	50 mM	**100 mM**	30 %	50 mM	**200 mM**
200	200 µM	4 µM	50 mM	**100 mM**	30 %	50 mM	**300 mM**
400	200 µM	4 µM	50 mM	**100 mM**	30 %	50 mM	**700 mM**

Table 13 Sample preparation for the turbidimetry assay (buffer type test).

	Protein Solution				PEG Solution		
Test Condition (PO_4^{2-} Buffer)	**Ataxin-3 13Q**	**GFP-Ataxin-3 13Q**	**PO_4^{2-} Buffer**	**NaCl**	**PEG 10000**	**PO_4^{2-} Buffer**	**NaCl**
0 µM Ataxin-3 13Q	**0 µM**	4 µM	**50 mM**	100 mM	30 %	50 mM	200 mM
12.5 µM Ataxin-3 13Q	**25 µM**	4 µM	**50 mM**	100 mM	30 %	50 mM	200 mM
25 µM Ataxin-3 13Q	**50 µM**	4 µM	**50 mM**	100 mM	30 %	50 mM	200 mM
50 µM Ataxin-3 13Q	**100 µM**	4 µM	**50 mM**	100 mM	30 %	50 mM	200 mM
100 µM Ataxin-3 13Q	**200 µM**	4 µM	**50 mM**	100 mM	30 %	50 mM	200 mM
Test Condition (HEPES Buffer)	**Ataxin-3 13Q**	**GFP-Ataxin-3 13Q**	**HEPES Buffer**	**NaCl**	**PEG 10000**	**$HEPES^-$ Buffer**	**NaCl**
0 µM Ataxin-3 13Q	**0 µM**	4 µM	**50 mM**	100 mM	30 %	50 mM	200 mM
12.5 µM Ataxin-3 13Q	**25 µM**	4 µM	**50 mM**	100 mM	30 %	50 mM	200 mM
25 µM Ataxin-3 13Q	**50 µM**	4 µM	**50 mM**	100 mM	30 %	50 mM	200 mM
50 µM Ataxin-3 13Q	**100 µM**	4 µM	**50 mM**	100 mM	30 %	50 mM	200 mM
100 µM Ataxin-3 13Q	**200 µM**	4 µM	**50 mM**	100 mM	30 %	50 mM	200 mM

Table 14 Sample preparation for the turbidimetry assay (ataxin-3 D1 construct test).

	Protein Solution			PEG Solution		
Test Condition	**Ataxin-3 D1**	**PO_4^{2-} Buffer**	**NaCl**	**PEG 10000**	**PO_4^{2-} Buffer**	**NaCl**
0 µM Ataxin-3 D1 + 150 mM NaCl	**0 µM**	50 mM	**100 mM**	30 %	50 mM	**200 mM**
12.5 µM Ataxin-3 D1 + 150 mM NaCl	**25 µM**	50 mM	**100 mM**	30 %	50 mM	**200 mM**
25 µM Ataxin-3 D1 + 150 mM NaCl	**50 µM**	50 mM	**100 mM**	30 %	50 mM	**200 mM**
50 µM Ataxin-3 D1 + 150 mM NaCl	**100 µM**	50 mM	**100 mM**	30 %	50 mM	**200 mM**
100 µM Ataxin-3 D1 + 150 mM NaCl	**200 µM**	50 mM	**100 mM**	30 %	50 mM	**200 mM**
0 µM Ataxin-3 D1 + 400 mM NaCl	**0 µM**	50 mM	**100 mM**	30 %	50 mM	**700 mM**
12.5 µM Ataxin-3 D1 + 400 mM NaCl	**25 µM**	50 mM	**100 mM**	30 %	50 mM	**700 mM**
25 µM Ataxin-3 D1 + 400 mM NaCl	**50 µM**	50 mM	**100 mM**	30 %	50 mM	**700 mM**
50 µM Ataxin-3 D1 + 400 mM NaCl	**100 µM**	50 mM	**100 mM**	30 %	50 mM	**700 mM**
100 µM Ataxin-3 D1 + 400 mM NaCl	**200 µM**	50 mM	**100 mM**	30 %	50 mM	**700 mM**

After mixing the protein and PEG solutions at a 1:1 volume ratio, 20 µL of each mixture was transferred to a well of a black 384-well plate with a clear bottom (CellCarrier Ultra 384-well, Black, Optically Clear Flat-Bottom Microplate, PerkinElmer®). The Synergy2 (BioTek Instruments) equipment was used to measure the absorbance of the solution at 340 nm, 405 nm, and 600 nm for 5 minutes at 25 ℃ with constant slow shacking between measurements.

Each experiment was performed in triplicate and the mean ± standard deviation was calculated.

3.2.7 Fluorescence and Brightfield Microscopy

The sample preparation protocol presented in the previous section was also implemented for the microscopy analysis (see Section 3.2.6. and Figure 9 and 10). Furthermore, the samples described above for the turbidimetry assays (see Tables 9 – 14) were also evaluated by microscopy. In this way, the quantitative results that were obtained by measuring the turbidity of the samples were complemented with imaging analysis of the particles in solution (i.e., liquid droplets or, in some cases, amorphous aggregates) that are responsible for dispersing the radiation. In addition, two more sets of experiments were conducted only for the microscopy assays to evaluate: i) how the NaCl concentration influences the LLPS saturation concentration of ataxin-3 and, ii) if a variation in NaCl concentration is sufficient to induce ataxin-3 LLPS without the presence of a crowding agent (i.e., PEG) (Tables 15 and 16, respectively).

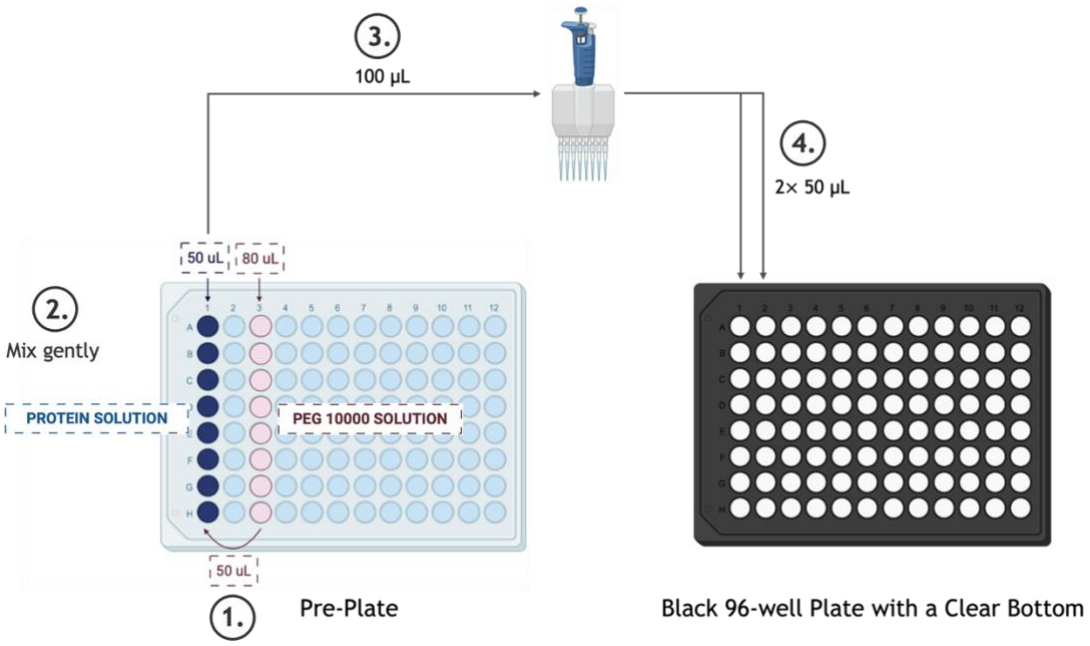


Figure 10 Schematic representation of the protocol used for the sample preparation for the microscopy imaging. *Created with BioRender.com.*

Table 15 Sample preparation for the microscopy imaging (ataxin-3 13Q and NaCl concentration test).

	Protein Solution				PEG Solution		
Test Condition	**Ataxin-3 13Q**	**GFP-Ataxin-3 13Q**	**PO_4^{2-} Buffer**	**NaCl**	**PEG 10000**	**PO_4^{2-} Buffer**	**NaCl**
0 µM Ataxin-3 13Q + 50 mM NaCl	**0 µM**	4 µM	50 mM	**100 mM**	30 %	50 mM	**0 mM**
12.5 µM Ataxin-3 13Q + 50 mM NaCl	**25 µM**	4 µM	50 mM	**100 mM**	30 %	50 mM	**0 mM**
25 µM Ataxin-3 13Q + 50 mM NaCl	**50 µM**	4 µM	50 mM	**100 mM**	30 %	50 mM	**0 mM**
50 µM Ataxin-3 13Q + 50 mM NaCl	**100 µM**	4 µM	50 mM	**100 mM**	30 %	50 mM	**0 mM**
100 µM Ataxin-3 13Q + 50 mM NaCl	**200 µM**	4 µM	50 mM	**100 mM**	30 %	50 mM	**0 mM**
0 µM Ataxin-3 13Q + 100 mM NaCl	**0 µM**	4 µM	50 mM	**100 mM**	30 %	50 mM	**100 mM**
12.5 µM Ataxin-3 13Q + 100 mM NaCl	**25 µM**	4 µM	50 mM	**100 mM**	30 %	50 mM	**100 mM**
25 µM Ataxin-3 13Q + 100 mM NaCl	**50 µM**	4 µM	50 mM	**100 mM**	30 %	50 mM	**100 mM**
50 µM Ataxin-3 13Q + 100 mM NaCl	**100 µM**	4 µM	50 mM	**100 mM**	30 %	50 mM	**100 mM**
100 µM Ataxin-3 13Q + 100 mM NaCl	**200 µM**	4 µM	50 mM	**100 mM**	30 %	50 mM	**100 mM**
0 µM Ataxin-3 13Q + 150 mM NaCl	**0 µM**	4 µM	50 mM	**100 mM**	30 %	50 mM	**200 mM**

12.5 µM Ataxin-3 13Q + 150 mM NaCl	**25 µM**	4 µM	50 mM	**100 mM**	30 %	50 mM	**200 mM**
25 µM Ataxin-3 13Q + 150 mM NaCl	**50 µM**	4 µM	50 mM	**100 mM**	30 %	50 mM	**200 mM**
50 µM Ataxin-3 13Q + 150 mM NaCl	**100 µM**	4 µM	50 mM	**100 mM**	30 %	50 mM	**200 mM**
100 µM Ataxin-3 13Q + 150 mM NaCl	**200 µM**	4 µM	50 mM	**100 mM**	30 %	50 mM	**200 mM**
0 µM Ataxin-3 13Q + 200 mM NaCl	**0 µM**	4 µM	50 mM	**100 mM**	30 %	50 mM	**300 mM**
12.5 µM Ataxin-3 13Q + 200 mM NaCl	**25 µM**	4 µM	50 mM	**100 mM**	30 %	50 mM	**300 mM**
25 µM Ataxin-3 13Q + 200 mM NaCl	**50 µM**	4 µM	50 mM	**100 mM**	30 %	50 mM	**300 mM**
50 µM Ataxin-3 13Q + 200 mM NaCl	**100 µM**	4 µM	50 mM	**100 mM**	30 %	50 mM	**300 mM**
100 µM Ataxin-3 13Q + 200 mM NaCl	**200 µM**	4 µM	50 mM	**100 mM**	30 %	50 mM	**300 mM**
0 µM Ataxin-3 13Q + 400 mM NaCl	**0 µM**	4 µM	50 mM	**100 mM**	30 %	50 mM	**700 mM**
12.5 µM Ataxin-3 13Q + 400 mM NaCl	**25 µM**	4 µM	50 mM	**100 mM**	30 %	50 mM	**700 mM**
25 µM Ataxin-3 13Q + 400 mM NaCl	**50 µM**	4 µM	50 mM	**100 mM**	30 %	50 mM	**700 mM**
50 µM Ataxin-3 13Q + 400 mM NaCl	**100 µM**	4 µM	50 mM	**100 mM**	30 %	50 mM	**700 mM**
100 µM Ataxin-3 13Q + 400 mM NaCl	**200 µM**	4 µM	50 mM	**100 mM**	30 %	50 mM	**700 mM**

Table 16 Sample preparation for the microscopy imaging (PEG and NaCl concentration test).

	Protein Solution				PEG Solution		
Test Condition	**Ataxin-3 13Q**	**GFP-Ataxin-3 13Q**	**PO_4^{2-} Buffer**	**NaCl**	**PEG 10000**	**PO_4^{2-} Buffer**	**NaCl**
0 % PEG + 50 mM NaCl	200 µM	4 µM	50 mM	**100 mM**	**0 %**	50 mM	**0 mM**
5 % PEG + 50 mM NaCl	200 µM	4 µM	50 mM	**100 mM**	**10 %**	50 mM	**0 mM**
10 % PEG + 50 mM NaCl	200 µM	4 µM	50 mM	**100 mM**	**20 %**	50 mM	**0 mM**
15 % PEG + 50 mM NaCl	200 µM	4 µM	50 mM	**100 mM**	**30 %**	50 mM	**0 mM**
20 % PEG + 50 mM NaCl	200 µM	4 µM	50 mM	**100 mM**	**40 %**	50 mM	**0 mM**
0 % PEG + 100 mM NaCl	200 µM	4 µM	50 mM	**100 mM**	**0 %**	50 mM	**100 mM**
5 % PEG + 100 mM NaCl	200 µM	4 µM	50 mM	**100 mM**	**10 %**	50 mM	**100 mM**
10 % PEG + 100 mM NaCl	200 µM	4 µM	50 mM	**100 mM**	**20 %**	50 mM	**100 mM**
15 % PEG + 100 mM NaCl	200 µM	4 µM	50 mM	**100 mM**	**30 %**	50 mM	**100 mM**
20 % PEG + 100 mM NaCl	200 µM	4 µM	50 mM	**100 mM**	**40 %**	50 mM	**100 mM**
0 % PEG + 150 mM NaCl	200 µM	4 µM	50 mM	**100 mM**	**0 %**	50 mM	**200 mM**
5 % PEG + 150 mM NaCl	200 µM	4 µM	50 mM	**100 mM**	**10 %**	50 mM	**200 mM**

10 % PEG + 150 mM NaCl	200 µM	4 µM	50 mM	**100 mM**	**20 %**	50 mM	**200 mM**
15 % PEG + 150 mM NaCl	200 µM	4 µM	50 mM	**100 mM**	**30 %**	50 mM	**200 mM**
20 % PEG + 150 mM NaCl	200 µM	4 µM	50 mM	**100 mM**	**40 %**	50 mM	**200 mM**
0 % PEG + 200 mM NaCl	200 µM	4 µM	50 mM	**100 mM**	**0 %**	50 mM	**300 mM**
5 % PEG + 200 mM NaCl	200 µM	4 µM	50 mM	**100 mM**	**10 %**	50 mM	**300 mM**
10 % PEG + 200 mM NaCl	200 µM	4 µM	50 mM	**100 mM**	**20 %**	50 mM	**300 mM**
15 % PEG + 200 mM NaCl	200 µM	4 µM	50 mM	**100 mM**	**30 %**	50 mM	**300 mM**
20 % PEG + 200 mM NaCl	200 µM	4 µM	50 mM	**100 mM**	**40 %**	50 mM	**300 mM**
0 % PEG + 400 mM NaCl	0 µM	4 µM	50 mM	**100 mM**	**30 %**	50 mM	**700 mM**
5 % PEG + 400 mM NaCl	25 µM	4 µM	50 mM	**100 mM**	**30 %**	50 mM	**700 mM**
10 % PEG + 400 mM NaCl	50 µM	4 µM	50 mM	**100 mM**	**30 %**	50 mM	**700 mM**
15 % PEG + 400 mM NaCl	100 µM	4 µM	50 mM	**100 mM**	**30 %**	50 mM	**700 mM**
20% PEG + 400 mM NaCl	200 µM	4 µM	50 mM	**100 mM**	**30 %**	50 mM	**700 mM**

After the protein and PEG solutions were mixed at a 1:1 volume ratio, 50 µL of each mixture was transferred to a well of a black 96-well plate with a clear bottom (96-well Half Area High Content Imaging Film Bottom Microplate, Corning®). The IN Cell Analyzer 2000 (GE Healthcare) equipment was used to acquire sample images at room temperature with a Nikon 40×/0.95, Plan Apo, Corr/Collar 0.11-0.23, CFI/60 Lambda objective. Two distinct acquisition

modes were selected to obtain the images: (i) fluorescence microscopy and (ii) brightfield microscopy (with the exception of the ataxin-3 D1 construct test, for which only brightfield microscopy was used, as no fluorescent protein was added to the sample). The channel settings for each acquisition mode are shown in Table 17. In fluorescence microscopy, images from three selected fields were acquired through three focal planes (with a 2.5 µm step). For DIC images, only one focal plane was selected for each field. Images were captured every 5-6 minutes for 30-42 minutes. Each experiment was performed in duplicate.

Table 17 Channel settings used in the microscopy analysis with the IN Cell Analyzer imaging system.

Channel	Excitation	Emission	Exposure	Image Type	Parameters
FITC	FITC	FITC	1.500	3-D	Slices: 3; Step: 2.50
Brightfield	Brightfield	DAPI	0.050	DIC	No Z Slices

3.2.8 Fluorescence Recovery After Photobleaching Assays

FRAP experiments were conducted to characterize the material properties of ataxin-3 13Q droplets. In addition, the effect of the ionic strength on the fluidity of the condensates was also evaluated, through the variation of salt concentration (see Table 18). To prepare the samples, 5 µL of the protein solution were added to 5 µL of the PEG solution in a 1.5 mL low protein binding microcentrifuge tube (Eppendorf). Following gentle homogenization of the sample, 5 µL from the mixture were spotted onto a glass microscope slide (VWR®) and covered with a glass coverslip (Labbox).

Table 18 Sample preparation for the FRAP assay (NaCl concentration test).

	Protein Solution				PEG 10000 Solution		
Test Condition	**Ataxin-3 13Q**	**GFP-Ataxin-3 13Q**	**PO_4^{2-} Buffer**	**NaCl**	**PEG 10000**	**PO_4^{2-} Buffer**	**NaCl**
150 mM NaCl	200 μM	10 μM	50 mM	**100 mM**	30 %	50 mM	**200 mM**
400 mM NaCl	200 μM	10 μM	50 mM	**100 mM**	30 %	50 mM	**700 mM**

FRAP assays were performed on a Leica TCS SP5II (Leica Microsystems) confocal microscope at room temperature. Furthermore, an HCX Plan-Apochromat CS 63x glycerol-immersion (NA 1.3) objective (Leica Microsystems) was used. Between assays, the pixel resolution (512 × 512), the pinhole (1 μm), and the gain (800 V) were kept constant. Excitation of the fluorescent molecules was accomplished with an Argon 488 nm laser beam at 10 % intensity, while the resulting emission signal was detected at a range of wavelength between 500 – 570 nm. The same excitation laser beam at 100 % laser transmission was used to bleach a circular region of the GFP-ataxin-3 13Q-containing droplets, using the Zoom-In method. One FRAP assay consisted of 3 distinct steps: i) pre-bleaching (3 images); ii) bleaching (5 images); iii) post-bleaching (90 images). Images were captured every 1.3 s. All measurements were performed in the first 30 minutes after sample preparation. This was done to exclude any effect due to the aging of the droplets. The raw data were analyzed with Fiji software and the recovery of the florescence intensity for each experiment was determined. Both the mobile fraction and the diffusion coefficient were calculated for the result section and presented as mean ± standard deviation. The diffusion coefficient was calculated following

$$D = \frac{w^2}{4t_{1/2}} \times 0.88 \quad (1)$$

where w is the radius of the bleached area and $t_{1/2}$ is the halftime for recovery, which can be calculated as

$$t_{1/2} = \frac{\ln 0.5}{-\tau} \quad (2)$$

in which τ is a parameter obtained from the fitting of the fluorescence intensity recovery curve

$$y(t) = A \times (1 - e^{-\tau \times t}) \quad (3)$$

A represents the mobile fraction and corresponds to the value at which the recovery curves tend to stabilize with time.

Chapter 4

Results and Discussion

4.1 Expression and Purification of the Ataxin-3 Constructs

Each ataxin-3 construct (i.e., ataxin-3 D1, ataxin-3 13Q, or GFP-ataxin-3 13Q) was successfully overexpressed in BL21(DE3)-SI cells, as shown (Figures 11A and 12A). At 3 hours after protein expression induction (T_{3h} in Figures 11A and 12A) there was a band corresponding to the protein of interest, which was not observed before the expression was induced (T_{0h} in Figures 11A and 12A).

After cell lysis, the protein was purified from the supernatant in two chromatography steps: first an ion immobilized affinity chromatography (IMAC), followed by a preparative SEC. For the first IMAC step, the supernatant was loaded to a Ni^{2+}-charged HiTrap™ IMAC HP column. The SDS-PAGE analysis confirmed that the protein of interest was, indeed, loaded to the column, as its protein band was no longer visible in the flow-through fraction (see Figures 11B, 12B and 13A). Due to the 6×His tag present at their N terminus, the ataxin-3 constructs possess a high affinity for the Ni^{2+} ions. Consequently, the protein of interest is expected to elute from the column in the presence of higher concentrations of imidazole (i.e., 260 mM, or 50 % Buffer B). This was, in fact, observed for both the ataxin-3 D1 and the ataxin-3 13Q constructs (Figures 11B-C and 12B-C).

For the purification of the GFP-ataxin-3 13Q construct a single elution step was performed with 50 % Buffer B (i.e., 260 mM imidazole) to prevent the loss of the protein at lower imidazole concentrations (Figure 13A-B and Figure 14). We knew that a great amount of this protein eluted from the column even at a lower Imidazole concentration (i.e., 68 mM, or 10 % Buffer B). For this reason, and to optimize the yield of the GFP-ataxin-3 13Q protein purification, the elution step of 10 % Buffer B was excluded (see Figure 13A-B). This alteration to the protein purification protocol may, however, lead to a final sample with a lower degree of purity.

Following this, the ataxin-3-containing sample eluted from the IMAC column was further purified by SEC using a HiPrep™ 26/60 Sephacryl® S300 HR column. In this chromatography method, proteins are separated according to their molecular size: while larger molecules elute at lower volumes, smaller molecules elute after a longer elution period (i.e., at higher elution volumes). Consequently, the smallest ataxin-3 construct (i.e., ataxin-3 D1) eluted at a higher volume than the largest one (i.e., GFP-ataxin-3 13Q). This relationship between protein molecular weight and elution volume is highlighted in Table 19.

As observed in the SEC chromatograms presented in Figures 11D, 12D and 13C, the A_{280nm} peak corresponding to the monomeric form of the protein was normally preceded by a smaller peak (highlighted with an asterisk) of its aggregates with a higher molecular weight that might be formed throughout the expression, lysis, and purification processes.

Table 19 Elution volumes of each ataxin-3 construct in size exclusion chromatography when using the HiPrep™ 26/60 Sephacryl® S300 HR column.

Ataxin-3 Construct	Molecular Weight (Da)	Elution Volume (mL)	Fractions
Ataxin-3 D1	32580.62	190	23 – 26
Ataxin-3 13Q	43582.58	180	19 – 21
GFP-Ataxin-3 13Q	70522.70	160	15 – 21

The purity of the protein samples eluted by SEC was confirmed by SDS-PAGE (12.5 %) analysis (Figures 11B, 12B and 13A). Fractions with the protein of interest in the monomeric form and with a high degree of purity (shown in Table 19) were combined and concentrated to a final concentration of 10–25 mg/mL. The final protein yields are presented in Table 20.

Table 20 Final yields obtained in the purification of each ataxin-3 construct.

Ataxin-3 Construct	Yield (mg of protein/L of cell culture)
Ataxin-3 D1	0.7
Ataxin-3 13Q	2.9
GFP-Ataxin-3 13Q	1.3

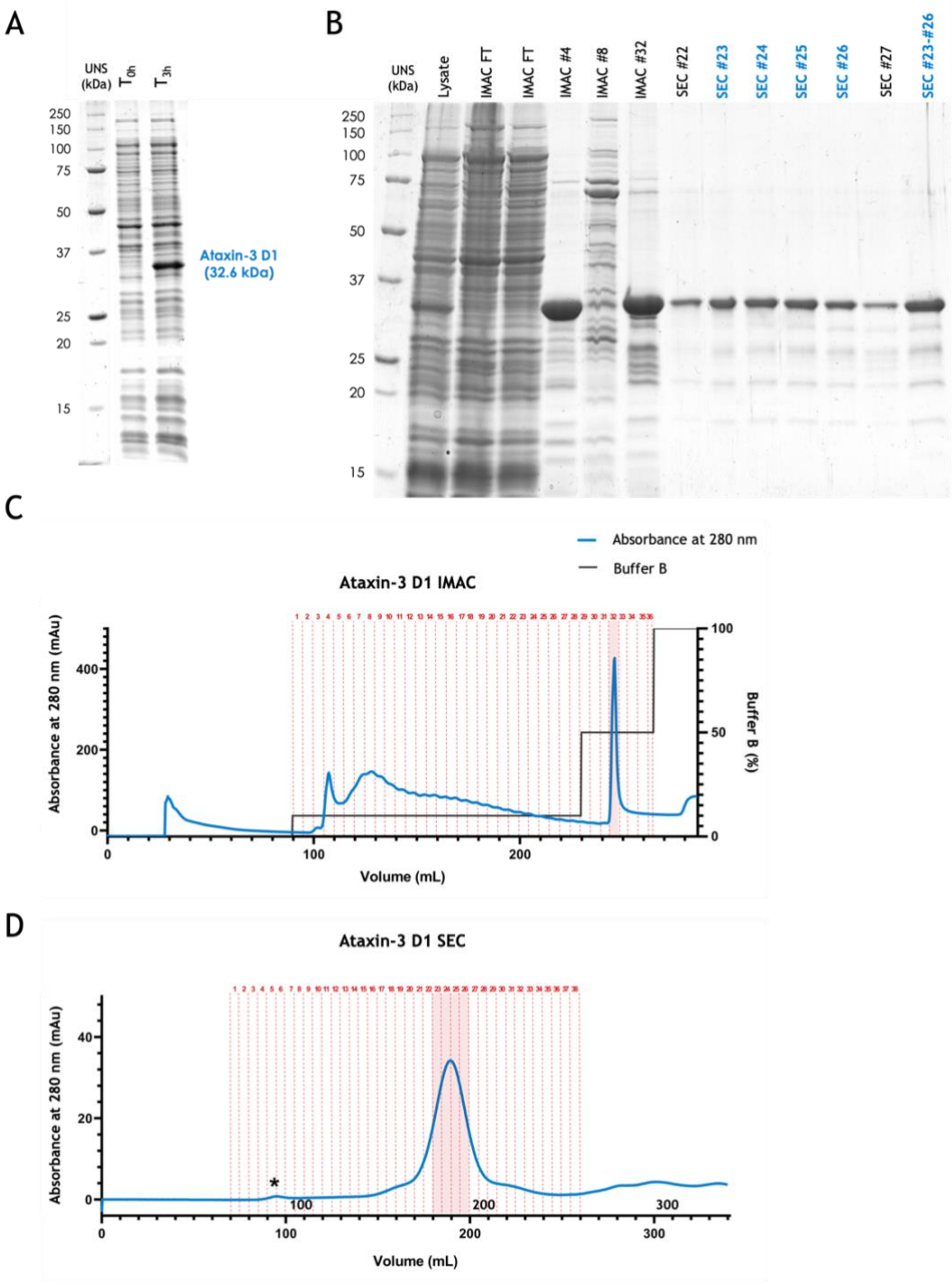


Figure 11 Ataxin-3 D1 expression and purification. SDS-PAGE analysis of ataxin-3 D1 expression **(A)** and purification **(B)**. The fractions pooled together for the final sample after SEC are shown in blue. **C)** IMAC chromatogram of the ataxin-3 D1 purification with two elution steps: first with 68 mM imidazole (10 % Buffer B), followed by 260 mM imidazole (50 % Buffer B). The fraction that was kept for the following SEC step is highlighted in red. **D)** SEC chromatogram of the ataxin-3 D1 purification. The fractions pooled together for the final sample are highlighted in red. The asterisk indicates the small peak of high molecular weight aggregates.

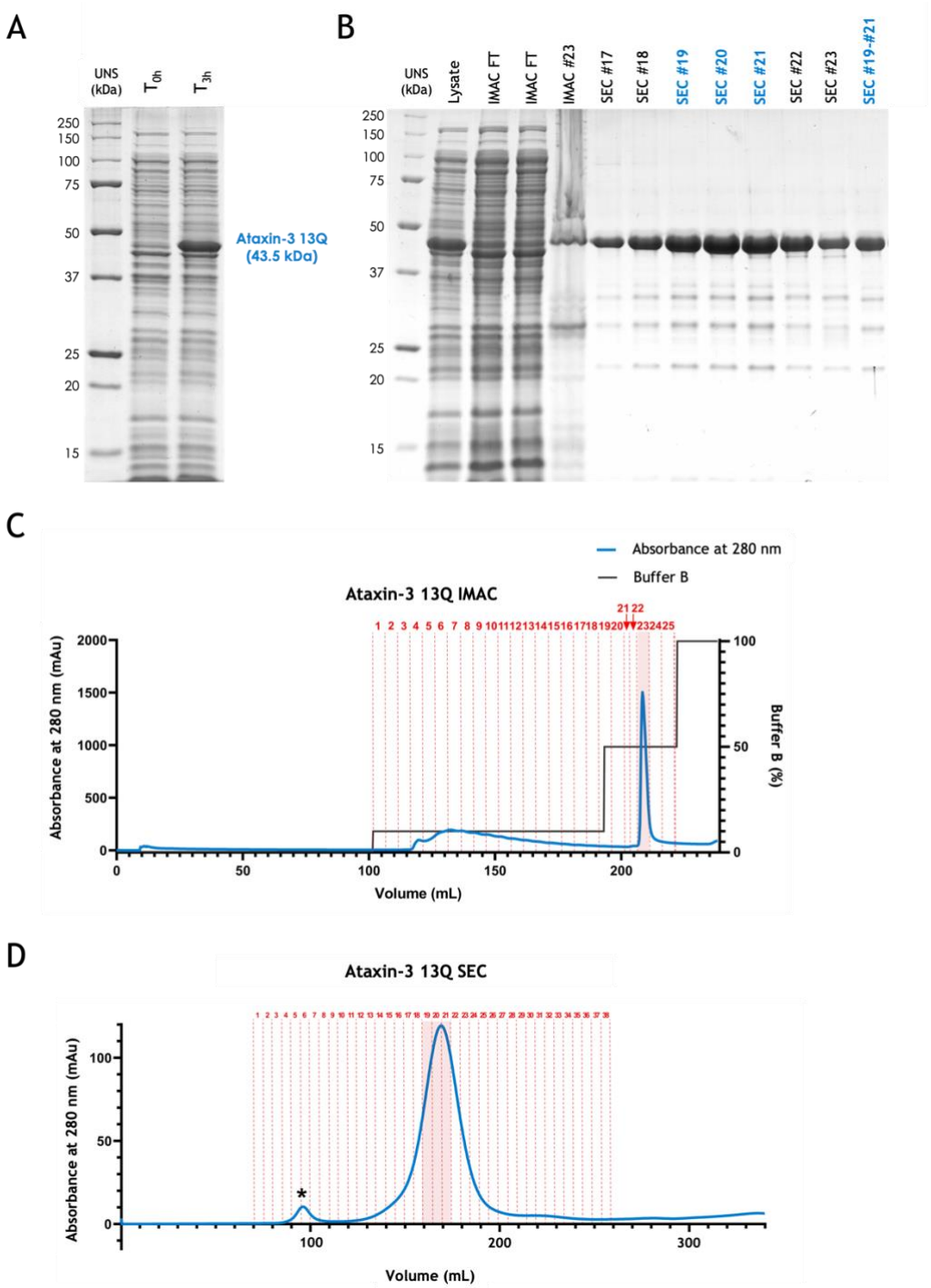


Figure 12 Ataxin-3 13Q expression and purification. SDS-PAGE analysis of ataxin-3 13Q expression **(A)** and purification **(B)**. The fractions pooled together for the final sample after SEC are shown in blue. **C)** IMAC chromatogram of the ataxin-3 13Q purification with two elution steps: first with 68 mM imidazole (10 % Buffer B), followed by 260 mM imidazole (50 % Buffer B). The fraction that was kept for the following SEC step is highlighted in red. **D)** SEC chromatogram of the ataxin-3 13Q purification. The fractions pooled together for the final sample are highlighted in red. The black asterisk indicates the small peak of high molecular weight aggregates.

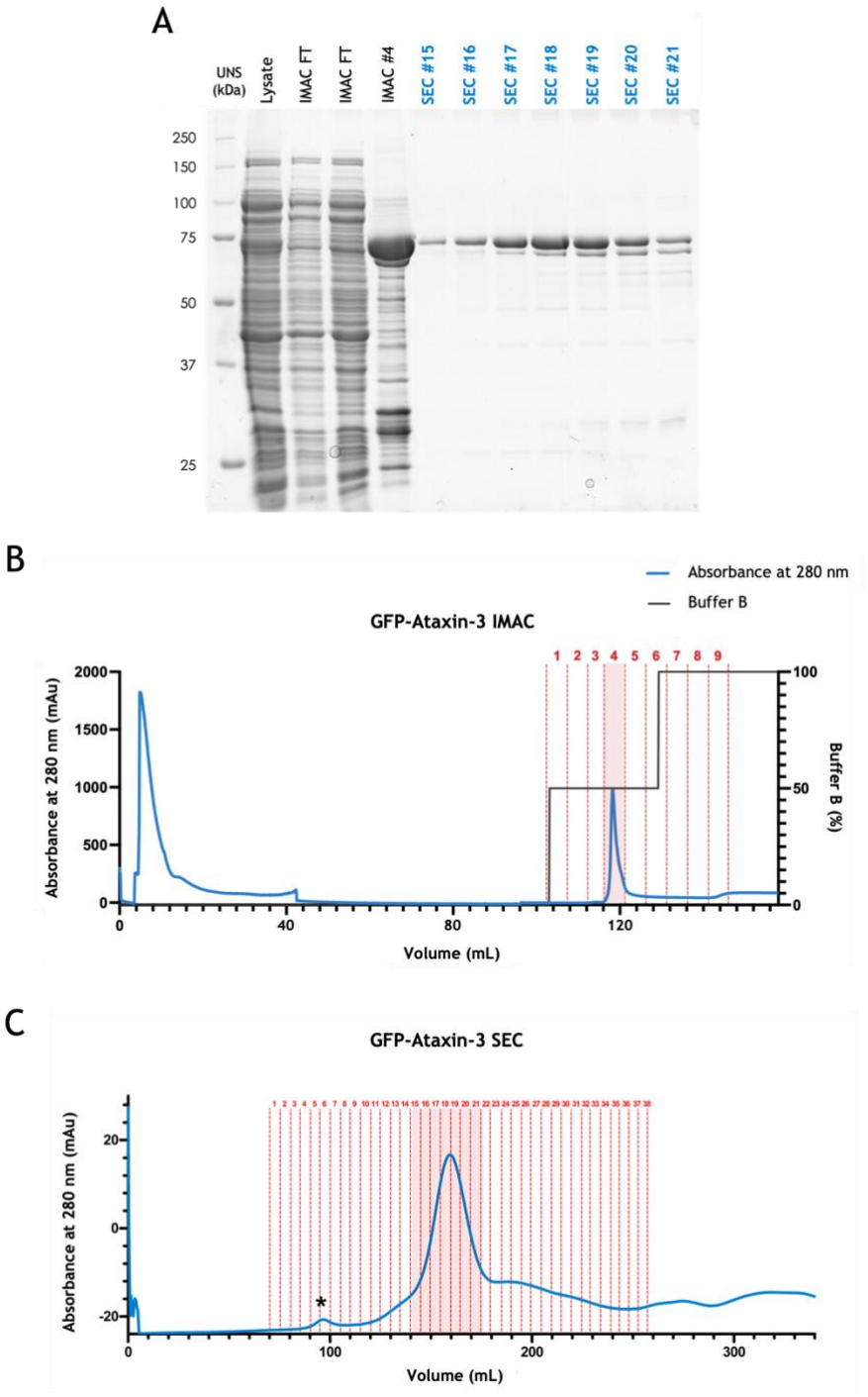


Figure 13 GFP-ataxin-3 13Q expression and purification. SDS-PAGE analysis of GFP-ataxin-3 13Q purification **(A)**. The fractions pooled together for the final sample after SEC are shown in blue. **B)** IMAC chromatogram of the GFP-ataxin-3 13Q purification with one single elution step with 68 mM imidazole (10 % Buffer B). The fraction that was kept for the following SEC step is highlighted in red. **C)** SEC chromatogram of the GFP-ataxin-3 13Q purification. The fractions pooled together for the final sample are highlighted in red. The black asterisk indicates the small peak of high molecular weight aggregates.

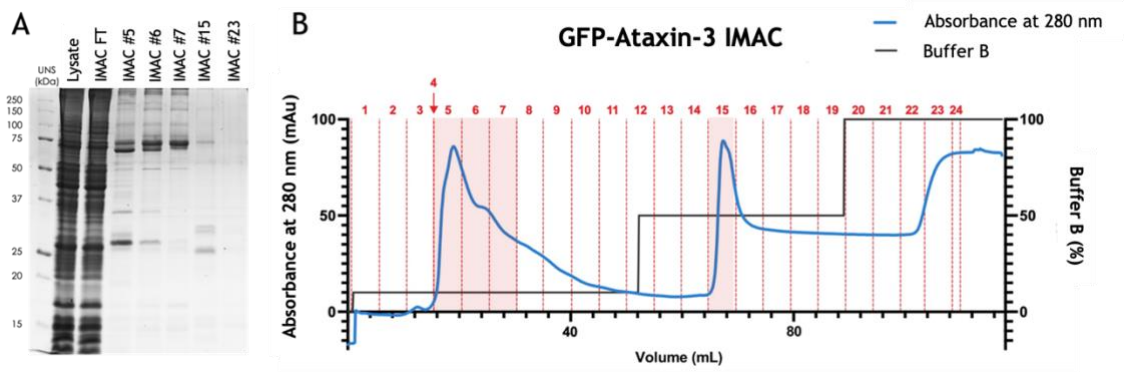


Figure 14 GFP-ataxin-3 13Q purification by a two-step elution in the IMAC chromatography column. A) SDS-PAGE analysis of ataxin-3 13Q IMAC purification. **B)** IMAC chromatogram of the GFP-ataxin-3 13Q purification with two elution steps: first with 68 mM imidazole (10 % Buffer B), followed by 260 mM imidazole (50 % Buffer B). The fractions that were used for the following SEC step are highlighted in red.

The yield of the ataxin-3 D1 construct was low (shown in Table 20), especially when comparing to previous purifications performed in our group, where it was possible to obtain around 3 milligrams of protein per litre of cell culture. As shown above in Section 3.1.4, the ataxin-3 D1 construct is only composed of the globular JD and the first two UIMs of ataxin-3. In fact, this construct excludes the polyQ region that potentiates aggregation. For this reason, this construct is generally more stable during the expression and purification processes. The protein expression was successful (Figure 11A), as the band corresponding to ataxin-3 D1 is clearly identified after 3 hours of protein expression. However, the process of cell lysis may have been insufficient, as the ataxin-3 D1 band on the SDS-PAGE gel was rather weak in the lysate (Figure 11B). Therefore, an optimization of the lysis step (e.g., by increasing its duration or by rising the stirring speed) should be further explored to improve the yield of this purification.

4.2 Characterization of Ataxin-3 Liquid-Liquid Phase Separation Behavior in Different Conditions

4.2.1 Sequence Analysis and Prediction of Ataxin-3 Phase-Separation Behavior

Bioinformatic tools are gaining popularity for the identification of proteins with propensity to undergo LLPS. In fact, from the amino acid sequence alone, predictive algorithms like IUPred[183] and PLAAC[184], describe the protein's tendency to adopt a preferential folding state or to remain unfolded in solution. As both multi-domain proteins and IDPs present a high multivalence and can establish weak and transient interactions important for the formation of

phase-separated liquid droplets, the information obtained from these tools can be used to assess the likelihood of a specific protein to have LLPS behavior. Prion-like domain (PLD) structures, which are disordered and have low sequence complexity by nature, are also identified by the PLAAC predictor. Furthermore, this same server shows how some of the molecule's relevant physicochemical properties (e.g., net charge and hydrophobicity) change throughout its sequence. This can be used to uncover the preferential interaction modes (e.g., electrostatic or hydrophobic) that participate in the phase separation process. More recently, the FuzDrop[185] method was developed to predict the probability of proteins to spontaneously undergo LLPS, through the identification of both droplet-promoting regions (DPRs) and aggregation hotspots in the molecule's sequence. DPRs are defined as segments of 10 or more residues with a droplet-promoting probability superior to 60 %[185]. On the other hand, aggregation hotspots are segments comprised in DPRs that can extensively exchange between the ordered and disordered binding modes[185]. The presence of these hotspots is associated with a faster droplet maturation process, which irreversibly changes the material properties of the condensates from liquid to solid-like[185]. Aggregation propensity of proteins can be studied with the Aggrescan software[186]. In Figure 15, we present the results obtained by implementing the three algorithms described above to the sequence of the ataxin-3 13Q construct used throughout this work.

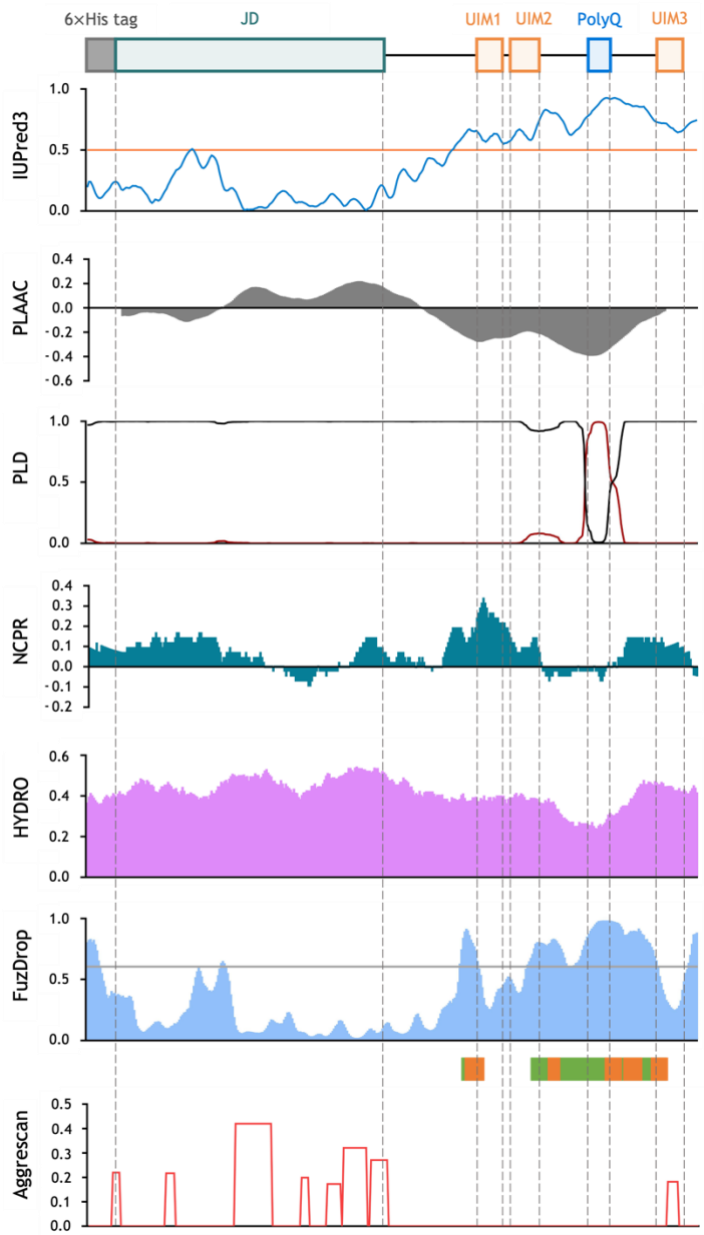


Figure 15 Bioinformatic analysis of the primary structure of ataxin-3 13Q to predict its propensity to undergo phase separation. A schematic representation of the domain structure of ataxin-3 13Q is presented at the top. IUPred3 and PLAAC are predictors of disorder and folding, respectively. The prion-like domain (PLD) graph highlights low complexity regions of the protein (predicted by PLAAC). Net charge per residue (NCPR) and hydrophobicity (HYDRO) of the protein according to the Kyte & Doolitle hydropathy score are shown (predicted by PLAAC). FuzDrop predicts the presence of DPRs and aggregation hotspots (shown in green and orange below the graph, respectively) in the protein's sequence. Aggrescan is an additional tool used to predict the aggregation propensity of a molecule.

In agreement to what is already well established for the three-dimensional structure of ataxin-3, both folding predictions revealed a structured N terminus, containing the JD, connected to a disordered C-terminal region, made up of the three UIMs and the polyQ tract[21]. The PLAAC algorithm also identified a PLD that coincides with the polyQ region of ataxin-3. Charged residues are distributed throughout the protein. Furthermore, the Kyte & Doolitle hydropathy score predicts that the protein is mostly of hydrophobic nature, although no values

superior to 0.6 are observed. The FuzDrop server prediction resulted in a high probability of spontaneous liquid-liquid phase separation (p_{LLPS}=0.8879). In fact, two distinct DPRs were proposed: i) a shorter one (residues 232-243), which precedes the UIM1; and ii) a longer one (residues 274-355), which ranges from the last residues of the UIM2 to the first amino acids of the UIM3, comprising the full polyQ tract. Both DPRs have aggregation hotspots, which suggests that ataxin-3 phase-separated droplets are highly susceptible to maturation. However, the Aggrescan software proposed different aggregation prone regions, seven in the N-terminal portion of the protein (residues 16-20, 49-54, 92-114, 133-137, 149-157, 159-173, and 176-186), and one at its C terminus (residues 360-366). Note that, the aggregation regions identified in the JD by the Aggrescan tool have already been experimentally determined by Scarff et al., 2015.

Taken together, these results indicate that it is very likely that ataxin-3 acts as a driving protein for LLPS. In the following sections, we describe how specific solution conditions (such as biomolecular crowding, protein concentration, ionic strength, and buffer type) influence the phase separation behavior of the studied protein system.

4.2.2 A Crowding Agent is Necessary for Ataxin-3 13Q Liquid-Liquid Phase Separation

The intracellular compartment, where most of the organism's ataxin-3 is found, isn't a homogeneous solution in which molecules can freely diffuse. Instead, the extremely high biomolecular concentration observed inside of a cell (e.g., overall macromolecular concentration of 50-400 mg/mL in eukaryotic cells[4]) creates a crowded environment. In other words, when the cell's molecules occupy a significant portion of the cytoplasm, the volume solvent that is available to interact with them is reduced. This increases their local concentration, with a direct effect on their structure and function[187-190]. Researchers have been using biopolymers [e.g., dextran, Ficoll, and polyethylene glycol (PEG)] of various molecular weights (MW: 60-500,000) to mimic the material properties of the intracellular environment and to evaluate the effects of biomolecular crowding on specific properties of proteins, including: i) thermodynamic stability; ii) structure acquisition; iii) aggregation propensity; and iv) overall function[191]. This application of biopolymers is also being explored to study LLPS *in vitro*, as crowding may be a crucial property of the protoplasm for bringing molecules close to each other at the right concentration for condensation to occur *in vivo*. In fact, although some proteins can undergo LLPS *in vitro* in the absence of a crowding agent (e.g., FUS, EWSR1, and TAF15[125]), many others, such as tau[129], α-synuclein[12,132], and huntingtin exon1[10], only phase separate when a biopolymer is added to the solution.

For ataxin-3, it was reported that a minimum of 10 % (w/v) PEG (MW: 7,400-10,200) or dextran (MW:50,000-70,000 or 180,000-210,000) is necessary for the observation of phase-separated droplets (at protein and salt concentrations of 100 μM and 150 mM, respectively)[1]. However, the FRAP and Raman microscopy assays were all achieved with a crowding agent at concentration of 20 % (w/v). In an attempt to reproduce the previously obtained results with our protein system and to confirm this dependency of a crowded environment for ataxin-3 13Q LLPS to take place, we tested a range of physiologically relevant PEG10000 concentrations[191].

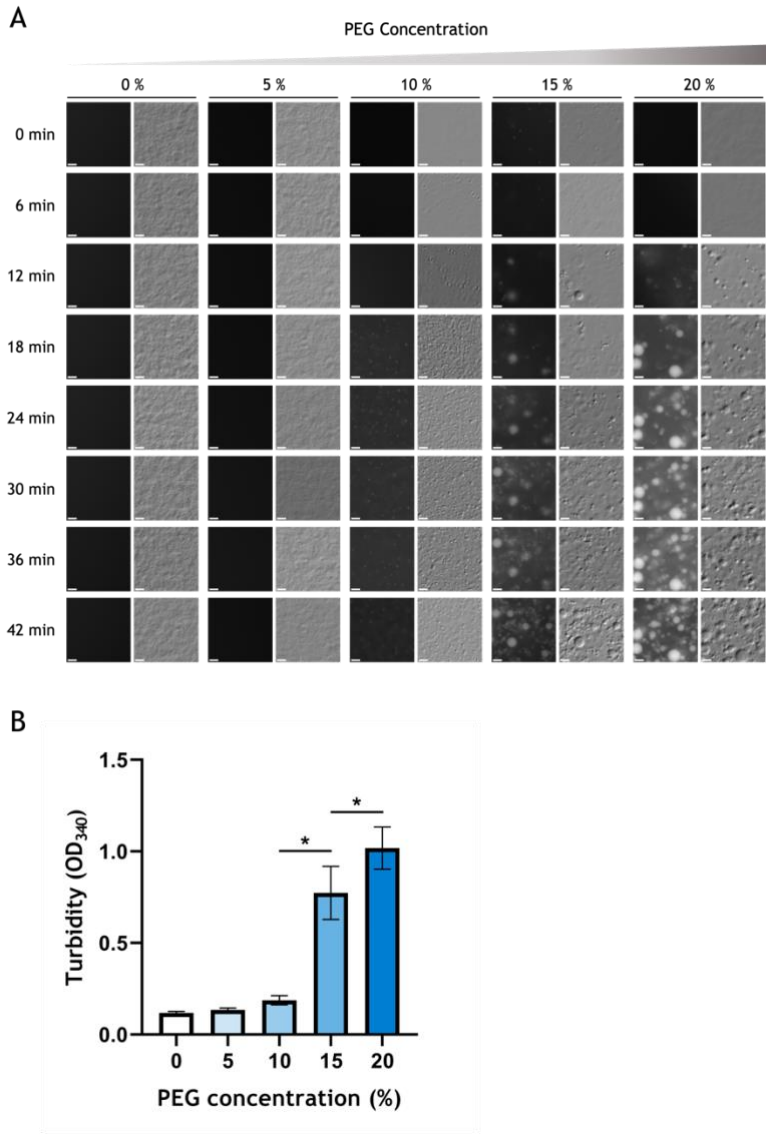


Figure 16 Effect of PEG concentration on LLPS of ataxin-3 13Q. (A) Microscopy images of ataxin-3 13Q droplets in the presence of different PEG 10000 concentrations. Ataxin-3 13Q (100 μM), GFP-ataxin-3 13Q (4 μM), and NaCl (150 mM) concentrations were kept constant. For each one of the evaluated conditions, FITC (on the left) and DIC (on the right) images were acquired every 6 minutes for 42 minutes. The scale bar corresponds to 10 μm. **(B)** Turbidity measurements at 340 nm of the ataxin-3 13Q solutions with varying concentrations of PEG. Experiments were performed in triplicate and the mean value ± standard deviation is presented. Values were compared by One-WAY ANOVA (*p-value ≤ 0.0001).

The fluorescence and brightfield images (Figure 16A) corroborate what was previously described for the effect of a crowding agent on LLPS of ataxin-3. In fact, 10 % (w/v) is the lowest crowding agent concentration at which the presence of a new phase is observed. The formed particles are small in size (~ 2 μm in diameter) and appear to have a spherical geometry. They also concentrate the fluorescently tagged protein (i.e., GFP-ataxin-3 13Q), which was demonstrated by the clear difference in fluorescence intensity between the two phases. Sedimentation assays (see Section 2.5.1.) would further help to elucidate the compositional differences between the two phases. Furthermore, the increase in PEG concentration seems to be accompanied by a visible increase in droplet size. In the future, it would be relevant to perform DLS assays (see Section 2.5.3), as it would allow us to clearly quantify how particle size distribution is affected by the increase in biomolecular crowding. With time, there was a significant increase in droplet number in the presented images. However, no particle growth was observed. For this reason, we propose that, as we are looking at a single focus plane from the sample, the rise in droplet count was due to deposition and did not reflect a continued nucleation process. In Figure 16B we see that sample turbidity was only significantly enhanced in the conditions with the two highest PEG concentrations.

Taking all of the previously described results into consideration, we selected the 15 % (w/v) PEG condition for the following assays, as it was the lowest concentration for which phase separation was detected by both experimental techniques.

4.2.3 Ataxin-3 13Q Liquid-Liquid Phase Separation is not Influenced by the Presence of GFP-Ataxin-3 13Q

To explore if the addition of the GFP-tagged protein somehow influences the phase separation behavior of ataxin-3 microscopy and turbidimetry assays were performed in which the concentration of GFP-ataxin-3 13Q was varied between 0 μM and 10 μM (Figure 17).

As expected, a decrease in the GFP-ataxin-3 13 to ataxin-3 13Q molar ratio resulted in droplets with progressively less fluorescence intensity (Figure 16A). In fact, when the GFP-tagged construct is completely excluded from the sample, the droplets can only be monitored by brightfield microscopy. By analyzing particle size and number, particularly at the last time point where most of the deposition process has already taken place, no relationship can be established between GFP-ataxin-3 13Q concentration and the extent of ataxin-3 13Q LLPS. In addition, the turbidimetry assays (Figure 17B), which take into consideration what is happening throughout the whole sample at a specific moment, reveal that there are no significant differences in sample turbidity between the tested conditions. This has led us to conclude that, in this specific experimental set-up, the fluorescent ataxin-3 construct does not affect the

formation of ataxin-3 droplets, and, for this reason, is a suitable probe to study LLPS of this protein system.

Note that, the evaluation of this set of conditions by sedimentation assays (see Section 2.5.1) would allow to clarify how the labeled and non-labeled forms of ataxin-3 13Q partition into the droplets in the presence of different concentrations of the fluorescent construct.

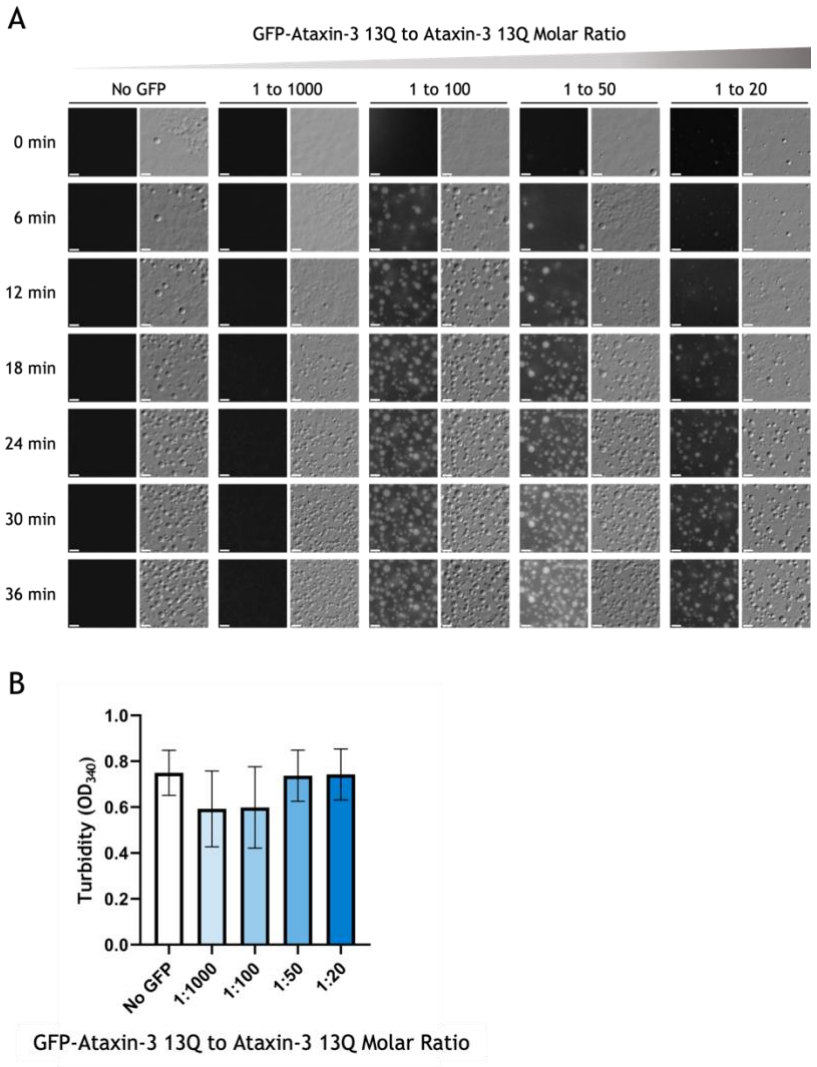


Figure 17 Effect of GFP-ataxin-3 13Q concentration on the LLPS of ataxin-3 13Q. (A) Microscopy images of ataxin-3 13Q droplets in the presence of different GFP-ataxin-3 13Q concentrations. Ataxin-3 13Q (100 μM), PEG 10000 [15 % (w/v)], and NaCl (150 mM) concentrations were kept constant. For each one of the evaluated conditions, FITC (on the left) and DIC (on the right) images were acquired every 5 minutes for 30 minutes. The scale bar corresponds to 10 μm. **(B)** Turbidity measurements at 340 nm of the ataxin-3 13Q solutions with varying concentrations of GFP-ataxin-3 13Q. Experiments were performed in triplicate and the mean value ± standard deviation is presented.

4.2.4 Determination of the Saturation Concentration of Ataxin-3 13Q for Liquid-Liquid Phase Separation

The saturation concentration for LLPS is defined as the threshold concentration above which a biomolecular system undergoes phase separation[125,175]. In other words, proteins with a high propensity phase separate, even at low concentrations, possess a low saturation concentration. It has been shown that the amino acid sequence of a protein strongly influences its saturation concentration. For instance, by studying LLPS of proteins from the FUS family (e.g., FUS, EWSR1, TAF15, TDP-43, hnRNPA1, among others), Wang et al. showed that the total number of arginine and tyrosine residues in a protein is inversely related to their saturation concentration[125]. The ataxin-3 13Q construct used in this dissertation has 21 and 10 arginine and tyrosine residues, respectively. This amino acid composition is similar to the one of the hnRNPA1a protein (24 and 12 arginine and tyrosine residues, respectively), which undergoes LLPS at a concentration of 100 μM in the presence of 10 % (w/v) dextran[125]. Even so, it was shown that in an environment crowded by 20 % (w/v) PEG, ataxin-3 28Q phase separates at concentrations as low as 20 μM[1]. The molecule's tendency to form liquid-liquid phase-separated condensates is also highly dependent on the environmental conditions that are being used. In fact, in addition to biomolecular crowding, other factors such as ionic strength, temperature, and pH will dictate the LLPS of a protein[22,178].

To estimate the saturation concentration of ataxin-3 13Q, under a specific set of environmental conditions [15 % (w/v) PEG, 150 mM NaCl, and pH 7.5], the set of experiments shown in Figure 18 were done. By varying the protein concentration in solution, it was also possible to determine how specific properties of the formed droplets (e.g., number and size distribution) change between conditions.

Small fluorescent spots are already observed at a protein concentration of 25 μM (Figure 18A). This indicates that the saturation concentration threshold has already been crossed. Even so, the turbidity measurements don't show any significant differences between this condition and the one where no protein is added to the solution. In fact, solution turbidity only becomes relevantly increased at a concentration of 50 μM or higher (Figure 18B). It is worth noting that two different protein batches, each one resulting from a distinct purification process, were used for the two experimental methods. This can account for some of the discrepancy of the results obtained with the different techniques. Nonetheless, by visualization of the droplets, one can conclude that the rise in ataxin-3 13Q concentration also seems to be accompanied by an increase in droplet number and size. Furthermore, at the higher concentration (i.e., 100 μM) all droplets possess a rounded shape, while at lower ones, the condensates assemble into structures that are not usually seen for structures of liquid nature[177]. For this reason, we selected the 100 μM ataxin-3 13Q condition for future experiments.

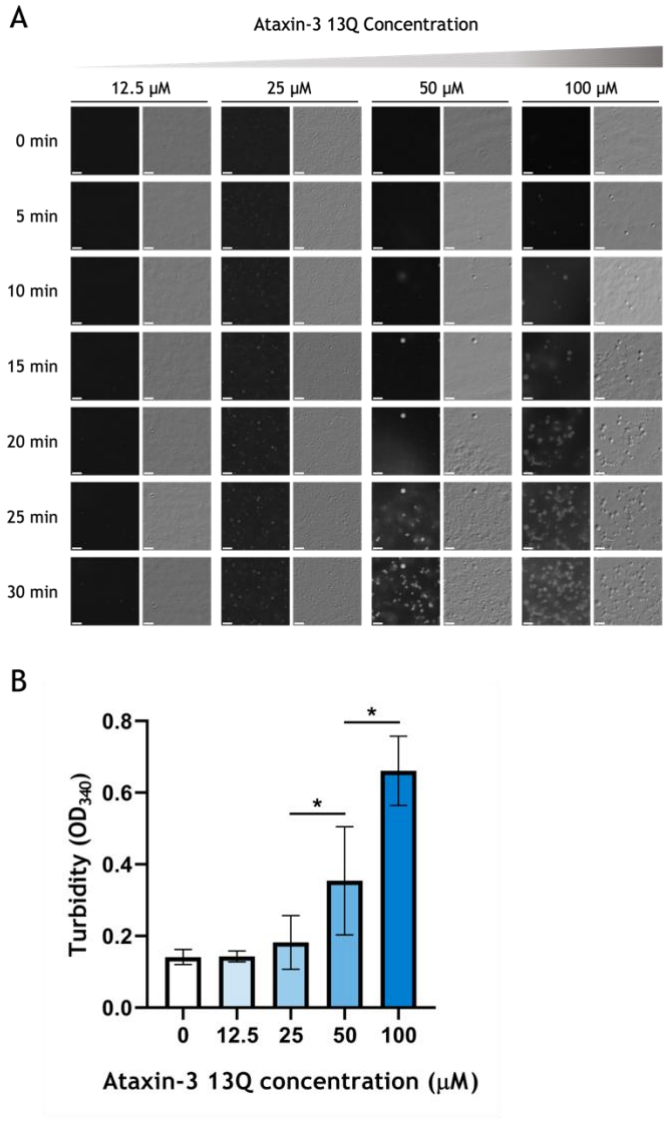


Figure 18 Effect of protein concentration on the LLPS of ataxin-3 13Q. (A) Microscopy images of ataxin-3 13Q droplets in the presence of different protein concentrations. GFP-ataxin-3 13Q (10 µM), PEG 10000 [15 % (w/v)], and NaCl (150 mM) concentrations were kept constant. For each one of the evaluated conditions, FITC (on the left) and DIC (on the right) images were acquired every 5 minutes for 30 minutes. The scale bar corresponds to 10 µm. **(B)** Turbidity measurements at 340 nm of the ataxin-3 13Q solutions with varying protein concentration. Experiments were performed in triplicate and the mean value ± standard deviation is presented. Values were compared by One-WAY ANOVA (*p-value ≤ 0.0001).

4.2.5 High-Salt Regime Promotes Ataxin-3 13Q Liquid-Liquid Phase Separation

As previously mentioned, the ionic strength of a solution plays an important role for determining the LLPS behavior of a protein. While some molecules preferentially phase-separate at low salt concentrations, others exhibit the opposite behavior[178,192]. More recently, an additional type of molecular behavior was described for proteins such as FUS, TDP-43, Brd4,

Sox2, and Annexin A11[22]. In fact, these proteins form liquid condensates at low salt concentration (e.g., 50 mM NaCl), which at intermediate values of salt concentration (e.g., 500 mM NaCl) disassemble into the dilute phase. However, raising the ionic strength of the solution beyond physiological values (e.g., >1.5 M NaCl) results in a reentrant LLPS[22]. While condensate assembly in the low-salt regime is mediated by both electrostatic and hydrophobic interactions, in the high-salt regime only hydrophobic and non-ionic interactions promote the LLPS of these proteins[22].

An initial study of the LLPS behavior of ataxin-3 28Q in response to changes in ionic strength was performed by Murakami et al.[1]. By testing three different NaCl concentrations between 0 and 150 mM they showed that there is a rise in the solution's turbidity that follows the increase in salt concentration[1]. In the present study, we confirmed these results for the ataxin-3 13Q construct by microscopy imaging and turbidimetry. Furthermore, we evaluated two additional salt concentrations (200 and 400 mM NaCl). Although these high salt concentrations are no longer physiological, they help to elucidate the type of molecular interaction that is promoting ataxin-3 droplet assembly.

The microscopy images (Figure 19A) show that, although phase separation occurs in all of the tested conditions, both droplet number and size increase with the ionic strength. On the other hand, the turbidity values appear to stabilize at salt concentrations superior to 150 mM (Figure 19B). In fact, the results obtained by latter technique don't inform us on particle type, size, shape, or number, which highlights why multiple experimental techniques should be used together to characterize the LLPS behavior of a protein system.

Because a high-salt regime promotes LLPS of ataxin-3, it has been proposed that hydrophobic interactions are involved in droplet formation. In agreement with this theory, it was previously reported that the addition of 1,6-hexanediol to the LLPS solution reduces its turbidity to approximately half of the original value[1]. To characterize the nature of the particles that persist in solution, future experimental plans should include a microscopy analysis of the samples following hydrophobic interaction disruption. In fact, this was done for huntingtin exon1 and revealed that, fibrillary structures remained in the place of droplets, which could indicate that protein aggregation was taking place inside of the condensates.

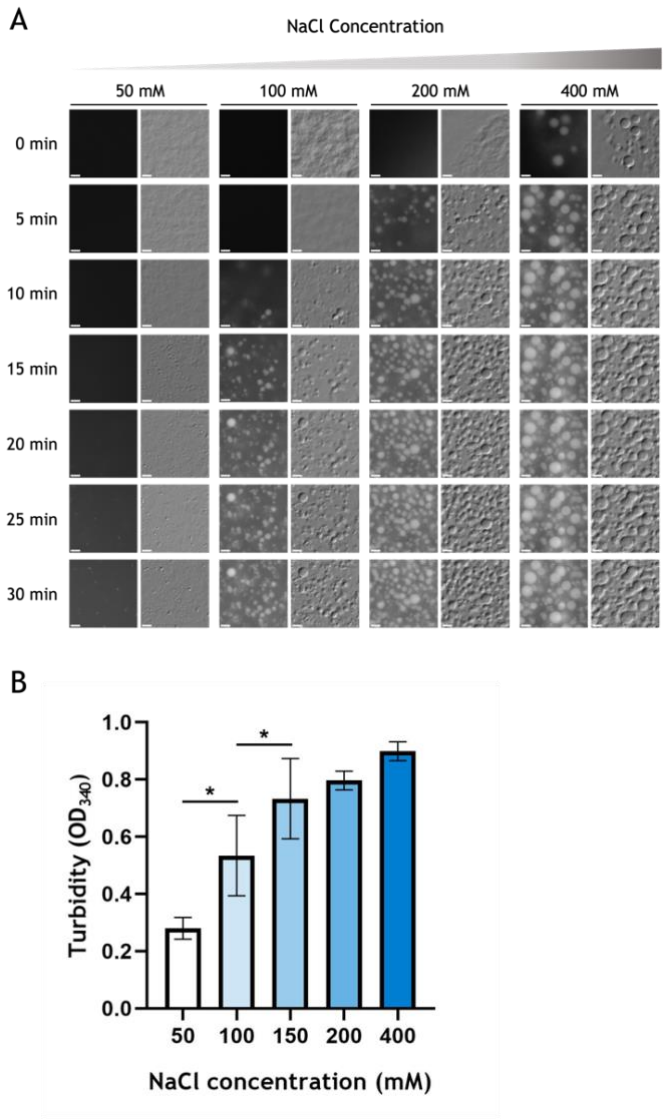


Figure 19 Effect of NaCl concentration on the LLPS of ataxin-3 13Q. (A) Microscopy images of ataxin-3 13Q droplets in the presence of different NaCl concentrations. Ataxin-3 13Q (100 μM), GFP-ataxin-3 13Q (4 μM), and PEG 10000 [15 % (w/v)] concentrations were kept constant. For each one of the evaluated conditions, FITC (on the left) and DIC (on the right) images were acquired every 5 minutes for 30 minutes. The scale bar corresponds to 10 μm. **(B)** Turbidity measurements at 340 nm of the ataxin-3 13Q solutions with varying concentrations of NaCl. Experiments were performed in triplicate and the mean value ± standard deviation is presented. Values were compared by One-WAY ANOVA (*p-value ≤ 0.0001).

The observation that ataxin-3 LLPS is promoted at a high-salt regime led us to investigate the effects of ionic strength on the protein's saturation concentration for phase separation (Figure 20). As expected, both droplet number and size are increased in response to higher protein and salt concentrations. Even so, condensate formation was never detected at 12.5 μM. For this reason, with the specific protein concentrations that were tested, we couldn't determine the extent to which the saturation concentration for LLPS was altered by increasing the ionic strength. In the future, using smaller protein concentration intervals between conditions might allow us to precisely identify the saturation concentration of our

protein system. On the other hand, decreasing NaCl concentration to 50 mM was enough to prevent LLPS at protein concentrations ≤ 50 μM.

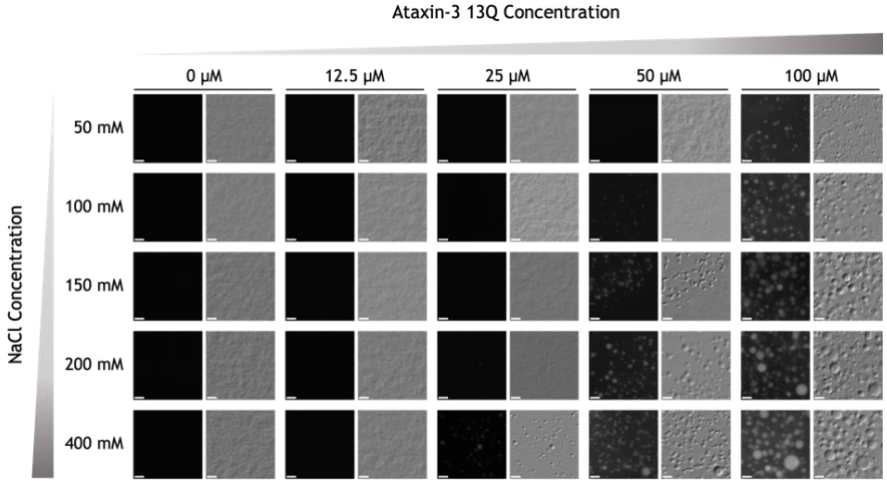


Figure 20 Effect of NaCl concentration on the saturation concentration for the LLPS of ataxin-3 13Q. Microscopy images of ataxin-3 13Q droplets in the presence of different NaCl and protein concentrations. GFP-ataxin-3 13Q (4 μM), and PEG 10000 [15 % (w/v)] concentrations were kept constant. For each one of the evaluated conditions, FITC (on the left) and DIC (on the right) images were acquired 30 minutes after sample preparation. The scale bar corresponds to 10 μm.

Finally, we evaluated if a variation in NaCl concentration would reduce the necessity of a crowded environment for ataxin-3 LLPS to take place. The grid presented in Figure 21 shows, once again, that an increase in both PEG and NaCl concentration promotes the protein's phase separation behavior. This is mostly represented by an increase in droplet size and not droplet number. Still, at PEG concentrations of 0-5 % (w/v), condensate formation was never observed, independently of the ionic strength of the solution. A few conditions from the 20 % (w/v) PEG row, namely at 100 and 150 mM NaCl, are enriched in structures that resemble accumulation of multiple droplets in one place, which is a common characteristic of gel-like condensates. This suggests that a highly crowded environment might promote the formation of irreversible connections between molecules, ultimately leading to the conversion of liquid-like droplets to gel-like condensates. This theory could be confirmed by experimental determination of the material properties of the droplets by FRAP assays.

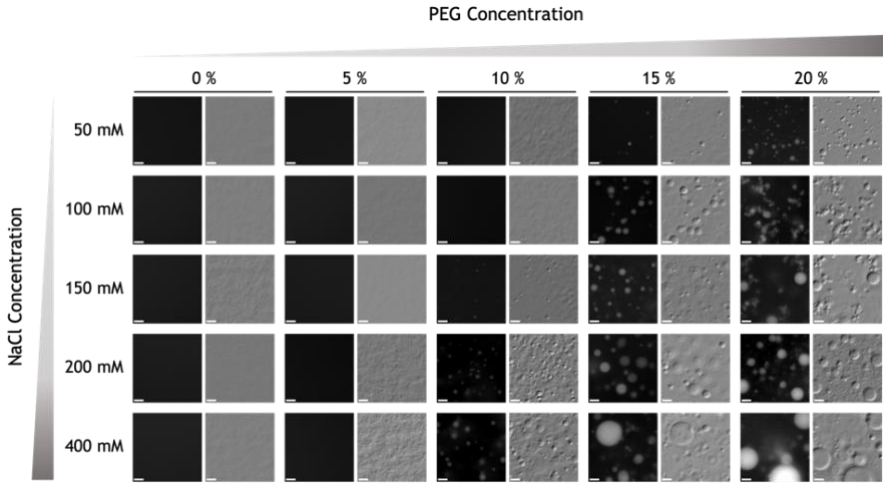


Figure 21 Effect of NaCl concentration on the crowding agent-dependent LLPS of ataxin-3 13Q. Microscopy images of ataxin-3 13Q droplets in the presence of different NaCl and PEG 1000 concentrations. Ataxin-3 13Q (100 μM), GFP-ataxin-3 13Q (4 μM) concentrations were kept constant. For each one of the evaluated conditions, FITC (on the left) and DIC (on the right) images were acquired 30 minutes after sample preparation. The scale bar corresponds to 10 μm.

4.2.6 The Effect of Buffer Type on Ataxin-3 Liquid-Liquid Phase Separation

Ataxin-3 aggregation assays have revealed that the rate of irreversible amyloid-like fibril assembly, monitored by ThT fluorescence, is dependent on the used buffer type (i.e., phosphate versus HEPES buffer)[144]. In fact, in phosphate buffer, there is a long lag phase before the intensity of the fluorescent signal increases and reaches a plateau[144]. On the other hand, when HEPES buffer is used, the lag phase is reduced, and the aggregation process is faster[144]. As LLPS has been proposed to act as a preceding step to protein aggregation[14], we aimed to study if the phase separation of ataxin-3 can also be modulated by changing the buffer type.

The microscopy imaging results (Figure 22A) show that, in both buffer types, an increase in protein concentration translates into the formation of more droplets of a bigger size. Note that, in the condition with the highest protein concentration (i.e., 100 μM), the HEPES buffer seems to promote condensate formation to a larger degree than the phosphate buffer, as more droplets are present in solution since the first time point. If ataxin-3 LLPS does lead to protein aggregation, like it has been proposed for other neurodegenerative disease causative proteins, the increased phase separation behavior in this particular buffer may help to explain why amyloid-like fibril assembly is accelerated in HEPES. The degree of protein aggregation inside of liquid droplets formed in different buffering conditions can be quantified by future FRAP assays, as solid aggregates don't exchange with the surrounding environment and, consequently, do not recover after photobleaching.

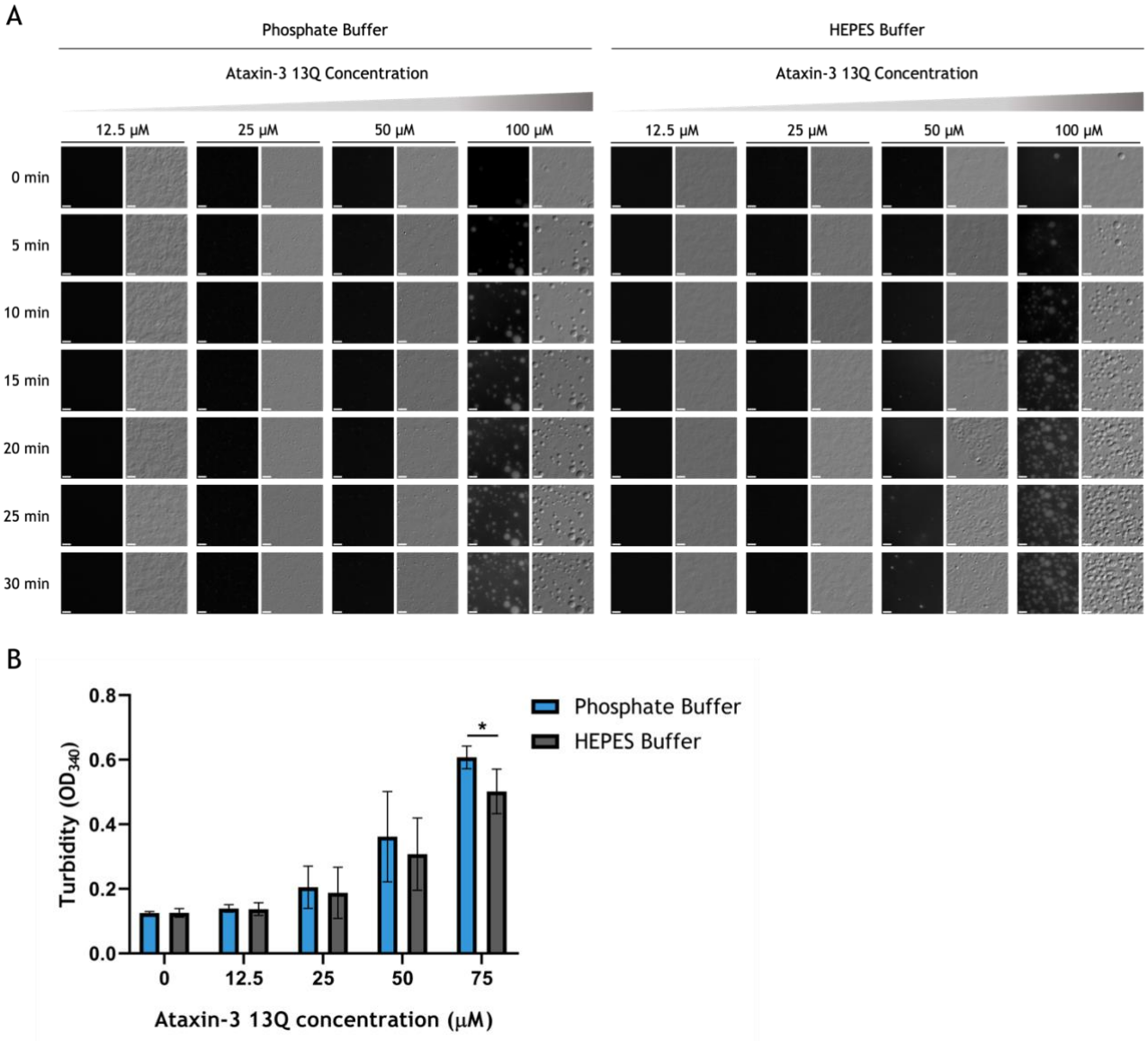


Figure 22 Effect of buffer type on the LLPS behavior of ataxin-3. (A) Microscopy images of ataxin-3 13Q droplets in the presence of two different buffers (i.e., Phosphate or HEPES). Four different protein concentrations were also tested. GFP-ataxin-3 13Q (4 µM), and PEG 10000 [15 % (w/v)] concentrations were kept constant. For each one of the evaluated conditions, FITC (on the left) and DIC (on the right) images were acquired every 5 minutes for 30 minutes. The scale bar corresponds to 10 µm. **(B)** Turbidity measurements at 340 nm of the ataxin-3 13Q solutions. Experiments were performed in triplicate and the mean value ± standard deviation is presented. Values were compared by One-WAY ANOVA (*p-value ≤ 0.0001).

Due to protein loss during the sample preparation protocol (see Section 3.2.6), the 100 µM ataxin-3 13Q condition wasn't evaluated by turbidimetry. Instead, a lower concentration of 75 µM was used. The results obtained by this technique (Figure 22B) reveal that the only significant differences in sample turbidity are between the two conditions with the highest protein concentration. However, and contradicting what was described above for the

microscopy analysis, it is the phosphate buffer that drives the formation of a solution with a higher turbidity. The fact that the turbidimetry assays measure dispersion of the whole liquid sample, while in the microscopy experiments only a specific focus field is being acquired, can to a certain extent justify the differences in the results obtained by the two techniques. In future experiments, it would be essential to also quantify the turbidity for the 100 μM ataxin-3 13Q samples to determine if what was observed by microscopy is reproducible (i.e., more LLPS in HEPES buffer), or if the trend of the turbidimetry assays continues (i.e., more LLPS in phosphate buffer). The conjugation of microscopy assays with ThT staining could also clarify if any of the tested conditions stimulates the evolution of the droplets into amyloid-like protofibrils, as liquid droplets formed by LLPS has been shown to evolve into solid-like structures for other protein systems[9,10].

4.3 Identification of the Ataxin-3 Region Responsible for Liquid-Liquid Phase Separation

Murakami et al. showed that the JD of ataxin-3 alone will not undergo LLPS, even in the presence of a crowded environment[1]. This led the authors to conclude that the polyQ tract of ataxin-3 is the primary domain responsible for LLPS induction. However, the bioinformatic analysis of the ataxin-3 13Q construct's sequence by the FuzDrop server (see Section 4.1.2) identified a shorter DPR outside of the polyQ tract of the protein. To determine if this region alone is sufficient to promote phase separation, we characterized the LLPS behavior of the ataxin-3 D1 construct, which, in addition to the N-terminal folded JD, also contains the first two UIMs of the protein. Our main goals were to evaluate how the saturation concentration for LLPS is altered in this truncated variant of ataxin-3, and, also, reveal if the same type of interactions (i.e., hydrophobic interactions) are involved in the condensation of this construct.

Note that, ataxin-3 D1 has a FuzDrop predicted probability of spontaneous liquid-liquid phase separation of 0.2019. For this reason, we expected that a higher concentration of protein would be necessary for LLPS to take place. This was, in fact, confirmed by both microscopy and turbidimetry assays (Figure 23). Furthermore, LLPS was once again enhanced at higher NaCl concentrations, highlighting that the hydrophobic interactions that are favored under these conditions govern the phase separation of this construct as well.

Following these experiments, it would be important to also evaluate the LLPS of a protein construct that spans from the C-terminal extremity of the second UIM to the C-terminus of ataxin-3 13Q so that the second DPR predicted by FuzDrop could be characterized on its own. In addition, mixing the two truncated constructs at a 1:1 molar ratio would clarify

if both portions of ataxin-3 13Q are necessary to reproduce what is observed for the full-length protein or if one of them assumes a greater importance for LLPS than the other.

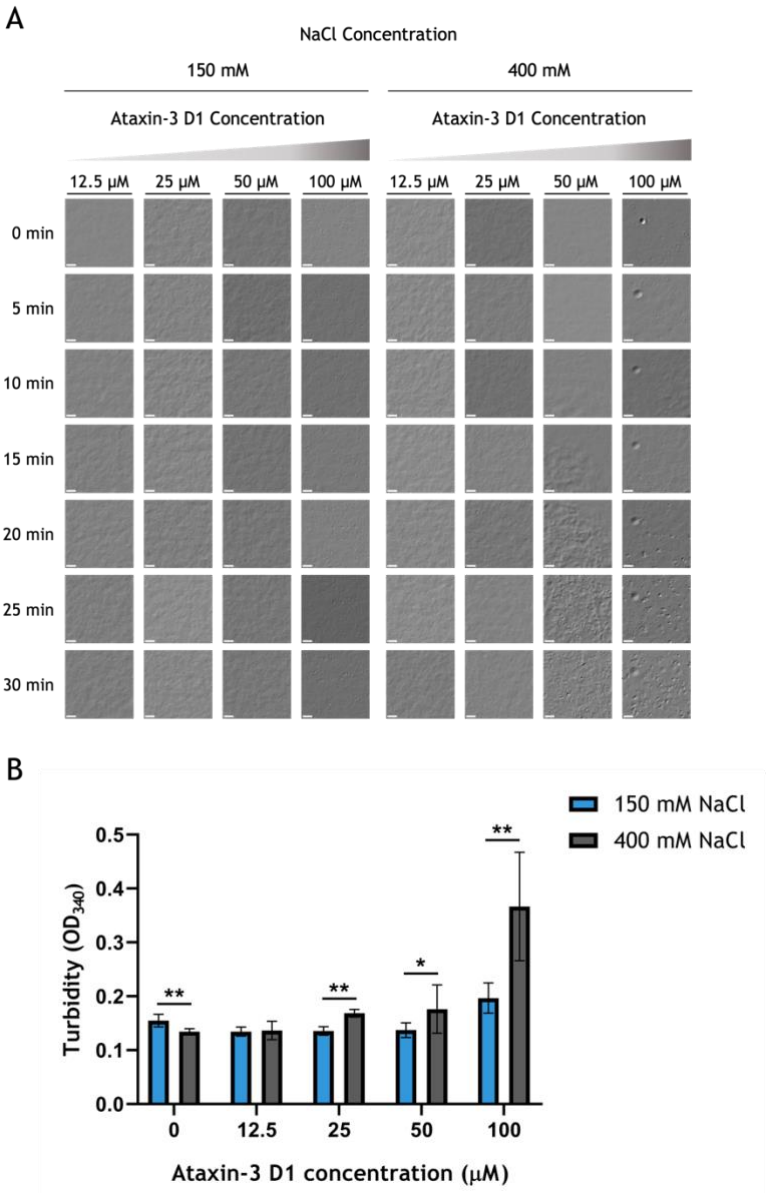


Figure 23 Characterization of the LLPS behavior of ataxin-3 D1. (A) Microscopy images of ataxin-3 D1 droplets in the presence of two NaCl concentrations (i.e., 150 and 400 mM). Four different protein concentrations were also tested. PEG 10000 [15 % (w/v)] concentration was kept constant. For each one of the evaluated conditions, DIC images were acquired every 5 minutes for 30 minutes. The scale bar corresponds to 10 µm. **(B)** Turbidity measurements at 340 nm of the ataxin-3 D1. Experiments were performed in triplicate and the mean value ± standard deviation is presented. Values were compared by One-WAY ANOVA (**p*-value ≤ 0.01, ***p*-value ≤ 0.0001).

4.4 Determination of the Material Properties of Ataxin-3 13Q Droplets

The material properties of ataxin-3 13Q droplets were assessed by FRAP experiments. Due to technical limitations of the bleaching process, only conditions that resulted in the formation of large droplets (i.e., of a diameter $\geq$ 5 µm) could be evaluated. For this reason, we set out to characterize how changes in ionic strength modify the material nature of ataxin-3 13Q condensates (Figure 24). It should be noted that the results presented in this dissertation are still preliminary and a higher number of replicates should be analyzed before it is possible to draw definitive conclusions.

As shown in Figure 24C and Table 21, bleaching a circular area of the fluorescent droplets resulted in a recovery of the fluorescence intensity to approximately 60 % of its original value for both NaCl concentrations. In other words, the droplets aren't completely liquid or solid, but rather of an intermediate gel-like nature. This indicates that even when no more than 30 minutes have passed following sample preparation, the droplets might already be undergoing a maturation process promoted by the formation of some solid aggregates inside of them. In the future, it should be studied if the incubation of the LLPS samples for longer periods of time results in a significant decrease in the mobile fraction. Furthermore, the addition of ThT to the sample would clarify if there are any amyloid-like structures being formed from the middle of the droplets.

Although there is no significant difference between the mobile fractions of the condensates in the two conditions that were analyzed, the kinetics of fluorescence recovery appeared to be affected by the solution's ionic strength. In fact, by looking at the initial slope of the recovery curves, one can readily observe that at 400 mM NaCl the recovery is slower (also showed by the diffusion rate in Table 21). The formation of a molecular mesh with a smaller or fewer pores under high-salt conditions may be the reason why the movement the molecules that are still in the liquid state is constricted.

Table 21 Variation in the mobile fraction and diffusion coefficient in response to changes in the ionic strength. Values are presented as mean $\pm$ standard deviation.

Test Condition	Mobile Fraction	Diffusion Coefficient ($\mu m^2/s$)
150 mM	0.63 ± 0.02	0.130 ± 0.036
400 mM	0.62 ± 0.04	0.055 ± 0.004

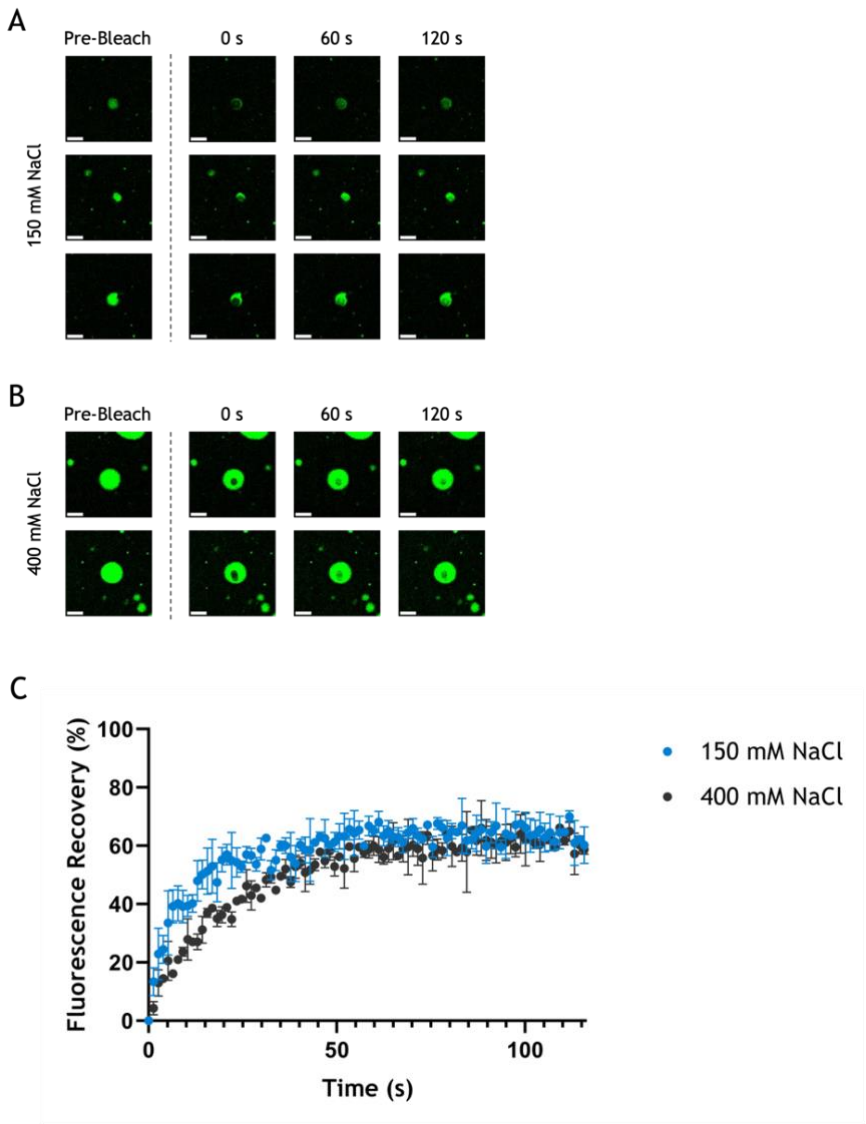


Figure 24 Characterization of the material properties of ataxin-3 13Q droplets at different salt concentrations. Confocal microscope images of the fluorescence recovery of ataxin-3 13Q droplets following the bleaching of a circular region at **(A)** 150 mM and **(B)** 400 mM NaCl. The dashed lines represent the moment of bleaching. The scale bar corresponds to 10 μm. **(C)** Average FRAP recovery for ataxin-3 13Q droplets at the two NaCl concentrations. Experiments were performed in triplicate or duplicate and the mean value ± standard deviation is presented.

In the future, the effect of other environmental parameters, such as crowding agent concentration and buffer type, on the material characteristics of ataxin-3 droplets should also be studied. In fact, from simple visualization of the droplets we observe that at a higher PEG concentration [i.e., 20 % (v/v)] the condensates possess some morphological characteristics that are often associated with more gel-like materials. Furthermore, HEPES buffer has been

shown to accelerate the aggregation process of ataxin-3 13Q, which should translate into more solid-like condensates under this buffering condition.

Chapter 5

Conclusions and Future Perspectives

With the experimental work presented in this dissertation, we demonstrated that the ataxin-3 LLPS behavior is sensitive to changes in the composition of its environment. Indeed, the presence of a crowding agent (i.e., PEG 10000), which aims to mimic the intracellular environment, is fundamental for phase separation to take place and increasing its concentration promoted the formation of more droplets with bigger size. Future FRAP experiments at different crowding conditions will help us to determine how the material nature of the formed condensates is modulated.

Increasing the ionic strength of the solution also favored the formation of ataxin-3-enriched condensates. It was shown that the saturation concentration for ataxin-3 LLPS decreases with an increase in NaCl concentration. A high-salt regime promotes protein interaction through hydrophobic connections. Hence, we propose that these non-electrostatic interactions are the ones responsible for the formation of a condensed phase in the studied protein system. When assessing the effects of salt concentration on the material properties of the droplets by FRAP it was found that, although the mobile fraction remained unchanged, the diffusion rate of the molecules becomes compromised in the high-salt regime. As hydrophobic interactions become more relevant in this environmental condition, there might be a formation of a more tightly packed biomolecular network that slows down the movement of the molecules that remain in the liquid state. In contrast to what was described for the aggregation of this protein, when only considering droplet number and solution turbidity, ataxin-3 LLPS wasn´t significantly when comparing HEPES and phosphate buffers. However, this relationship should be further explored by FRAP analysis, because if protein aggregation is indeed enhanced in the droplets formed in HEPES buffer, there should be an observable decrease in the mobile fraction. Microscopy imaging experiments with the addition of ThT to the sample will also help to determine if LLPS and amyloid formation are on the same pathway for protein aggregation.

Furthermore, we also propose that the region containing the first two UIMs of ataxin-3 may contribute to the LLPS behavior of ataxin-3 13Q. In fact, it has been previously described

that the JD alone cannot undergo LLPS at any concentration between 0-100 μM, even at extreme biomolecular crowding conditions. However, here we show that the D1 construct, which in addition to the JD also includes UIM1 and UIM2, can phase separate, and that this phenomenon is modulated by ionic strength in a similar manner to the full-length protein. This hypothesis is also supported by the bioinformatic analysis of ataxin-3 sequence with FuzDrop tool, which predicts the presence of a shorter DPR in the preceding region of UIM1.

The ability of droplets to relax upon fusion is also a primary characteristic of condensates formed by LLPS. Even so, we didn't observe any clear fusion event in any of the microscopy assays that were conducted in this work. To confirm whether this protein system is capable of undergoing spontaneous fusion, we propose that, in the future, a multicolor labeling experiment should be performed. For that we propose to label ataxin-3 separately with two different fluorophores and then mix both protein samples. If two droplets, one from each solution, fuse, both fluorescent proteins will co-localize in the droplets.

Ataxin-3 is a protein with an extensive interactome[193]. For this reason, it would be also important to determine how the presence of some of its binding partners affects the protein's propensity to undergo LLPS. This will help to elucidate if LLPS is a necessary biomolecular process for the physiological function of ataxin-3.

Only the non-expanded form of ataxin-3 has been studied in the field of LLPS thus far. As disease-related mutations in other neurodegenerative disease causative proteins have been shown to significantly alter their phase separation behavior it is also essential to characterize the condensation of the expanded ataxin-3. The identification of an aberrant LLPS behavior in the mutated form of ataxin-3, manifesting through either, for example, an enhancement of droplet formation or an acceleration of the maturation process, will further deepen our understanding on what are the pathological phenomena that take place in the neurons of MJD patients.

In summary, this dissertation describes how different experimental techniques can be used to monitor specific characteristic of LLPS systems such as droplet size, number, and material properties) in the presence of different environmental conditions. As it contains a detailed evaluation of the LLPS behavior of non-expanded ataxin-3, this study can also be used as a control to be compared with future experiments with the abnormally expanded protein.

References

1 Murakami, K. *et al*. Observation of liquid–liquid phase separation of ataxin-3 and quantitative evaluation of its concentration in a single droplet using Raman microscopy. *Chemical science* **12**, 7411-7418 (2021).

2 Hyman, A. A., Weber, C. A. & Jülicher, F. Liquid-liquid phase separation in biology. *Annual review of cell and developmental biology* **30**, 39-58 (2014).

3 Zbinden, A., Pérez-Berlanga, M., De Rossi, P. & Polymenidou, M. Phase separation and neurodegenerative diseases: a disturbance in the force. *Developmental cell* **55**, 45-68 (2020).

4 Alberti, S. & Dormann, D. Liquid–liquid phase separation in disease. *Annual review of genetics* **53**, 171-194 (2019).

5 Wilson, E. B. The structure of protoplasm. *Science* **10**, 33-45 (1899).

6 Lyon, A. S., Peeples, W. B. & Rosen, M. K. A framework for understanding the functions of biomolecular condensates across scales. *Nature Reviews Molecular Cell Biology* **22**, 215-235 (2021).

7 Banani, S. F., Lee, H. O., Hyman, A. A. & Rosen, M. K. Biomolecular condensates: organizers of cellular biochemistry. *Nature reviews Molecular cell biology* **18**, 285-298 (2017).

8 Alberti, S. & Hyman, A. A. Biomolecular condensates at the nexus of cellular stress, protein aggregation disease and ageing. *Nature Reviews Molecular Cell Biology* **22**, 196-213 (2021).

9 Patel, A. *et al*. A liquid-to-solid phase transition of the ALS protein FUS accelerated by disease mutation. *Cell* **162**, 1066-1077 (2015).

10 Peskett, T. R. *et al*. A liquid to solid phase transition underlying pathological huntingtin exon1 aggregation. *Molecular cell* **70**, 588-601. e586 (2018).

11 Wegmann, S. *et al*. Tau protein liquid–liquid phase separation can initiate tau aggregation. *The EMBO journal* **37**, e98049 (2018).

12 Ray, S. *et al*. α-Synuclein aggregation nucleates through liquid–liquid phase separation. *Nature chemistry* **12**, 705-716 (2020).

13 Shin, Y. & Brangwynne, C. P. Liquid phase condensation in cell physiology and disease. *Science* **357**, eaaf4382 (2017).

14 Vendruscolo, M. & Fuxreiter, M. Sequence determinants of the aggregation of proteins within condensates generated by liquid-liquid phase separation. *Journal of Molecular Biology* **434**, 167201 (2022).

15 Alberti, S. & Hyman, A. A. Are aberrant phase transitions a driver of cellular aging? *BioEssays* **38**, 959-968 (2016).

16 Li, T. *et al*. Is the high frequency of Machado-Joseph disease in China due to new mutational origins? *Frontiers in genetics* **9**, 740 (2019).

17 Bettencourt, C. & Lima, M. Machado-Joseph Disease: from first descriptions to new perspectives. *Orphanet journal of rare diseases* **6**, 1-12 (2011).

18 Schöls, L., Bauer, P., Schmidt, T., Schulte, T. & Riess, O. Autosomal dominant cerebellar ataxias: clinical features, genetics, and pathogenesis. *The Lancet Neurology* **3**, 291-304 (2004).

19 Evers, M. M., Toonen, L. J. & van Roon-Mom, W. Ataxin-3 protein and RNA toxicity in spinocerebellar ataxia type 3: current insights and emerging therapeutic strategies. *Molecular neurobiology* **49**, 1513-1531 (2014).
20 Scarff, C. A. *et al*. Examination of ataxin-3 (atx-3) aggregation by structural mass spectrometry techniques: a rationale for expedited aggregation upon polyglutamine (polyQ) expansion. *Molecular & Cellular Proteomics* **14**, 1241-1253 (2015).
21 Sicorello, A. *et al*. The Structural properties in solution of the intrinsically mixed folded protein ataxin-3. *Biophysical journal* **115**, 59-71 (2018).
22 Krainer, G. *et al*. Reentrant liquid condensate phase of proteins is stabilized by hydrophobic and non-ionic interactions. *Nature Communications* **12**, 1085, doi:10.1038/s41467-021-21181-9 (2021).
23 Hayashi, Y., Ford, L. K., Fioriti, L., McGurk, L. & Zhang, M. Liquid-liquid phase separation in physiology and pathophysiology of the nervous system. *Journal of Neuroscience* **41**, 834-844 (2021).
24 Boisvert, F.-M., van Koningsbruggen, S., Navascués, J. & Lamond, A. I. The multifunctional nucleolus. *Nature reviews Molecular cell biology* **8**, 574-585 (2007).
25 Brangwynne, C. P., Mitchison, T. J. & Hyman, A. A. Active liquid-like behavior of nucleoli determines their size and shape in Xenopus laevis oocytes. *Proceedings of the National Academy of Sciences* **108**, 4334-4339 (2011).
26 Feric, M. *et al*. Coexisting liquid phases underlie nucleolar subcompartments. *Cell* **165**, 1686-1697 (2016).
27 Gasset-Rosa, F. *et al*. Cytoplasmic TDP-43 de-mixing independent of stress granules drives inhibition of nuclear import, loss of nuclear TDP-43, and cell death. *Neuron* **102**, 339-357. e337 (2019).
28 Li, Y. R., King, O. D., Shorter, J. & Gitler, A. D. Stress granules as crucibles of ALS pathogenesis. *Journal of cell biology* **201**, 361-372 (2013).
29 Decker, C. J. & Parker, R. P-bodies and stress granules: possible roles in the control of translation and mRNA degradation. *Cold Spring Harbor perspectives in biology* **4**, a012286 (2012).
30 Anderson, P. & Kedersha, N. Stress granules. *Current biology* **19**, R397-R398 (2009).
31 Gilks, N. *et al*. Stress granule assembly is mediated by prion-like aggregation of TIA-1. *Molecular biology of the cell* **15**, 5383-5398 (2004).
32 Feng, Z., Chen, X., Zeng, M. & Zhang, M. Phase separation as a mechanism for assembling dynamic postsynaptic density signalling complexes. *Current Opinion in Neurobiology* **57**, 1-8 (2019).
33 Zeng, M. *et al*. Reconstituted Postsynaptic Density as a Molecular Platform for Understanding Synapse Formation and Plasticity. *Cell* **174**, 1172-1187.e1116, (2018).
34 Zeng, M. *et al*. Phase Transition in Postsynaptic Densities Underlies Formation of Synaptic Complexes and Synaptic Plasticity. *Cell* **166**, 1163-1175.e1112, (2016).
35 Sheng, M. & Kim, E. The postsynaptic organization of synapses. *Cold Spring Harbor perspectives in biology* **3**, a005678 (2011).
36 Goode, B. L., Eskin, J. A. & Wendland, B. Actin and endocytosis in budding yeast. *Genetics* **199**, 315-358 (2015).
37 Marlow, F. L. in *Colloquium Series on Developmental Biology*. 1-196 (Morgan & Claypool Life Sciences).
38 Boke, E. *et al*. Amyloid-like self-assembly of a cellular compartment. *Cell* **166**, 637-650 (2016).
39 Handwerger, K. E., Cordero, J. A. & Gall, J. G. Cajal bodies, nucleoli, and speckles in the Xenopus oocyte nucleus have a low-density, sponge-like structure. *Molecular biology of the cell* **16**, 202-211 (2005).
40 Nizami, Z., Deryusheva, S. & Gall, J. G. The Cajal body and histone locus body. *Cold Spring Harbor perspectives in biology* **2**, a000653 (2010).
41 Li, L. *et al*. Dynamic nature of cleavage bodies and their spatial relationship to DDX1 bodies, Cajal bodies, and gems. *Molecular biology of the cell* **17**, 1126-1140 (2006).
42 Case, L. B. & Waterman, C. M. Integration of actin dynamics and cell adhesion by a three-dimensional, mechanosensitive molecular clutch. *Nature cell biology* **17**, 955-963 (2015).

43 Morimoto, M. & Boerkoel, C. F. The role of nuclear bodies in gene expression and disease. *Biology* **2**, 976-1033 (2013).

44 Cauchi, R. J. Gem formation upon constitutive Gemin3 overexpression in Drosophila. *Cell biology international* **35**, 1233-1238 (2011).

45 Voronina, E., Seydoux, G., Sassone-Corsi, P. & Nagamori, I. RNA granules in germ cells. *Cold Spring Harbor perspectives in biology* **3**, a002774 (2011).

46 Brangwynne, C. P. *et al*. Germline P granules are liquid droplets that localize by controlled dissolution/condensation. *Science* **324**, 1729-1732 (2009).

47 Saha, S. *et al*. Polar positioning of phase-separated liquid compartments in cells regulated by an mRNA competition mechanism. *Cell* **166**, 1572-1584. e1516 (2016).

48 Duronio, R. J. & Marzluff, W. F. Coordinating cell cycle-regulated histone gene expression through assembly and function of the Histone Locus Body. *RNA biology* **14**, 726-738 (2017).

49 Jones, N. *et al*. Nck adaptor proteins link nephrin to the actin cytoskeleton of kidney podocytes. *Nature* **440**, 818-823 (2006).

50 Li, P. *et al*. Phase transitions in the assembly of multivalent signalling proteins. *Nature* **483**, 336-340 (2012).

51 Banjade, S. & Rosen, M. K. Phase transitions of multivalent proteins can promote clustering of membrane receptors. *elife* **3**, e04123 (2014).

52 Beck, M. & Hurt, E. The nuclear pore complex: understanding its function through structural insight. *Nature reviews Molecular cell biology* **18**, 73-89 (2017).

53 Spector, D. L. & Lamond, A. I. Nuclear speckles. *Cold Spring Harbor perspectives in biology* **3**, a000646 (2011).

54 Spector, D. L. Nuclear domains. *Journal of cell science* **114**, 2891-2893 (2001).

55 Harrigan, J. A. *et al*. Replication stress induces 53BP1-containing OPT domains in G1 cells. *Journal of Cell Biology* **193**, 97-108 (2011).

56 Fox, A. H. & Lamond, A. I. Paraspeckles. *Cold Spring Harbor perspectives in biology* **2**, a000687 (2010).

57 Hennig, S. *et al*. Prion-like domains in RNA binding proteins are essential for building subnuclear paraspeckles. *Journal of Cell Biology* **210**, 529-539 (2015).

58 Pirrotta, V. & Li, H.-B. A view of nuclear Polycomb bodies. *Current opinion in genetics & development* **22**, 101-109 (2012).

59 Lallemand-Breitenbach, V. PML nuclear bodies. *Cold Spring Harbor perspectives in biology* **2**, a000661 (2010).

60 Calle, Y., Burns, S., Thrasher, A. J. & Jones, G. E. The leukocyte podosome. *European journal of cell biology* **85**, 151-157 (2006).

61 Kiebler, M. A. & Bassell, G. J. Neuronal RNA granules: movers and makers. *Neuron* **51**, 685-690 (2006).

62 Dustin, M. L. & Groves, J. T. Receptor signaling clusters in the immune synapse. *Annual review of biophysics* **41**, 543 (2012).

63 Su, X. *et al*. Phase separation of signaling molecules promotes T cell receptor signal transduction. *Science* **352**, 595-599 (2016).

64 Liu, J.-L. & Gall, J. G. U bodies are cytoplasmic structures that contain uridine-rich small nuclear ribonucleoproteins and associate with P bodies. *Proceedings of the National Academy of Sciences* **104**, 11655-11659 (2007).

65 Douglass, A. D. & Vale, R. D. Single-molecule microscopy reveals plasma membrane microdomains created by protein-protein networks that exclude or trap signaling molecules in T cells. *Cell* **121**, 937-950 (2005).

66 Woodruff, J. B. *et al*. The centrosome is a selective condensate that nucleates microtubules by concentrating tubulin. *Cell* **169**, 1066-1077. e1010 (2017).

67 King, M. R. & Petry, S. Phase separation of TPX2 enhances and spatially coordinates microtubule nucleation. *Nature communications* **11**, 1-13 (2020).

68 Jiang, H. *et al.* Phase transition of spindle-associated protein regulate spindle apparatus assembly. *Cell* **163**, 108-122 (2015).
69 Beutel, O., Maraspini, R., Pombo-Garcia, K., Martin-Lemaitre, C. & Honigmann, A. Phase separation of zonula occludens proteins drives formation of tight junctions. *Cell* **179**, 923-936. e911 (2019).
70 Hirose, T. *et al.* A Highlights from MBoC Selection: NEAT1 long noncoding RNA regulates transcription via protein sequestration within subnuclear bodies. *Molecular Biology of the Cell* **25**, 169 (2014).
71 Sharkey, T. D. in *Encyclopedia of Biological Chemistry III (Third Edition)* (ed Joseph Jez) 399-412 (Elsevier, 2021).
72 Andersson, I. & Backlund, A. Structure and function of Rubisco. *Plant Physiology and Biochemistry* **46**, 275-291 (2008).
73 Rosenzweig, E. S. F. *et al.* The eukaryotic CO2-concentrating organelle is liquid-like and exhibits dynamic reorganization. *Cell* **171**, 148-162. e119 (2017).
74 Chakraborty, A. K. & Weiss, A. Insights into the initiation of TCR signaling. *Nature immunology* **15**, 798-807 (2014).
75 Powers, S. K. *et al.* Nucleo-cytoplasmic partitioning of ARF proteins controls auxin responses in Arabidopsis thaliana. *Molecular cell* **76**, 177-190. e175 (2019).
76 Matsuki, H. *et al.* Both G 3 BP 1 and G 3 BP 2 contribute to stress granule formation. *Genes to Cells* **18**, 135-146 (2013).
77 Yang, P. *et al.* G3BP1 is a tunable switch that triggers phase separation to assemble stress granules. *Cell* **181**, 325-345. e328 (2020).
78 Zhu, L. *et al.* Controlling the material properties and rRNA processing function of the nucleolus using light. *Proceedings of the National Academy of Sciences* **116**, 17330-17335 (2019).
79 Yao, R.-W. *et al.* Nascent pre-rRNA sorting via phase separation drives the assembly of dense fibrillar components in the human nucleolus. *Molecular Cell* **76**, 767-783. e711 (2019).
80 Mitrea, D. M. *et al.* Self-interaction of NPM1 modulates multiple mechanisms of liquid–liquid phase separation. *Nature communications* **9**, 1-13 (2018).
81 Ishizuka, N., Cowan, W. M. & Amaral, D. G. A quantitative analysis of the dendritic organization of pyramidal cells in the rat hippocampus. *Journal of Comparative Neurology* **362**, 17-45 (1995).
82 Donnelly, C. J., Fainzilber, M. & Twiss, J. L. Subcellular communication through RNA transport and localized protein synthesis. *Traffic* **11**, 1498-1505 (2010).
83 Gopal, P. P., Nirschl, J. J., Klinman, E. & Holzbaur, E. L. Amyotrophic lateral sclerosis-linked mutations increase the viscosity of liquid-like TDP-43 RNP granules in neurons. *Proceedings of the National Academy of Sciences* **114**, E2466-E2475 (2017).
84 Liao, Y.-C. *et al.* RNA granules hitchhike on lysosomes for long-distance transport, using annexin A11 as a molecular tether. *Cell* **179**, 147-164. e120 (2019).
85 Riback, J. A. *et al.* Stress-triggered phase separation is an adaptive, evolutionarily tuned response. *Cell* **168**, 1028-1040. e1019 (2017).
86 Yoo, H., Triandafillou, C. & Drummond, D. A. Cellular sensing by phase separation: Using the process, not just the products. *Journal of Biological Chemistry* **294**, 7151-7159 (2019).
87 Tompa, P. Intrinsically disordered proteins: a 10-year recap. *Trends in biochemical sciences* **37**, 509-516 (2012).
88 Uversky, V. N. Intrinsically disordered proteins in overcrowded milieu: Membrane-less organelles, phase separation, and intrinsic disorder. *Current opinion in structural biology* **44**, 18-30 (2017).
89 Romero, P. *et al.* Sequence complexity of disordered protein. *Proteins: Structure, Function, and Bioinformatics* **42**, 38-48 (2001).
90 Vucetic, S., Brown, C. J., Dunker, A. K. & Obradovic, Z. Flavors of protein disorder. *Proteins: Structure, Function, and Bioinformatics* **52**, 573-584 (2003).
91 Brangwynne, C. P., Tompa, P. & Pappu, R. V. Polymer physics of intracellular phase transitions. *Nature Physics* **11**, 899-904 (2015).
92 Qamar, S. *et al.* FUS phase separation is modulated by a molecular chaperone and methylation of arginine cation-π interactions. *Cell* **173**, 720-734. e715 (2018).

93 Monahan, Z. *et al*. Phosphorylation of the FUS low-complexity domain disrupts phase separation, aggregation, and toxicity. *The EMBO journal* **36**, 2951-2967 (2017).

94 Boyko, S., Qi, X., Chen, T.-H., Surewicz, K. & Surewicz, W. K. Liquid–liquid phase separation of tau protein: the crucial role of electrostatic interactions. *Journal of Biological Chemistry* **294**, 11054-11059 (2019).

95 Molliex, A. *et al*. Phase separation by low complexity domains promotes stress granule assembly and drives pathological fibrillization. *Cell* **163**, 123-133 (2015).

96 Lin, Y., Protter, D. S., Rosen, M. K. & Parker, R. Formation and maturation of phase-separated liquid droplets by RNA-binding proteins. *Molecular cell* **60**, 208-219 (2015).

97 Xiang, S. *et al*. The LC domain of hnRNPA2 adopts similar conformations in hydrogel polymers, liquid-like droplets, and nuclei. *Cell* **163**, 829-839 (2015).

98 Nott, T. J. *et al*. Phase transition of a disordered nuage protein generates environmentally responsive membraneless organelles. *Molecular cell* **57**, 936-947 (2015).

99 Wippich, F. *et al*. Dual specificity kinase DYRK3 couples stress granule condensation/dissolution to mTORC1 signaling. *Cell* **152**, 791-805 (2013).

100 Misteli, T. *et al*. Serine phosphorylation of SR proteins is required for their recruitment to sites of transcription in vivo. *The Journal of cell biology* **143**, 297-307 (1998).

101 Petri, S., Grimmler, M., Over, S., Fischer, U. & Gruss, O. J. Dephosphorylation of survival motor neurons (SMN) by PPM1G/PP2Cγ governs Cajal body localization and stability of the SMN complex. *The Journal of cell biology* **179**, 451-465 (2007).

102 Wang, J. T. *et al*. Regulation of RNA granule dynamics by phosphorylation of serine-rich, intrinsically disordered proteins in C. elegans. *Elife* **3**, e04591 (2014).

103 Guillén-Boixet, J., Buzon, V., Salvatella, X. & Méndez, R. CPEB4 is regulated during cell cycle by ERK2/Cdk1-mediated phosphorylation and its assembly into liquid-like droplets. *Elife* **5**, e19298 (2016).

104 Hearst, S. M. *et al*. Cajal-body formation correlates with differential coilin phosphorylation in primary and transformed cell lines. *Journal of cell science* **122**, 1872-1881 (2009).

105 Castello, A. *et al*. Insights into RNA biology from an atlas of mammalian mRNA-binding proteins. *Cell* **149**, 1393-1406 (2012).

106 Berry, J., Weber, S. C., Vaidya, N., Haataja, M. & Brangwynne, C. P. RNA transcription modulates phase transition-driven nuclear body assembly. *Proceedings of the National Academy of Sciences* **112**, E5237-E5245 (2015).

107 Aguzzi, A. & Altmeyer, M. Phase separation: linking cellular compartmentalization to disease. *Trends in cell biology* **26**, 547-558 (2016).

108 Zempel, H., Thies, E., Mandelkow, E. & Mandelkow, E.-M. Aß Oligomers Cause Localized Ca²⁺ Elevation, Missorting of Endogenous Tau into Dendrites, Tau Phosphorylation, and Destruction of Microtubules and Spines. *The Journal of Neuroscience* **30**, 11938, doi:10.1523/JNEUROSCI.2357-10.2010 (2010).

109 D'Aguanno, V. *et al*. Systemic amyloidosis: a contemporary overview. *Clinical Reviews in Allergy & Immunology* **59**, 304-322 (2020).

110 Dobson, C. M. The amyloid phenomenon and its links with human disease. *Cold Spring Harbor perspectives in biology* **9**, a023648 (2017).

111 Wördehoff, M. M. & Hoyer, W. α-Synuclein aggregation monitored by thioflavin T fluorescence assay. *Bio-protocol* **8**, e2941-e2941 (2018).

112 Babinchak, W. M. & Surewicz, W. K. Liquid–liquid phase separation and its mechanistic role in pathological protein aggregation. *Journal of molecular biology* **432**, 1910-1925 (2020).

113 Bosco, D. A. *et al*. Mutant FUS proteins that cause amyotrophic lateral sclerosis incorporate into stress granules. *Human molecular genetics* **19**, 4160-4175 (2010).

114 Dewey, C. M. *et al*. TDP-43 is directed to stress granules by sorbitol, a novel physiological osmotic and oxidative stressor. *Molecular and cellular biology* **31**, 1098-1108 (2011).
115 Kim, H. J. *et al*. Mutations in prion-like domains in hnRNPA2B1 and hnRNPA1 cause multisystem proteinopathy and ALS. *Nature* **495**, 467-473 (2013).
116 Mackenzie, I. R. *et al*. TIA1 mutations in amyotrophic lateral sclerosis and frontotemporal dementia promote phase separation and alter stress granule dynamics. *Neuron* **95**, 808-816. e809 (2017).
117 Bentmann, E. *et al*. Requirements for stress granule recruitment of fused in sarcoma (FUS) and TAR DNA-binding protein of 43 kDa (TDP-43). *Journal of Biological Chemistry* **287**, 23079-23094 (2012).
118 Alami, N. H. *et al*. Axonal transport of TDP-43 mRNA granules is impaired by ALS-causing mutations. *Neuron* **81**, 536-543 (2014).
119 Liu-Yesucevitz, L. *et al*. Tar DNA binding protein-43 (TDP-43) associates with stress granules: analysis of cultured cells and pathological brain tissue. *PloS one* **5**, e13250 (2010).
120 Murakami, T. *et al*. ALS/FTD mutation-induced phase transition of FUS liquid droplets and reversible hydrogels into irreversible hydrogels impairs RNP granule function. *Neuron* **88**, 678-690 (2015).
121 Dormann, D. *et al*. ALS-associated fused in sarcoma (FUS) mutations disrupt Transportin-mediated nuclear import. *The EMBO journal* **29**, 2841-2857 (2010).
122 Hofweber, M. *et al*. Phase separation of FUS is suppressed by its nuclear import receptor and arginine methylation. *Cell* **173**, 706-719. e713 (2018).
123 Hofweber, M. & Dormann, D. Friend or foe—Post-translational modifications as regulators of phase separation and RNP granule dynamics. *Journal of Biological Chemistry* **294**, 7137-7150 (2019).
124 Suárez-Calvet, M. *et al*. Monomethylated and unmethylated FUS exhibit increased binding to Transportin and distinguish FTLD-FUS from ALS-FUS. *Acta neuropathologica* **131**, 587-604 (2016).
125 Wang, J. *et al*. A molecular grammar governing the driving forces for phase separation of prion-like RNA binding proteins. *Cell* **174**, 688-699. e616 (2018).
126 Hasegawa, M. *et al*. Phosphorylated TDP-43 in frontotemporal lobar degeneration and amyotrophic lateral sclerosis. *Annals of Neurology: Official Journal of the American Neurological Association and the Child Neurology Society* **64**, 60-70 (2008).
127 Kametani, F. *et al*. Mass spectrometric analysis of accumulated TDP-43 in amyotrophic lateral sclerosis brains. *Scientific reports* **6**, 1-15 (2016).
128 Cvetković-Dožić, D., Skender-Gazibara, M. & Dožić, S. Neuropathological hallmarks of Alzheimer's disease. *Archive of Oncology* **9**, 195-199 (2001).
129 Hernández-Vega, A. *et al*. Local nucleation of microtubule bundles through tubulin concentration into a condensed tau phase. *Cell reports* **20**, 2304-2312 (2017).
130 Zhang, X. *et al*. RNA stores tau reversibly in complex coacervates. *PLoS biology* **15**, e2002183 (2017).
131 Ambadipudi, S., Biernat, J., Riedel, D., Mandelkow, E. & Zweckstetter, M. Liquid–liquid phase separation of the microtubule-binding repeats of the Alzheimer-related protein Tau. *Nature communications* **8**, 1-13 (2017).
132 Hardenberg, M. C. *et al*. Observation of an α-synuclein liquid droplet state and its maturation into Lewy body-like assemblies. *Journal of molecular cell biology* **13**, 282-294 (2021).
133 Fan, H.-C. *et al*. Polyglutamine (PolyQ) diseases: genetics to treatments. *Cell transplantation* **23**, 441-458 (2014).
134 Zu, T., Pattamatta, A. & Ranum, L. P. Repeat-associated non-ATG translation in neurological diseases. *Cold Spring Harbor perspectives in biology* **10**, a033019 (2018).
135 Zu, T. *et al*. Non-ATG–initiated translation directed by microsatellite expansions. *Proceedings of the National Academy of Sciences* **108**, 260-265 (2011).
136 Zhang, H. *et al*. RNA controls PolyQ protein phase transitions. *Molecular cell* **60**, 220-230 (2015).
137 Jain, A. & Vale, R. D. RNA phase transitions in repeat expansion disorders. *Nature* **546**, 243-247 (2017).

138 Bettencourt, C. *et al*. DNA repair pathways underlie a common genetic mechanism modulating onset in polyglutamine diseases. *Annals of neurology* **79**, 983-990 (2016).

139 Haendel, M. *et al*. How many rare diseases are there? *Nature Reviews Drug Discovery* **19**, 77-78 (2020).

140 Bettencourt, C., Santos, C., Kay, T., Vasconcelos, J. & Lima, M. Analysis of segregation patterns in Machado–Joseph disease pedigrees. *Journal of human genetics* **53**, 920-923 (2008).

141 Orr, H. T. & Zoghbi, H. Y. Trinucleotide repeat disorders. *Annu. Rev. Neurosci.* **30**, 575-621 (2007).

142 Kawaguchi, Y. *et al*. CAG expansions in a novel gene for Machado-Joseph disease at chromosome 14q32. 1. *Nature genetics* **8**, 221-228 (1994).

143 Maciel, P. *et al*. Correlation between CAG repeat length and clinical features in Machado-Joseph disease. *American journal of human genetics* **57**, 54 (1995).

144 Figueiredo, F. *et al*. A Robust Assay to Monitor Ataxin-3 Amyloid Fibril Assembly. *Cells* **11**, 1969 (2022).

145 Bettencourt, C. *et al*. The APOE ε2 allele increases the risk of earlier age at onset in Machado-Joseph disease. *Archives of neurology* **68**, 1580-1583 (2011).

146 Jardim, L. B. *et al*. Neurologic findings in Machado-Joseph disease: relation with disease duration, subtypes, and (CAG) n. *Archives of neurology* **58**, 899-904 (2001).

147 Coutinho, P. & Andrade, C. Autosomal dominant system degeneration in Portuguese families of the Azores Islands: a new genetic disorder involving cerebellar, pyramidal, extrapyramidal and spinal cord motor functions. *Neurology* **28**, 703-703 (1978).

148 Paulson, H. Machado–Joseph disease/spinocerebellar ataxia type 3. *Handbook of clinical neurology* **103**, 437-449 (2012).

149 Riess, O., Rüb, U., Pastore, A., Bauer, P. & Schöls, L. SCA3: neurological features, pathogenesis and animal models. *The Cerebellum* **7**, 125-137 (2008).

150 do Carmo Costa, M. & Paulson, H. L. Toward understanding Machado–Joseph disease. *Progress in neurobiology* **97**, 239-257 (2012).

151 Harris, G. M., Dodelzon, K., Gong, L., Gonzalez-Alegre, P. & Paulson, H. L. Splice isoforms of the polyglutamine disease protein ataxin-3 exhibit similar enzymatic yet different aggregation properties. *PloS one* **5**, e13695 (2010).

152 Schmidt, T. *et al*. An isoform of ataxin-3 accumulates in the nucleus of neuronal cells in affected brain regions of SCA3 patients. *Brain pathology* **8**, 669-679 (1998).

153 Trottier, Y. *et al*. Heterogeneous intracellular localization and expression of ataxin-3. *Neurobiology of disease* **5**, 335-347 (1998).

154 Fang, S. & Weissman, A. A field guide to ubiquitylation. *Cellular and molecular life sciences: CMLS* **61**, 1546-1561 (2004).

155 Winborn, B. J. *et al*. The deubiquitinating enzyme ataxin-3, a polyglutamine disease protein, edits Lys63 linkages in mixed linkage ubiquitin chains. *Journal of Biological Chemistry* **283**, 26436-26443 (2008).

156 Burnett, B., Li, F. & Pittman, R. N. The polyglutamine neurodegenerative protein ataxin-3 binds polyubiquitylated proteins and has ubiquitin protease activity. *Human molecular genetics* **12**, 3195-3205 (2003).

157 Mao, Y. *et al*. Deubiquitinating function of ataxin-3: insights from the solution structure of the Josephin domain. *Proceedings of the National Academy of Sciences* **102**, 12700-12705 (2005).

158 Nicastro, G. *et al*. The solution structure of the Josephin domain of ataxin-3: structural determinants for molecular recognition. *Proceedings of the National Academy of Sciences* **102**, 10493-10498 (2005).

159 Nicastro, G. *et al*. Josephin domain of ataxin-3 contains two distinct ubiquitin-binding sites. *Biopolymers: Original Research on Biomolecules* **91**, 1203-1214 (2009).

160 McCampbell, A. *et al*. CREB-binding protein sequestration by expanded polyglutamine. *Human molecular genetics* **9**, 2197-2202 (2000).

161 Araujo, J. *et al*. FOXO4-dependent upregulation of superoxide dismutase-2 in response to oxidative stress is impaired in spinocerebellar ataxia type 3. *Human Molecular Genetics* **20**, 2928-2941 (2011).
162 Burnett, B. G. & Pittman, R. N. The polyglutamine neurodegenerative protein ataxin 3 regulates aggresome formation. *Proceedings of the National Academy of Sciences* **102**, 4330-4335 (2005).
163 Evert, B. O. *et al*. Ataxin-3 represses transcription via chromatin binding, interaction with histone deacetylase 3, and histone deacetylation. *Journal of Neuroscience* **26**, 11474-11486 (2006).
164 Li, F., Macfarlan, T., Pittman, R. N. & Chakravarti, D. Ataxin-3 is a histone-binding protein with two independent transcriptional corepressor activities. *Journal of Biological Chemistry* **277**, 45004-45012 (2002).
165 Wang, G.-h., Sawai, N., Kotliarova, S., Kanazawa, I. & Nukina, N. Ataxin-3, the MJD1 gene product, interacts with the two human homologs of yeast DNA repair protein RAD23, HHR23A and HHR23B. *Human molecular genetics* **9**, 1795-1803 (2000).
166 Shimohata, T. *et al*. Expanded polyglutamine stretches interact with TAFII130, interfering with CREB-dependent transcription. *Nature genetics* **26**, 29-36 (2000).
167 Landschulz, W. H., Johnson, P. F. & McKnight, S. L. The leucine zipper: a hypothetical structure common to a new class of DNA binding proteins. *Science* **240**, 1759-1764 (1988).
168 Jana, N. R. & Nukina, N. Misfolding promotes the ubiquitination of polyglutamine-expanded ataxin-3, the defective gene product in SCA3/MJD. *Neurotoxicity research* **6**, 523-533 (2004).
169 Gales, L. *et al*. Towards a structural understanding of the fibrillization pathway in Machado-Joseph's disease: trapping early oligomers of non-expanded ataxin-3. *Journal of molecular biology* **353**, 642-654 (2005).
170 Scarff, C. A. *et al*. A tale of a tail: Structural insights into the conformational properties of the polyglutamine protein ataxin-3. *International Journal of Mass Spectrometry* **345**, 63-70 (2013).
171 Masino, L. *et al*. The Josephin domain determines the morphological and mechanical properties of ataxin-3 fibrils. *Biophysical journal* **100**, 2033-2042 (2011).
172 Masino, L. *et al*. Characterization of the structure and the amyloidogenic properties of the Josephin domain of the polyglutamine-containing protein ataxin-3. *Journal of molecular biology* **344**, 1021-1035 (2004).
173 Ellisdon, A. M., Pearce, M. C. & Bottomley, S. P. Mechanisms of ataxin-3 misfolding and fibril formation: kinetic analysis of a disease-associated polyglutamine protein. *Journal of molecular biology* **368**, 595-605 (2007).
174 Woodruff, J. B., Hyman, A. A. & Boke, E. Organization and function of non-dynamic biomolecular condensates. *Trends in biochemical sciences* **43**, 81-94 (2018).
175 Alberti, S., Gladfelter, A. & Mittag, T. Considerations and challenges in studying liquid-liquid phase separation and biomolecular condensates. *Cell* **176**, 419-434 (2019).
176 Li, S. *et al*. Pressure and temperature phase diagram for liquid–liquid phase separation of the RNA-binding protein fused in sarcoma. *The Journal of Physical Chemistry B* **125**, 6821-6829 (2021).
177 Wang, Z., Zhang, G. & Zhang, H. Protocol for analyzing protein liquid–liquid phase separation. *Biophysics Reports* **5**, 1-9 (2019).
178 Van Lindt, J. *et al*. A generic approach to study the kinetics of liquid–liquid phase separation under near-native conditions. *Communications biology* **4**, 1-8 (2021).
179 Zai-Rose, V. *et al*. Effects of doxorubicin on the liquid-liquid phase change properties of elastin-like polypeptides. *Biophysical journal* **115**, 1431-1444 (2018).
180 Li, Y., Lubchenko, V. & Vekilov, P. G. The use of dynamic light scattering and Brownian microscopy to characterize protein aggregation. *Review of Scientific Instruments* **82**, 053106 (2011).
181 Poggemann, H.-F. (2021).
182 Mitrea, D. M. *et al*. Methods for physical characterization of phase-separated bodies and membrane-less organelles. *Journal of molecular biology* **430**, 4773-4805 (2018).

183 Erdős, G., Pajkos, M. & Dosztányi, Z. IUPred3: prediction of protein disorder enhanced with unambiguous experimental annotation and visualization of evolutionary conservation. *Nucleic acids research* **49**, W297-W303 (2021).
184 Lancaster, A. K., Nutter-Upham, A., Lindquist, S. & King, O. D. PLAAC: a web and command-line application to identify proteins with prion-like amino acid composition. *Bioinformatics* **30**, 2501-2502 (2014).
185 Hatos, A., Tosatto, S. C., Vendruscolo, M. & Fuxreiter, M. FuzDrop on AlphaFold: visualizing the sequence-dependent propensity of liquid–liquid phase separation and aggregation of proteins. *Nucleic Acids Research* (2022).
186 Conchillo-Solé, O. *et al*. AGGRESCAN: a server for the prediction and evaluation of" hot spots" of aggregation in polypeptides. *BMC bioinformatics* **8**, 1-17 (2007).
187 Tan, C., Saurabh, S., Bruchez, M. P., Schwartz, R. & LeDuc, P. Molecular crowding shapes gene expression in synthetic cellular nanosystems. *Nature nanotechnology* **8**, 602-608 (2013).
188 Nakano, S.-i., Miyoshi, D. & Sugimoto, N. Effects of molecular crowding on the structures, interactions, and functions of nucleic acids. *Chemical reviews* **114**, 2733-2758 (2014).
189 Paul, S. S., Sil, P., Chakraborty, R., Haldar, S. & Chattopadhyay, K. Molecular crowding affects the conformational fluctuations, peroxidase activity, and folding landscape of yeast cytochrome c. *Biochemistry* **55**, 2332-2343 (2016).
190 Takahashi, A., Nagao, C., Murakami, K., Kuroi, K. & Nakabayashi, T. Effects of molecular crowding environment on the acquisition of toxic properties of wild-type SOD1. *Biochimica et Biophysica Acta (BBA)-General Subjects* **1864**, 129401 (2020).
191 Shahid, S., Hassan, M. I., Islam, A. & Ahmad, F. Size-dependent studies of macromolecular crowding on the thermodynamic stability, structure and functional activity of proteins: in vitro and in silico approaches. *Biochimica et Biophysica Acta (BBA)-General Subjects* **1861**, 178-197 (2017).
192 Chiu, Y.-P. *et al*. Liquid-liquid phase separation and extracellular multivalent interactions in the tale of galectin-3. *Nature communications* **11**, 1-12 (2020).
193 Almeida, B., Fernandes, S., Abreu, I. A. & Macedo-Ribeiro, S. Trinucleotide repeats: a structural perspective. *Frontiers in neurology* **4**, 76 (2013).